Aeroacoustic Resonance of Slender Cavities

An experimental and numerical investigation

PROEFSCHRIFT

ter verkrijging van de graad van doctor
aan de Technische Universiteit Delft,
op gezag van de Rector Magnificus Prof. ir. K.Ch.A.M. Luyben,
voorzitter van het College voor Promoties,
in het openbaar te verdedigen op dinsdag 5 juni 2012 om 15:00 uur
door

Arjen Teake DE JONG

Doctorandus in de Natuur- en Sterrenkunde
Ingenieur in de Luchtvaart- en Ruimtevaarttechniek
Geboren te Amersfoort.

Dit proefschrift is goedgekeurd door de promotor:

Prof. dr. ir. drs. H. Bijl

Samenstelling promotiecommissie:

Rector Magnificus	voorzitter
Prof. dr. ir. drs. H. Bijl	Technische Universiteit Delft, promotor
Prof. dr. F. Scarano	Technische Universiteit Delft
Prof. dr. ing. G. Eitelberg	Technische Universiteit Delft
Prof. dr. ir. B.J. Boersma	Technische Universiteit Delft
Prof. dr. ir. A. Hirschberg	Technische Universiteit Eindhoven
Prof. dr. ing. J. Wiedemann	Universität Stuttgart
Dr. S. Cyr	Exa Corporation

ISBN 978-94-6203-047-3

Cover design by Sjouke de Jong and Richard de Jong
Printed by Wöhrmann Print Service

Author email: `arjendejongengineering@gmail.com`

Contents

Summary

Cavity aeroacoustic noise is relevant for aerospace and automotive industries and widely investigated since the 1950's. Most investigations so far consider cavities where opening length and width are of similar scale. The present investigation focuses on a less investigated setup, namely cavities that resemble the door gaps of automobiles. In automotive, the transmission of sound generated by cavity bodies into the interior and surroundings is an important topic. A door gap cavity can produce or amplify sound, and flexible seals can transmit this into the cabin. These cavities are both slender (width much greater than length or depth) and partially covered. Furthermore they are under influence of a low Mach number flow with a relatively thick boundary layer. Under certain conditions, these gaps can produce tonal noise. The present investigation is performed on simplified geometries in order to generalize the results for non-automotive applications where slender cavities are present as well. This thesis consists of three separate parts on the physics, flow control and simulation of slender cavities.

Part I: Understanding the physics of cavity resonance

First, the aeroacoustic mechanism of this tonal noise for higher resonance modes is investigated. Experiments have been conducted on a simplified geometry, where unsteady internal pressures have been measured at different spanwise locations. With increasing velocity, several resonance modes occur. In order to obtain higher mode shapes, the cavity acoustic response is simulated and compared with experiment. Using the frequency-filtered simulation pressure field, the higher modes shapes are retrieved. The mode shapes can be interpreted as the slender cavity self-organizing into separate Helmholtz resonators that interact with each other. Based on this an analytical model is derived that shows good agreement with the simulations and experimental results.

Compliance and real-world effects can influence the flow-driven aeroacoustic response of cavities. Particularly flexible seals can influence the compliance of the

cavity volume. A preliminary experimental campaign has been conducted using a cavity with back cabin in a blown splitter plate with various seal designs in between the two volumes. The influence of the investigated flexible seals on the cavity aeroacoustic response amplitude is minimal. The presence of flexible seals slightly lowers the resonance frequency, which can be expected due to the higher cavity compliance. Some differences in transmission properties between various seal designs have been measured in this preliminary investigation.

Part II: Passive and active control of cavity noise

Methods for both passive and active control of cavity noise have been evaluated. For passive resonance suppression, the design of the cavity opening is investigated. The upstream and downstream edge of the opening as well as the cover lip overhang location and boundary layer thickness are parametrically varied in an experimental campaign. The effect of the parameters on the resonance amplitude is investigated. Slender rectangular cavity geometries are used, with an opening length of 8 mm and spanwise width of 500 mm. The cavity flow induced acoustic response is measured with pressure transducers at different spanwise locations inside the cavity. Hot-wire measurements are performed to quantify the boundary layer characteristics. Furthermore, high speed time resolved Particle Image Velocimetry (PIV) is used to capture the instantaneous velocity field around the opening geometries. When the boundary layer thickness is increased, the cavity resonance amplitude diminishes. The cover lip overhang location has a large influence on the resonance response, which can be attributed to changes in the cavity driven flow properties. Rounding of the upstream edge promotes resonance, whereas rounding of the downstream edge can diminish it. A possible explanation of the phenomena is given on the basis of the PIV observations.

Next to passive tonal noise attenuation, an active flow control method has been tested. A novel dielectric barrier discharge plasma actuator configuration for flow control is employed on open cavities to evaluate the potential for aeroacoustic tonal noise reduction. Instead of a planar configuration, the actuator is designed around the cavity opening edges. The investigation focusses on the effectiveness for tonal noise suppression and the associated fluid dynamics. The investigated open cavities have a square cross-section. A low Mach flow with a thin laminar boundary layer introduces tonal sound emission due to hydrodynamic feedback. Both upstream and downstream edge actuators have been tested, and both cavity inwards and outwards actuation has been employed. The upstream mounted actuators influence cavity tonal feedback. A cavity inwards velocity inducing actuator completely suppresses the cavity tone up to a free-stream velocity of 12.5 m/s. An outwards inducing actuator influenced mode switching. Downstream mounted actuators did not influence the cavity aeroacoustics. PIV is used to investigate the fluid dynamics. The actuator can induce velocities up to 4 m/s for an applied voltage of 15 kV at 4 kHz. The induced velocity is directed perpendicular to the free stream direction. A secondary circulating flow is developed in the cavity that modifies the hydrodynamic feedback mechanism.

Part III: Simulation capabilities

The Lattice Boltzmann Method (LBM) is employed to evaluate simulation capabilities for resonating cavity aeroacoustics. Due to the inherent compressibility of the method, LBM is capable of simulating acoustic wave propagation as well as fluid flow. Sharp trailing edge noise is selected as a first test case for aeroacoustics without resonance but with the effect of turbulent boundary layers. LBM is used to simulate sharp trailing edge noise of NACA0012 and DU96-180 airfoils, for 0 and 7 degrees angle of attack. Both natural and tripped turbulence transition has been investigated. For tripped simulations, a zigzag type turbulator has been implemented. An additional high resolution simulation has been conducted as well for the tripped NACA0012 case at 0 degrees angle of attack. The far-field noise at two chords distance is calculated using an FW-H acoustic analogy and is compared to the simulated acoustics pressures directly obtained from the flow simulation domain. In order to compensate for the cyclic wall conditions in span, both a time based and frequency based analysis is conducted. The sound field from analogy and directly obtained sound field match well when the directly obtained pressures are modified to account for the cyclic conditions. Both sound fields have been normalized and compared to results in literature. The high resolution simulation matches the sound pressure level and frequency distribution well, the lower resolution simulations show an over-prediction.

After the trailing edge LBM simulations, simulation of the aeroacoustic resonance of partially covered slender cavities is performed. These cavities are under influence of a low Mach number flow with a relatively thick boundary layer. The requirements to simulate the resonance behavior using an LBM model are investigated. Special focus is put on the effect of simulation spanwise width and inflow conditions. In order to validate the simulations, experiments have been conducted on simplified geometries. The configuration consists of a partially covered, rectangular cavity geometry 32 x 50 x 250 mm in size, with opening dimensions of 8 x 250 mm. The cavity flow induced acoustic response is measured with microphones at different spanwise locations inside the cavity. Hot-wire measurements are performed in order to quantify the boundary layer characteristics. Furthermore, high speed time resolved PIV is used to capture the instantaneous velocity field around the opening geometry. Flow simulations show that the turbulent fluctuation content of the boundary layer is important to correctly simulate the flow induced resonance response. A minimum simulation spanwise width is needed to show good resemblance with experimental cavity pressure spectra. When a full spanwise width simulation is employed, base mode and higher modes are retrieved.

Samenvatting

Het aeroakoestische geluid van holtes/openingen/spouwen is een relevant onderwerp voor de lucht- en ruimtevaart en automobielindustrie en is op grote schaal onderzocht sinds de jaren '50. De meeste onderzoeken tot nu toe beschouwen holtes waarbij de verhouding van lengte en breedte van vergelijkbare omvang zijn. Het huidige onderzoek richt zich op een minder onderzochte geometrie, namelijk holtes die lijken op de deurspouwen van auto's. De afstraling en voortplanting naar het interieur en de omgeving van geluid gegenereerd door deurspouwen is een belangrijk onderwerp in de automobielindustrie. Een deurspouw kan geluid produceren of versterken, en via flexibele afdichtingen kan dit worden overgebracht naar de passagierscabine. Dit soort spouwen zijn zowel slank (met een veel grotere breedte dan lengte of diepte) als gedeeltelijk overdekt. Verder zijn deze onder invloed van een subsone stroming met laag Mach getal en een relatief dikke turbulente grenslaag. Onder bepaalde omstandigheden kunnen de openingen een toongeluid produceren. Het huidige onderzoek is uitgevoerd op vereenvoudigde geometrieën, zodat de resultaten ook bruikbaar zijn voor toepassingen met slanke holtes buiten de automobielsector. Dit proefschrift is ingedeeld in drie aparte delen die focussen op de physica, controle en simulatie van slanke holtes.

Deel I: Het begrijpen van de fysica van resonantie

Eerst is het aeroakoestische mechanisme van toongeluid voor hogere resonantiemodes onderzocht. Experimenten zijn uitgevoerd op een versimpelde geometrie, waar de fluctuerende interne drukken zijn gemeten op verschillende locaties in de spanwijdte. Er ontstaan verschillende resonantie modes met toenemende snelheid. De akoestische respons van de geometrie is gesimuleerd en vergeleken met akoestische experimenten om de spatiële vorm van de hogere modes in de holte te verkrijgen. Uit het per frequentieband gefilterde drukveld van de simulatie zijn de vormen van de hogere modes onttrokken. De hogere modes kunnen worden geïnterpreteerd als gekoppelde zelf-organiserende afzonderlijke Helmholtz resona-

toren die gerangschikt zijn in de spanwijdte. Op basis van dit is een analytisch model afgeleid dat goed overeenkomt met de akoestische simulaties en experimentele resultaten met stroming.

Flexibiliteit en geometrische effecten kunnen invloed hebben op de aeroakoestische respons van spouwen onder invloed van stroming. Vooral flexibele afdichtingen kunnen invloed uitoefenen op de akoestische impedantie van het volume van de holte. Er is een initiële experimentele campagne uitgevoerd op een gedeeltelijk overdekte holte tezamen met een onderliggende ruimte in een splitterplaat. Hierbij zijn verschillende flexibele afdichtingsontwerpen tussen de twee volumes in geplaatst. De invloed van de onderzochte flexibele afdichting op de aeroakoestische responsamplitude is minimaal. De aanwezigheid van flexibele afdichting vermindert licht de resonantiefrequentie, wat te verwachten is aan de hand van de toegenomen totale akoestische flexibiliteit. Er zijn verschillen gemeten in de transmissie-eigenschappen van de verschillende seal uitvoeringen in dit vooronderzoek.

Deel II: Passieve en actieve controle van toongeluid van openingen

Zowel methoden voor passieve als actieve resonantieonderdrukking zijn onderzocht. Voor passieve resonantieonderdrukking is het effect van het ontwerp van de openingen onderzocht. De stroomopwaartse en stroomafwaartse randen van de opening zijn hiervoor parametrisch gevarieerd in een experimentele campagne. Ook is aanhechtingslocatie van de overhangende lip veranderd die de opening gedeeltelijk afsluit en is de dikte van de grenslaag gevarieerd. Het effect van al deze parameters op de resonantie amplitude is onderzocht. Er is gebruik gemaakt van slanke rechthoekige geometrieen met een opening lengte van 8 mm en een breedte van 500 mm in de spanwijdte. De stromingsgeïnduceerde akoestische respons is gemeten met drukopnemers op verschillende locaties in spanwijdte. Om de grenslaag eigenschappen te kwantificeren zijn hittedraad metingen uitgevoerd. Daarnaast is PIV met hoge tijdsresolutie gebruikt om het instantane snelheidsveld vast te leggen rond de onderzochte openingsgeometrieën. Wanneer de grenslaagdikte toeneemt, vermindert de resonantie amplitude. De aanhechtingslocatie van de overhang heeft een grote invloed op de resonantie, wat kan worden toegeschreven aan veranderingen in stromingsbeeld binnenin de holte. Afronding van de stroomopwaartse rand bevordert resonantie, terwijl afronding van de stroomafwaartse rand resonantie kan verminderen. Een mogelijke verklaring voor dit verschijnsel wordt gegeven aan de hand van de waarnemingen met PIV.

Naast passieve geluid reductie door middel van het openingsontwerp, is een actieve stromingsbeheersingsmethode getest. Een nieuwe configuratie van plasma actuator op basis van diëlektrische barriereontlading is geëvaluteerd voor aeroakoestische resonantieonderdrukking. In plaats van een configuratie in een enkel vlak is de actuator ontworpen rondom de openingsranden. De effectiviteit voor tonale ruisonderdrukking en de bijbehorende stromingsleer is onderzocht. De onderzochte holten waren onafgedekt en met een vierkante dwarsdoorsnede. Een stroming met een dunne laminaire grenslaag introduceert een toongeluidsemissie als gevolg van hydrodynamische terugkoppeling. Zowel stroomopwaarts als stroomafwaarts gemonteerde actuatoren zijn getest, met zowel inwaarts als uitwaarts gerichte aansturing. De stroomopwaarts gemonteerde actuatoren beïnvloeden de terugkoppeling. Een inwaarts stromingsinducerende actuator onderdrukt volledig de caviteitstoon tot een vrije stroomsnelheid van 12,5 m/s. Een naar buiten inducerende actuator beïnvloed mode selectie. Stroomafwaarts gemonteerde actuatoren hadden geen invloed op de aeroakoestiek. PIV is gebruikt om de stromingdynamica in de spouw te onderzoeken. De actuatie kan snelheden induceren tot 4 m/s bij een spanning van 15 kV bij 4 kHz. De geïnduceerde snelheid staat loodrecht op de vrije stroom richting. Een tweede circulatiestroom wordt ontwikkeld in de holte die de hydrodynamische terugkoppeling wijzigt.

Deel III: Simulatiemogelijkheden

De Lattice Boltzmann Methode (LBM) is gebruikt voor evaluatie van de simulatie mogelijkheden van aeroakoestisch resonerende holtes. Door de inherente compressibiliteit van het LBM schema kan deze zowel akoestiek als vloeistofstroming tezamen simuleren. Als een eerste testcase is geluidsafstraling van een scherpe achterrand van een vleugelprofiel geselecteerd, omdat dit een testcase betreft zonder resonantie maar wel met het aeroakoestische effect van turbulente grenslagen. LBM is gebruikt om geluidsafstraling van de scherpe achterrand van NACA0012 en DU96-180 profielen te simuleren, voor 0 en 7 graden invalshoek. Zowel natuurlijke en geforceerde transitie naar turbulentie is onderzocht. Voor de simulaties met geforceerde transitie is een zigzagvormige turbulator geïmplementeerd. Ook is een hogere resolutie simulatie uitgevoerd voor het NACA0012 profiel bij 0 graden invalshoek. Er is een vergelijking gemaakt op twee koordlengten afstand van het profiel tussen het directe geluidsdrukveld uit het simulatiedomein en het indirect verkregen geluidsveld volgens een FW-H akoestische analogie. Er is zowel tijdsals frequentieanalyse uitgevoerd op het effect van cyclische randcondities. Wanneer gecompenseerd wordt voor de cyclische randvoorwaarden komen het direct verkregen geluidsveld en het geluidsveld volgens de analogie goed overeen. Beide geluidsvelden zijn genormaliseerd en vergeleken met de resultaten in de literatuur. Het spectrum van hogere resolutie simulatie komt goed overeen met literatuur voor zowel geluidsdrukniveau als frequentiedistributie. De lagere resolutie simulaties laten een te hoog geluidsniveau zien.

Na de hierboven beschreven LBM simulaties van vleugelprofielen zijn simulaties uitgevoerd van de aeroakoestische resonantie van slanke holtes die gedeeltelijk overdekt zijn. Deze holtes zijn onder invloed van een stroming met een laag Mach getal en met een relatief dikke grenslaag. De eisen voor het correct simuleren van het resonantie gedrag zijn onderzocht met behulp van LBM. Er is aandacht besteed aan het effect van spanwijdte van de simulatie en de instroomcondities. Ter validatie zijn stromingsexperimenten uitgevoerd. De onderzochte configuratie bestaat uit een gedeeltelijk afgesloten rechthoekige holte 32 x 50 x 250 mm groot, met een opening van 8 x 250 mm. De stromingsgeïnduceerde akoestische respons is gemeten met microfoons op verschillende locaties in de spanne binnen de holte. Hittedraad metingen zijn uitgevoerd om de grenslaag eigenschappen te kwantificeren. Bovendien is PIV met hoge tijdsresolutie gebruikt om het instantane snelheidsveld vast te leggen rond de opening. Uit de uitgevoerde stromingssimulaties blijkt, dat de turbulente fluctuaties van de grenslaag belangrijk zijn om de resonantieamplitude correct kunnen te simuleren. Een minimum simulatiebreedte in spanwijdte is nodig om een goede gelijkenis te tonen met experimentele spectra. Wanneer de volledige breedte is gesimuleerd, worden zowel de basis resonantiemode als de hogere moden met variatie in spanwijdte teruggevonden.

Chapter 1

Introduction

1.1 Aeroacoustics

Aeroacoustics is the study of the interaction between sound and fluid motion, it therefore is a fusion of the fields of acoustics and aerodynamics [1]. This thesis focusses on aeroacoustics of audible sound in air. Sound is often produced by motion of air. Examples are windblown musical instruments, where sound production is wanted [2]. Other examples include unwanted sound production, such as the noise from airplanes and cars [3].

Acoustics can be described as the study of small oscillatory motions and corresponding pressure waves in air which can be detected by the human ear: sound. In a sense, acoustics and fluid dynamics can be considered the same, as both describe the motion of air. However, for low Mach numbers, there are large differences in time scales, length scales and associated energies between acoustic emission and fluid motion. This makes the field of aeroacoustics challenging. To cover the range of pressure amplitudes in acoustics, a logarithmic scale for sound pressure level (SPL) is often employed. The SPL is defined as:

$$SPL = 20log_{10}\left(\frac{p_{rms}}{p_{ref}}\right), \tag{1.1}$$

where p_{rms} is the root mean square of pressure fluctuations and p_{ref} is the reference value of pressure in air, $p_{ref} = 2 \times 10^{-5} Pa$. In most cases, energy-wise the acoustic field is a small by-product of the hydrodynamic motions of fluids. In order to describe aeroacoustic production of sound, often an acoustic analogy is employed, where analogy refers here to the idea of representing a complex fluid mechanical process that acts as an acoustic source by an acoustically equivalent source term[1]. In 1952, Lighthill [4] rewrote the Navier-Stokes equations into an exact inhomogeneous wave equation, with nonzero right-hand-side. The Navier-Stokes equations for mass and momentum conservation are:

$$\frac{\partial \rho}{\partial t} + \frac{\partial}{\partial x_i}(\rho u_i) = 0 \tag{1.2}$$

$$\frac{\partial}{\partial t}(\rho u_i) + \frac{\partial}{\partial x_j}(\rho u_i u_j) = -\frac{\partial p}{\partial x_i} + \frac{\partial \tau_{ij}}{\partial x_j}, \tag{1.3}$$

where ρ, u, p are the fluid density, velocity and pressure. The viscous stress tensor τ_{ij} is defined as:

$$\tau_{ij} = \mu \left[\frac{\partial u_i}{\partial x_j} + \frac{\partial u_j}{\partial x_i} - \frac{2}{3} \left(\frac{\partial u_k}{\partial x_k} \right) \delta_{ij} \right], \tag{1.4}$$

where δ_{ij} is the Kronecker delta. Lighthill's formulation can be found by taking the time derivation of the mass conservation law and subtracting the divergence of the momentum equation, giving:

$$\frac{\partial^2 \rho'}{\partial t^2} - c_0^2 \frac{\partial^2 \rho'}{\partial x_i^2} = \frac{\partial^2 T_{ij}}{\partial x_i \partial x_j}, \tag{1.5}$$

with $T_{ij} = \rho u_i u_j + \left(p' - c_0^2 \rho'\right) \delta_{ij} - \tau_{ij}$ (the Renolds stress tensor) and $\rho' = \rho - \rho_0$, $p' = p - p_0$. ρ_0 and p_0 are the mean density and pressure respectively. Lighthill considered the right-hand-side of equation (1.5) a description for the sources of sound. Although the conversion into a wave equation was exact, the Lighthill acoustic analogy was not practical and only applicable in a limited number of cases. The interaction between solid walls and fluid flow was not taken into account for example and it is hard to obtain the Lighthill sources as it involves second derivatives of the Reynolds stress tensor. However, the landmark paper by Lighthill in effect started the modern field of aeroacoustics. Numerous acoustic analogies using approximations have been created since to provide a more practical estimate for sound prediction [5, 6, 7].

Acoustic emissions can be divided into three basic types: monopole, dipole and quadrupole [1]. Monopole sources arise due to fluctuating mass flow or volume changes and are typically the strongest sources of sound. The free field radiation of a monopole is uniformly omnidirectional. Dipole sources arise due to momentum fluctuations, where no net mass is added into the system. These can also be constructed (physically and mathematically) by two close monopoles in opposite phase. The free-field radiation has a directional axis of emission. Quadrupoles can be constructed by two opposite phase dipoles and is the weakest acoustic emitter. A speaker without enclosure can be considered a dipole source, as it transfers momentum. Within an enclosure, a typical speaker acts as a monopole, only the front of the membrane is exposed to the fluid within the vicinity of the speaker. Explosions can also be considered monopole sources. The turbulent eddies in a turbulent jet act as quadrupole sources [4]. The influence of solid boundaries can have a significant effect on sound emissions [5]. For example, in a boundary layer flow, the turbulent eddies effectively act as dipoles due to the presence of a wall [1].

1.2 Computational aeroacoustics

With increasing computer performance, the field of computational fluid dynamics (CFD) has risen in the 1990's and 2000's and CFD is now used extensively in industry and academics. More recently, the field of computational aeroacoustics (CAA) has undergone large developments [8, 9, 10, 11]. The differences in time, length and energy scales between fluid motion and acoustics have made it more difficult to predict aeroacoustics using computations.

Fluid dynamic turbulent motions can be an important source of sound in engineering applications. The effect of turbulence in CFD is traditionally often modeled with an effective viscosity in Reynolds Averaged Navier-Stokes (RANS) equations [12]. RANS simulations are typically steady in time, although there are applications of Unsteady RANS (URANS) where the large bulk fluid motion is simulated in time. Direct Numerical Simulation (DNS) resolves all scales of turbulent motion directly, but for general engineering problems at high Reynolds number, the computational time needed for a DNS simulation is far too high. The use of simulation of only large vortical structures using schemes such as Large Eddy Simulation (LES) [13] or Detached Eddy Simulation (DES) [14] has grown more popular for use in CFD with the increase in computing power. In these schemes typically a filter is employed in which the small scale turbulent structures are modeled and the large scale structures are resolved.

In CAA, steady RANS based modeling cannot be used for directly estimating the sound field as turbulent structures are not resolved. In order to use RANS solutions for the evaluation of sound emissions, reconstruction of the turbulent structures as acoustic sources is needed [15]. However, if the turbulent structures are simulated directly, no such reconstruction is needed. Schemes like LES and DES have therefore grown more popular in the CAA community. However, there are challenges concerning simulation dimensions, computational costs and numerical accuracy when using these schemes for CAA. In a large number of CAA applications, a split is made between the fluid dynamic field and the acoustic field, which are then one-way coupled [1]. For low Mach number flows, typically an incompressible fluid flow simulation is performed from which acoustic sources are extracted using an acoustic analogy[16, 17]. This one-way scheme with no influence from the acoustic field back to the fluid dynamics is not applicable for flows where the acoustic field influences the hydrodynamic solution, such as in the case of resonance. In case of resonance, direct noise computation (DNC) [18] is needed, employing a compressible type simulation that recovers acoustics as well as fluid dynamics. Vast differences in time, length and energy scales between fluid motion and acoustics make it difficult to implement DNC.

An interesting candidate for DNC computations is the Lattice Boltzmann Method (LBM). Most fluid dynamics simulation methods are based on discretization of the Navier-Stokes equations. LBM [19] is an alternative numerical method to traditional Navier-Stokes based CFD for simulating complex fluid flows. Unlike conventional methods based on macroscopic continuum equations, the LBM starts from mesoscopic kinetic equations, i.e. the Boltzmann equation, to determine macroscopic fluid dynamics. Due to its inherent compressible and time dependent nature, LBM inherently recovers acoustics [20]. Therefore the LBM method has been chosen in this thesis to evaluate DNC simulation capabilities for cavity aeroacoustics. Some fundamental aeroacoustic capabilities of the scheme have been studied before, such as wave propagation and compressible behavior [21]. In these cases the code has proven itself capable of correctly simulating acoustics related problems. Examples of the use of the Lattice Boltzmann scheme in (aero-)acoustics are simulation of radiation from waveguides, [22], acoustic pulses in flows and duct aeroacoustics [20], landing gear noise [23], wind noise [24], HVAC noise [25] and sunroof buffeting [26].

1.3 Cavity aeroacoustics

A typical configuration for producing sound is a cavity under a grazing flow. The flow over cavities is often studied for their intrinsic resonant behavior and the consequent significance of aeroacoustic noise production [27]. Depending on the cavity shape, feedback and/or resonance can occur [18]. This can create high amplitude tonal sound emissions.

Within the field of aeroacoustics a distinction can be made between aeroacoustics without hydrodynamic feedback, with feedback and with both feedback and acoustic resonance. Figure 1.1 gives examples of these aeroacoustic mechanisms. Examples of aeroacoustics without feedback include turbulent boundary layer [28, 29] and sharp trailing edge noise [30], where the turbulent pressure fluctuations are the source of sound. Cases with hydrodynamic feedback include blunt trailing edge noise [30] and shallow cavity noise [18]. Here the hydrodynamics of the configuration cause an oscillatory cycle in the flow, that in turn produces tonal sound emissions. In case of feedback, the shear layer can roll up into discrete vortices impinging on the opening trailing edge coherently (a Rossiter mode) [31], or the shear layer can exhibit a flapping shear layer motion. Rossiter's equation for the frequency is:

$$\frac{L}{U_c} + \frac{L}{c_0} = \frac{n+\alpha}{f}, \tag{1.6}$$

with U_c the vortex convection velocity, c_0 the speed of sound, n the mode number and $\alpha = 0.25$ a delay factor between vortex impingement and feedback. By varying the integer n corresponding to the number of perturbations present in the shear layer, several modes can be described. In the low Mach number limit, the feedback mode corresponds to excitation at a fixed Strouhal number $Sr = \frac{f\delta}{U_\infty} = c_n$, with f the frequency, δ the slot opening length and U_∞ the free stream velocity.

Examples of flows with acoustic resonance are deep and partially covered cavities [32, 33]. In this case there is a coupling between the fluid dynamics and acoustics of the fluid inside and around the cavity. The acoustic waves created within the fluid inside the cavity are acting on the hydrodynamic field. In case

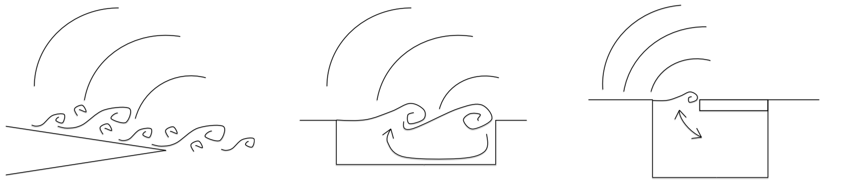

(a) no feedback (b) with hydrodynamic feedback (c) hydrodynamic feedback and acoustic resonance

Figure 1.1: overview of aeroacoustic divisions

of lock-on between the two fields, high amplitude tonal sound emissions can be produced. For deep cavities, the resonance is of a standing wave type, with crests and troughs. The frequencies for standing wave resonance in a rectangular box of dimensions L, D, W are [18, 27]:

$$f_{n_x,n_y,n_z} = \frac{c}{2}\sqrt{\left(\frac{n_x}{L}\right)^2 + \left(\frac{n_y}{D}\right)^2 + \left(\frac{n_z}{W}\right)^2}. \tag{1.7}$$

For partially covered cavities the resonance is of a Helmholtz resonance type, with typically nearly uniform compression of the fluid inside the cavity body. The equation for a Helmholtz resonator is [18]:

$$f_H = \frac{c}{2\pi}\sqrt{\frac{S}{VL'}}. \tag{1.8}$$

Here V is the cavity volume, S is the cavity neck surface area and L' is the corrected vertical length of the cavity neck. The relation between the real vertical cavity neck height L and L' is: $L' = L + l$, where l is an end correction factor to account for the added resonating mass above and below the opening. Cavity excitation for resonance can either be due to a feedback mechanism of the perturbed shear layer or due to passive excitation by the pressure fluctuations in the turbulent flow [34] (turbulent rumble). If the excitation frequency is close to a resonance frequency, lock-on can occur and the system can resonate. In case of turbulent rumble the resonance should effectively be independent of velocity.

The aeroacoustic behavior of cavities under a flow is complex and depends on a number of structural and fluid dynamic parameters, such as the cavity and opening dimensions, opening shape, upstream boundary layer profile and turbulence intensity. Howe's theory [35] indicated that an increased aspect ratio modifies the impedance, thereby reducing resonance. Kooijman et. al. [36] showed that by increasing the boundary layer momentum thickness compared to the opening length, the instability of the opening shear layer is reduced.

1.4 Technological applications of cavity aeroacoustics

Cavity noise is common in numerous applications such as transport systems (trains, planes, cars) [23, 24, 25, 26, 37] and industrial internal flow (side branches in pipe systems) [2]. Cavity systems can also be used to attenuate sound, such as is used in liners and mufflers [1]. Cavity aeroacoustic noise is thus relevant for aerospace and automotive industries and widely investigated since the 1950's. In automotive there are a large number of cavity structures that can be defined. These include the car cabin when the windows are (partially) opened, mirror gaps and door and trunk lid gaps [26, 37]. An example from non-automotive ground transportation is the noise from the pantograph recess in trains [38].

In the aircraft industry, most focus has been put on open shallow cavities [31]. These cavities resemble aircraft weapon bays and landing gear wheel wells [39]. Deep cavity resonance has also been a topic of interest, for example in side branches of pipe systems [40, 41]. Covered cavity geometries have been investigated in detail, where the cavity often behaves like a Helmholtz resonator. For example Dequand et. al. [42, 43] investigated the resonance lock-on amplitude of several rectangular Helmholtz resonator geometries under a thin boundary layer flow. Examples of applications are the sound generation in flute like instruments [44, 45, 46], the buffeting of open car sunroofs and side windows [47, 48] and Helmholtz resonators used in acoustic liners [49].

Most investigations in literature, so far, consider cavities where the opening length and width are of similar scale. The present investigation focuses on a less investigated setup, namely cavities that resemble the door gaps of automobiles. Often these cavity structures are slender, with a width that is much larger than typical streamwise dimensions or depth, and partially covered. Furthermore they are under influence of a low Mach number flow with a relatively thick boundary layer. Under certain conditions, these gaps can produce tonal noise [3, 33, 50, 51]. Only limited investigations have been performed on these specific configurations and it is difficult to reliably predict tonal amplitudes [37, 52, 53].

1.5 Aim of this thesis

The current thesis focusses on the aeroacoustical response of low Mach number flow over slender cavities. The intended applications include, but are not limited to, door and trunk lid gaps. In order to be generally applicable for other applications outside automotive, the research is performed on simplified open and partially covered cavities. The aims of this thesis regarding the investigated geometries are:

- to understand the physics of tonal flow-induced resonance,
- to evaluate techniques to control resonance behavior,

- to investigate if the flow-induced behavior can be predicted using CFD/CAA simulations.

In this thesis both wind tunnel experiments and CFD/CAA simulations are used, next to analytical models of cavity resonance. For the control of the flow induced behavior, both passive and active flow control techniques are investigated experimentally. For simulations, LBM is used due to its aeroacoustic capabilities.

1.6 Thesis outline

The thesis is divided into three parts, which each cover a topic of research corresponding to the aims described in section 1.5.

First, in part one, certain cavity geometries and setups are investigated with the aim to gain physical understanding of the main aeroacoustic mechanisms that come into play. Special focus is put on understanding the physics of observed higher resonance modes with resonance amplitude variation in the spanwise direction. In chapter 2 the effects of spanwise modes in slender cavity geometries are investigated. The studied simplified cavities of this chapter are fully rigid, whereas in real-world applications, often a compliant structure such as a synthetic rubber seal is present. The influence of flexible seals on the cavity flow induced behavior based on conducted experiments is discussed in chapter 3. The results of chapters 2 and 3 together with prior knowledge on cavity flow resonance provide a base for further investigations on the control and simulation of cavity.

In part two, a number of experimental investigations are presented and discussed to evaluate the potential for passive (by structural design) and active (using active flow control) methods to suppress or minimize the tonal emissions of slender cavities. In chapter 4 a parametric investigation on the influence of the cavity design and incoming turbulent boundary layer is presented. The onset of cavity resonance is sensitive to the detailed design of the resonator opening. The large difference in resonance behavior between an upstream and downstream overhang lip is investigated in more detail using high speed particle image velocimetry (PIV) and shear layer stability analysis. Besides passive control methods by means of geometric design, active control of cavity resonance has been investigated as well. In chapter 5 the potential of controlling tonal emissions by use of a novel layout dielectric barrier discharge plasma actuator is shown. Dielectric barrier discharge plasma actuators are relatively simple and involve no moving parts. Typically these actuators are constructed in a single plane, however in the current investigation the actuator is designed around open cavity corners. It turns out that upstream mounted actuators can prevent cavity resonance. PIV is used to study the fluid mechanics of the achieved resonance suppression.

Finally, in part three, an investigation is conducted on the ability to use computational fluid dynamics and computational aeroacoustics in predicting cavity aeroacoustic behavior. In this study, a Lattice Boltzmann Method is employed due to its inherent aeroacoustic behavior. As the simulation of cavity aeroacoustics encompass multiple facets such as fluid dynamics simulation of the turbulent boundary layer and acoustic propagation and aeroacoustic resonance. A preliminary test case is selected where the acoustic behavior in absence of feedback and resonance is investigated, in combination with evaluation of the hydrodynamic capabilities of the Lattice Boltzmann method. The selected test case is airfoil sharp trailing edge noise, where a turbulent attached boundary layer streaming over the sharp trailing edge is creating broadband sound emissions. In chapter 6 the ability of the implemented code to correctly simulate turbulent boundary layer airfoil trailing edge noise is studied as a test case for LBM aeroacoustic capabilities. The hydrodynamic behavior of the airfoil and the acoustic emissions are studied separately. The directly obtained acoustic spectra are compared to ones obtained using an acoustic analogy. Also a comparison with experimental acoustic results is made. The setup of the trailing edge noise test case is used as a base for cavity aeroacoustic simulations. In chapter 7 LBM is implemented on a cavity geometry where aeroacoustic resonance comes into play. The effect of boundary layer turbulence and simulation spanwise width is investigated. A comparison with own experiments is made where the simulations are shown to be able to retrieve the aeroacoustic resonance spectra for the base mode as well as for the higher modes with spanwise variations.

Bibliography

[1] Hirschberg, A. and Rienstra, S., "An introduction to aeroacoustics," `www.win.tue.nl/~sjoerdr/papers/les-swr-mh.pdf` (date last viewed 04/25/12), Eindhoven University of Technology, July 2004.

[2] Dequand, S., *Duct aeroacoustics: from technological applications to the flute*, Ph.D. thesis, Eindhoven University of Technology, 2000.

[3] Henderson, B. S., "Category 6 Automobile Noise Involving Feedback - Sound Generated by Low Speed Cavity Tones," NASA Techical Report, 2000, 95-100.

[4] Lighthill, M., "On sound generated aerodynamically. I. General theory," *Proceedings of the Royal Society of London. Series A, Mathematical and Physical Sciences*, Vol. 211, No. 1107, 1952, pp. 564–587.

[5] Curle, N., "The influence of solid boundaries upon aerodynamic sound," *Proceedings of the Royal Society of London. Series A, Mathematical and Physical Sciences*, Vol. 231, No. 1187, 1955, pp. 505–514.

[6] Powell, A., "Theory of vortex sound," *Journal of the Acoustical Society of America*, Vol. 36, 1964, pp. 177–195.

[7] Ffowcs-Williams, J. and Hall, L., "Aerodynamic sound generation by turbulent flow in the vicinity of a scattering half plane," *Journal of Fluid Mechanics*, Vol. 40, No. 04, 1970, pp. 657–670.

[8] Kurbatskii, K. and Mankbadi, R., "Review of computational aeroacoustics algorithms," *International Journal of Computational Fluid Dynamics*, Vol. 18, No. 6, 2004, pp. 533–546.

[9] Brouwer, H. and Rienstra, S., "Aeroacoustics research in Europe: The CEAS-ASC report on 2007 highlights," *Journal of Sound and Vibration*, Vol. 318, No. 4-5, 2008, pp. 625–654.

[10] Juvé, D., "Aeroacoustics research in Europe: The CEAS-ASC report on 2008 highlights," *Journal of Sound and Vibration*, Vol. 328, No. 1-2, Nov 2009, pp. 213–242.

[11] Casalino, D., "Aeroacoustics research in Europe The CEAS-ASC report on 2009 highlights," *Journal of Sound and Vibration*, Vol. 329, No. 22, Oct 2010, pp. 4810–4828.

[12] Blazek, J., *Computational Fluid Dynamics: Principles and Applications*, Elsevier, 2001.

[13] Wagner, C., Huettl, T., and Sagaut, P., *Large-Eddy Simulations for Acoustics*, Cambridge University Press, 2007.

[14] Spalart, P. R., "Detached-Eddy Simulation," *Annual Review of Fluid Mechanics*, Vol. 41, No. 1, January 2009, pp. 181–202.

[15] Doolan, C., "A review of airfoil trailing edge noise and its prediction," *Acoustics Australia*, Vol. 36, No. 1, Jan 2008, pp. 7–13.

[16] Gloerfelt, X., Bailly, C., and Juvé, D., "Direct computation of the noise radiated by a subsonic cavity and application of integral methods," *Journal of Sound and Vibration*, Vol. 226, No. 1, 2003, pp. 119–146.

[17] Lai, H. and Luo, K. H., "A three-dimensional hybrid les-acoustic analogy method for predicting open-cavity noise," *Flow, Turbulence and Combustion*, Vol. 79, No. 1, 2007, pp. 55–82.

[18] Gloerfelt, X., "Cavity noise," `http://sin-web.paris.ensam.fr/squelettes/ref_biblio/Gloerfelt_VKI_2009a.pdf` (date last viewed 04/25/12), 2009.

[19] Succi, S., *The lattice Boltzmann equation for fluid dynamics and beyond*, Oxford University Press, 2001, pp. 11-13.

[20] Li, X. M., Leung, R. C., and So, R. M. C., "One-Step Aeroacoustics Simulation Using Lattice Boltzmann Method," *AIAA Journal*, Vol. 44, No. 1, January 2006, pp. 78–89.

[21] Crouse, B., Freed, D. M., Balasubramanian, G., Senthooran, S., Lew, P., and Mongeau, L., "Fundamental Aeroacoustic Capabilities of the Lattice-Boltzmann Method," *12th AIAA/CEAS Aeroacoustics Conference*, No. AIAA-2006-2571, Cambridge, Massachussets, May 2006, pp. 2571–2588.

[22] da Silva, A. A. and Scavone, G. P., “Lattice Boltzmann simulations of the acoustic radiation from waveguides,” *Journal of Physics A*, Vol. 40, 2007, pp. 397–408.

[23] Brès, G., Wessels, M., and Noelting, S., “Tandem Cylinder Noise Predictions Using Lattice Boltzmann and Ffowcs Williams-Hawkings Methods,” *16th AIAA/CEAS Aeroacoustics Conference*, No. AIAA-2010-3791, Stockholm, Sweden, June 2010.

[24] Pérot, F., Meskine, M., and Vergne, S., “Investigation of the statistical properties of pressure loadings on real automotive side glasses,” *15th AIAA/CEAS Aeroacoustics Conference*, No. AIAA-2009-3402, Miami, Florida, May 2009.

[25] Lee, D. K., Pérot, F., and Freed, D. M., “The prediction of the flow induced noise related to automotive HVAC systems,” *SAE Technical Paper*, 2011-01-0493, 2011, doi:10.4271/2011-01-0493.

[26] Crouse, B., Balasubramanian, G., Senthooran, S., and Freed, D. M., “Investigation of gap deflector efficiency for reduction of sunroof buffeting,” *SAE Technical Paper*, 2009-01-2233, 2009, doi:10.4271/2009-01-2233.

[27] Rockwell, D. and Naudascher, E., “Self-sustained oscillations of impinging free shear layers,” *Annual Review of Fluid Mechanics*, Vol. 11, 1979, pp. 67–94.

[28] Meecham, W. C., “Surface and volume sound from boundary layers,” *Journal of the Acoustical Society of America*, Vol. 37, 1965, pp. 516–522.

[29] Ronneberger, D. and Ahrens, C., “Wall shear stress caused by small amplitude perturbations of turbulent boundary-layer flow: an experimental investigation,” *Journal of Fluid Mechanics*, Vol. 83, 1977, pp. 433–464.

[30] Brooks, T., Pope, T., and Marcolini, M., “Airfoil self noise and prediction,” Tech. Rep. 1218, NASA reference publication, 1989.

[31] Rossiter, J. E., *Wind-tunnel experiments on the flow over rectangular cavities at subsonic and transonic speeds*, London, H.M.S.O., 1st ed., 1967, pp. 1-32.

[32] Forrestier, N., Jacquin, L., and Geffroy, P., “The mixing layer over a deep cavity at high-subsonic speed,” *Journal of Fluid Mechanics*, Vol. 475, 2003, pp. 101–145.

[33] Nelson, P. A., Halliwell, N. A., and Doak, P. E., “Fluid Dynamics of a Flow Excited Resonance, Part I: Experiment,” *Journal of Sound and Vibration*, Vol. 78, No. 1, 1981, pp. 15–38.

[34] Elder, S. A., Farabee, T. M., and DeMetz, F. C., “Mechanisms of Flow-excited Cavity Tones at Low Mach Number,” *Journal of the Acoustical Society of America*, Vol. 72, No. 2, 1982, pp. 532–549.

[35] Howe, M. S., “Low Strouhal number instabilities of flow over apertures and wall cavities,” *Journal of the Acoustical Society of America*, Vol. 102, No. 2, 1997, pp. 772–780.

[36] Kooijman, G., Hirschberg, A., and Golliard, J., “Acoustical response of orifices under grazing flow: Effect of boundary layer profile and edge geometry,” *Journal of Sound and Vibration*, Vol. 315, 2008, pp. 849–874.

[37] Milbank, J., *Investigation of fluid-dynamic cavity oscillations and the effects of flow angle in an automotive context using an open-jet wind tunnel*, Ph.D. thesis, RMIT university, August 2004.

[38] Noger, C., Patrat, J. C., Peube, J., and Peube, J. L., “Aeroacoustical study of the TGV pantograph recess,” *Journal of Sound and Vibration*, Vol. 231, 2000, pp. 563–575.

[39] Lawson, S. J. and Barakos, G. N., “Review of numerical simulations for high-speed, turbulent cavity flows,” *Progress in Aerospace Sciences*, Feb 2011, pp. 1–31.

[40] Radavich, P. M., Selamet, A., and Novak, J. M., “A computational approach for flow-acoustic coupling in closed side branches,” *Journal of the Acoustical Society of America*, Vol. 109, No. 4, 2001, pp. 1343–1353.

[41] Dequand, S., Hulshoff, S. J., and Hirschberg, A., “Self-sustained oscillations in a closed side branch system,” *Journal of Sound and Vibration*, Vol. 265, 2003, pp. 359–386.

[42] Dequand, S., Luo, X., Willems, J., and Hirschberg, A., “Helmholtz-Like Resonator Self-Sustained Oscillations, Part 1: Acoustical Measurements and Analytical Models,” *AIAA journal*, Vol. 41, No. 3, March 2003, pp. 408–415.

[43] Dequand, S., Hulshoff, S., Kuijk van, H., Willems, J., and Hirschberg, A., “Helmholtz-Like Resonator Self-Sustained Oscillations, Part 2: Detailed Flow Measurements and Numerical Simulations,” *AIAA journal*, Vol. 41, No. 3, March 2003, pp. 416–424.

[44] Dequand, S., Willems, J. F. H., Leroux, M., Vullings, R., van Weert, M., Thieulot, C., and Hirschberg, A., “Simplified models of flue instruments: Influence of mouth geometry on the sound source,” *Journal of the Acoustical Society of America*, Vol. 113, No. 3, March 2003, pp. 1724–1735.

[45] Coltman, J. W., “Jet Drive Mechanism in Edge Tones and Organ Pipes,” *Journal of the Acoustical Society of America*, Vol. 60, No. 3, 1976, pp. 725–733.

[46] Elder, S. A., “On the Mechanism of Sound Production in Organ Pipes,” *Journal of the Acoustical Society of America*, Vol. 54, 1973, pp. 1554–1564.

[47] Crouse, B., Senthooran, S., Balasubramanian, G., Freed, D., Noelting, S., Mongeau, L., and Hong, J. S., "Sunroof Buffeting of a Simplified Car Model: Simulations of the Acoustic and Flow-Induced Responses," *SAE Technical Paper*, 2005-01-2498, 2005, doi:10.4271/2005-01-2498.

[48] Ricot, D., Maillard, V., and Bailly, C., "Numerical Simulation of the Unsteady Flow past a Cavity and Application to Sunroof Buffeting," *7th AIAA/CEAS Aeroacoustics Conference*, Maastricht, The Netherlands, May 2001, pp. 1–11, AIAA-2001-2112.

[49] Ingard, U., "On the theory and design of acoustic resonators," *Journal of the Acoustical Society of America*, Vol. 25, No. 6, November 1953, pp. 1037–1061.

[50] Henderson, B. S., "Category 5: Sound Generation in Viscous Problems, Problem 2: Sound Generation by Flow over a Cavity," NASA Technical Report, 2004, 71-77.

[51] Nelson, P. A., Halliwell, N. A., and Doak, P. E., "Fluid Dynamics of a Flow Excited Resonance, Part II: Flow Acoustic Interaction," *Journal of Sound and Vibration*, Vol. 91, No. 3, 1983, pp. 375–402.

[52] Mongeau, L., Bezemek, J. D., and Danforth, R., "Pressure Fluctuations in a Flow-Excited Door Gap Model," *SAE Technical Paper*, 971923, 1997, doi:10.4271/971923.

[53] Ma, R., Slaboch, P., and Morris, S., "Fluid mechanics of the flow-excited Helmholtz resonator," *Journal of Fluid Mechanics*, Vol. 623, Jan 2009, pp. 1–26.

Part I

Understanding the physics of cavity resonance

Chapter 2

Higher spanwise Helmholtz resonance modes in slender covered cavities

This chapter is based on the published journal paper:

Higher spanwise Helmholtz resonance modes in slender covered cavities
A.T de Jong and H. Bijl
Journal of the Acoustical Society of America
***128** (4), pp 1668-1678, October 2010*

(Submitted 26 October 2009, revised 8 July 2010, accepted 9 July 2010)

Cavity aeroacoustic noise is relevant for aerospace and automotive industries and widely investigated since the 1950's. Most investigations so far consider cavities where opening length and width are of similar scale. The present investigation focuses on a less investigated setup, namely cavities that resemble the door gaps of automobiles. These cavities are both slender (width much greater than length or depth) and partially covered. Furthermore they are under influence of a low Mach number flow with a relatively thick boundary layer. Under certain conditions, these gaps can produce tonal noise.

The present investigation attempts to reveal the aeroacoustic mechanism of this tonal noise for higher resonance modes. Experiments have been conducted on a simplified geometry, where unsteady internal pressures have been measured at different spanwise locations. With increasing velocity, several resonance modes occur. In order to obtain higher mode shapes, the cavity acoustic response is simulated and compared with experiment. Using the frequency-filtered simulation pressure field, the higher modes shapes are retrieved. The mode shapes can be interpreted as the slender cavity self-organizing into separate Helmholtz resonators that interact with each other. Based on this an analytical model is derived that shows good agreement with the simulations and experimental results.

2.1 Introduction

Cavity geometries under influence of a grazing flow can produce aeroacoustic noise. The mechanism for this noise is dependent on the cavity geometry and flow properties. In literature, most focus has been on certain geometry types (various non-slender cavities) due to their relevance in aerospace and automotive industries.

In the aircraft industry, most focus has been put on open shallow cavities. These cavities resemble aircraft weapon bays and landing gear wheel wells [1]. An example outside the aircraft industry is the noise from the pantograph recess in trains [2]. Deep cavity resonance has also been a topic of interest, for example in side branches of pipe systems [3, 4]. Covered cavity geometries have been investigated in detail, where the cavity often behaves like a Helmholtz resonator. For example Dequand et. al. [5, 6] investigated the resonance lock-on amplitude of several rectangular Helmholtz resonator geometries under a thin boundary layer flow. Examples of applications are the sound generation in flute like instruments [7, 8, 9], the buffeting of open car sunroofs and side windows [10, 11] and Helmholtz resonators used in acoustic liners [12].

The current investigation concerns a special setup relevant in the automobile industry, the tonal noise from automobile gaps. These covered cavities are slender (width much larger than length or depth) and under influence of a low Mach number flow ($M \approx 0.1$) with a relatively thick boundary layer. Both slenderness and a thick boundary layer reduce the resonance response of a cavity. Howe's theory [13] indicated that an increased aspect ratio modifies the impedance, thereby reducing resonance. Kooijman et. al. [14] showed that by increasing the boundary layer momentum thickness compared to the opening length, the instability of the opening shear layer is reduced. In fact, in general door gaps only show a passive response to the flow, although there are cases where a resonance lock-on can occur.

Door gap structures have not been examined in great detail, although quite some investigations on geometries of this kind can be found in literature. For example Nelson [15, 16] experimentally analyzed a Helmholtz resonator with laser Doppler velocimetry, where an opening slot of 600 by 10 mm was excited by a grazing flow of 16 to 27 m/s. In addition, Henderson [17, 18] presented benchmark experimental data of a resonator with a 460 by 8 mm slot with a thick boundary layer flow of 45 to 60 m/s. Mongeau et. al. [19] show experimental results of a 25 cm wide cavity that resembles a door gap, including a seal fixture, where the cavity showed a passive response to the outside flow.

The current investigation is set up to investigate the acoustic resonance behavior over a wide range of velocities in order to reveal a multitude of acoustic resonance modes, with special focus on resonances with spanwise variations that occur. Spanwise modes have been identified in shallow cavities in a large eddy simulation of a weapon bay by Larchevêque [20], corresponding to simple spanwise room modes. For covered cavities, Henderson mentioned the possible existence of modes with spanwise variation. But the pressure excitations were measured at a single spanwise location and it was therefore not possible to identify these modes. Mongeau observed passive low amplitude spanwise modes which were not coupled to higher amplitude excitations. Therefore they do not correspond to spanwise varying resonance modes observed in the current research.

In the present investigation experiments, simulations and analytical studies are combined. First experiments have been conducted on a simplified cavity geometry, where unsteady internal pressures have been measured at different spanwise locations. In order to obtain the experimentally observed higher mode shapes, the cavity acoustic response is simulated and compared with experiment. Using the frequency-filtered simulation pressure field, the higher modes are identified and an analytical model is derived. Sections 2.3 and 2.4 give the experimental flow run setup and results. The numerical acoustic response test is described in section 2.5. The analytical model is derived and compared with the flow run experimental results in section 2.6.

2.2 Theory: Cavity resonance modes

This section briefly explains the aeroacoustic mechanisms possible in the investigated setup. A cavity volume can act as an acoustic resonator to an excitation source in the cavity neck region.

The excitation can either be due to a feedback mechanism of the perturbed shear layer or due to passive excitation by the pressure fluctuations in the turbulent flow [21] (turbulent rumble). In case of feedback, the shear layer can roll up into discrete vortices impinging on the opening trailing edge coherently (a Rossiter mode) [1], or exhibit a flapping shear layer motion. In the low Mach number limit, a feedback mode corresponds to excitation at a fixed Strouhal number $Sr = \frac{f\delta}{U_\infty}$, with f the frequency, δ the slot opening length and U_∞ the free stream velocity. If the excitation frequency is close to a resonance frequency, lock-on can occur and the system can resonate. In case of turbulent rumble the resonance should effectively be independent of velocity.

The resonance method can either be of a Helmholtz type or of a standing wave type. In Helmholtz-like resonance the mass of air in the cavity is coherently compressed and expanded. The equation for a Helmholtz resonator is [22]:

$$f_H = \frac{c}{2\pi}\sqrt{\frac{S}{VL'}}. \tag{2.1}$$

Here V is the cavity volume, S is the cavity neck surface area and L' is the corrected vertical length of the cavity neck. The relation between the real vertical cavity neck height L and L' is $L' = L + l$, where l is an end correction factor to account for the added resonating mass above and below the opening. For non-slender openings it is based on the surface area $l \propto \sqrt{S}$, whereas in the slotted opening of the current investigation, it is assumed to be related to the opening length only $l \propto \delta$ and independent of the slot width W [12].

Besides Helmholtz-like excitation, where the air in the cavity is coherently pressurized and expanded, standing wave patterns inside the cavity can emerge. The combined effect of all acoustic pressure waves in the cavity volume can create a standing pattern consisting of a fixed number of sinusoidal waves between opposite cavity boundaries. The frequencies for a rectangular box of dimensions L_{cav}, D, W are [22]:

$$f_{n_x,n_y,n_z} = \frac{c}{2}\sqrt{\left(\frac{n_x}{L_{cav}}\right)^2 + \left(\frac{n_y}{2D}\right)^2 + \left(\frac{n_z}{W}\right)^2}. \tag{2.2}$$

2.3 Experimental setup

The experimental geometry consists of a rectangular cavity partially closed off by a rigid overhang from the leading edge of the cavity. The cavity opening is subjected to a flow with a thick (compared to the opening length δ) flat plate boundary layer profile. The aspect ratio of the cavity is large, $\frac{W}{\delta} >> 1$.

For the experiments the vertical tunnel (V-tunnel), located at Delft University of Technology in the Netherlands was used. The V-tunnel is a tunnel with an open test section and a vertical outflow through a circular opening, 0.6 m in diameter. Due to the high contraction ratio of the settling chamber the quality of the airflow is high (low turbulence) and the tunnel is relatively silent.

The model used in the windtunnel is a cavity embedded in a splitter plate which has an elliptic nose cone. Figure 2.1 gives the dimensions of the cavity and figure 2.2 shows a photograph of the splitter plate with the embedded cavity. The expected Helmholtz resonance frequency is around 800 Hz and expected base resonance onset velocity is 25 m/s. This is in the velocity range of the used vertical windtunnel (0 to 47 m/s) and is also an interesting velocity to resemble a car door gap (typical car highway speeds).

The boundary layer develops on the first section of the plate. By adjusting the length of the splitter plate and the location of trip wires the boundary layer is controlled in a precise and reproducible way. In the setup used for this publication, the splitter plate upstream flat plate section is set to 0.7 m and a 1 mm high zigzag type turbulator strip is located 10 cm from the splitter plate nose.

The cavity itself is constructed out of thick-walled aluminum to ensure enough rigidity to prevent fluid-structure resonance effects. Interchangeable parts are used to alter the neck geometry. The cavity neck is equipped with sharp edges and a leading edge overhang, as depicted in figure 2.1.

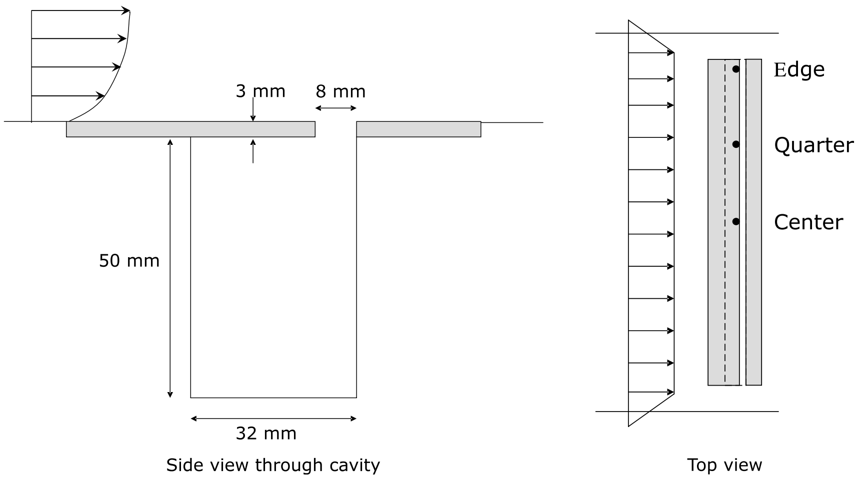

Figure 2.1: Cavity dimensions.

The maximum spanwise width of the cavity is set to 0.5 m, which is smaller than the 0.6 m width of the splitter plate itself. This leaves 5 cm on both sides (shown in figures 2.1 and 2.2) to ensure that the end effects of the outlet (the shear layer of the outlet jet) will not reach the cavity region. In this way the flow speed and boundary layer shape remain constant along the whole span of the cavity. The current experiments also include runs with a reduced cavity width of 0.3 m by closing one side with blocks in both the interior and opening. This reduced setup is used to evaluate the effect of the total span on the resonance behavior.

First the cavity has been closed off to determine the boundary layer characteristics. These are measured with a constant temperature hotwire probe. The velocity magnitude in the boundary layer is measured at 25 different heights (with uneven spacing, most measurements in the lower regions), for 4 different flow speeds (20, 24 , 30 and 40 m/s) and 3 spanwise locations (center, quarter and edge of cavity, see figure 2.1).

Flow runs with open cavity have been performed to measure the flow induced sound pressure levels inside the cavity. The velocity is increased incrementally, up to the wind tunnel limit of approximately 47 m/s. The open cavity flow run experiments use 3 pressure transducers. These are located at different spanwise locations (center, quarter, and edge) on the floor of the cavity, as indicated in figure 2.1.

2.4 Experimental results

In this section the obtained experimental results of the boundary layer properties and cavity internal pressure fluctuations are presented. The cavity measurement data are split into the full span (0.5 m) and reduced span (0.3 m) results.

Figure 2.2: The windtunnel model.

2.4.1 Boundary layer profiles

The boundary layer measurement results are used to check the boundary layer height, shape and fluctuations. This will allow reproducibility of setup conditions for future experiments and simulations. Also, the measurements are used to check that the flow properties are constant across the entire span.

The profiles for the mean and root mean squared (RMS) fluctuation profiles of velocity magnitude (more accurately the vector addition of the streamwise and vertical velocity component) are given in figure 2.3 for the center location (middle of the cavity neck opening, 25 cm from the opening edge). The other two locations, quarter (12.5 cm from the opening edge) and edge have similar boundary layer properties. The figures show that the boundary layer properties remain similar during the flow sweep. There is a mild thickness decrease with increasing velocity due to Reynolds effects [23].

The following integral properties are displayed in table 2.1: the displacement thickness δ^*, the momentum thickness θ, the shape factor H and the height at 99% of the mean flow δ_{99} [23]. The displacement thickness δ^*, momentum thickness θ, and shape factor H are defined as:

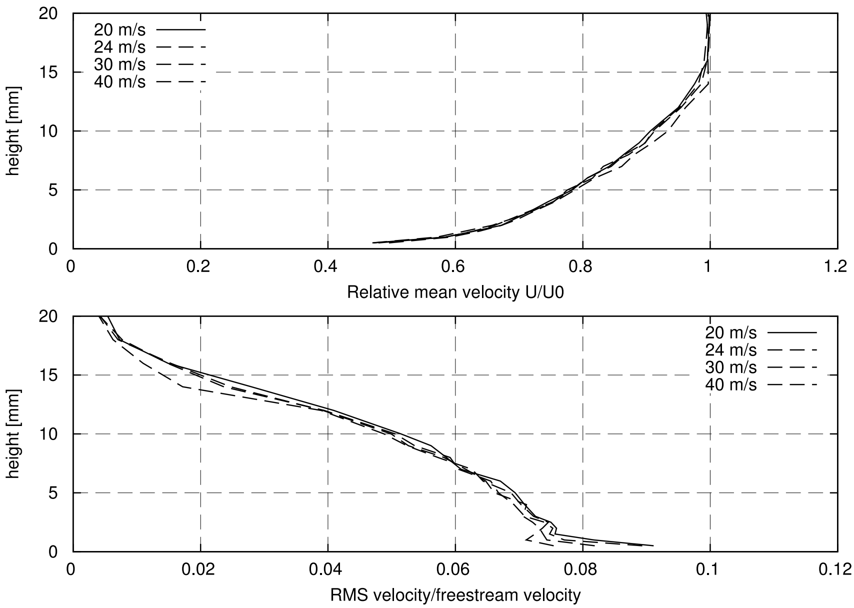

Figure 2.3: Experimental boundary layer mean (top) and rms (bottom) profiles of velocity magnitude.

$$\delta^* = \int_0^\infty \left(1 - \frac{\bar{u}}{U_e}\right) dy, \tag{2.3}$$

$$\theta = \int_0^\infty \frac{\bar{u}}{U_e}\left(1 - \frac{\bar{u}}{U_e}\right) dy, \tag{2.4}$$

$$H = \frac{\delta^*}{\theta}, \tag{2.5}$$

where U_e is the velocity outside the boundary layer and $\bar{u}$ the local mean velocity magnitude at height y. The table includes boundary layer data for 3 different spanwise locations to indicate the consistency across the span.

2.4.2 Full cavity span flow runs, 0.5 m width

Now that the boundary layer properties are known, the cavity flow induced resonance can be investigated. The cavity resonance is measured for 2 span widths, 0.5 m and 0.3 m. This section presents the full 0.5 m span results and the next section the 0.3 m reduced span ones.

The flow velocity is increased incrementally. The internal probe sound pressure levels of these velocity sweeps are gathered in spectrograms and given in figure 2.4 for all 3 probe locations. The frequency of the excitation is shown at the vertical

Table 2.1: Overview of boundary layer properties, center/quarter/edge location in span as indicated in figure 2.1.

flow velocity $[m/s]$	location	δ^*	θ	H	$\delta_{99}[mm]$
20	center	2.46	1.80	1.36	15.4
24	center	2.40	1.75	1.37	14.9
24	quarter	2.50	1.80	1.39	15.2
24	edge	2.43	1.78	1.37	14.9
30	center	2.46	1.79	1.38	15.9
40	center	2.24	1.64	1.37	13.6

axis and the free stream velocity on the horizontal one. The amplitude of the excitation in dB is indicated by level. The figure shows several resonating modes with increasing velocity and increasing frequency. The first resonance is visible at all probe locations whereas for the higher modes some are not. This indicates a spanwise variation in the higher resonance modes.

From figure 2.4 it is found that all the center points of the excitation modes show a linear relation between frequency and velocity. The Strouhal number $Sr = \frac{fL}{U_\infty}$ corresponding to this is approximately 0.3, indicating that all modes are excited by the first stage hydrodynamic mode [1]. No excitations of the second stage hydrodynamic mode ($Sr \approx 0.7$) are present, although low amplitude onsets of resonance for this Strouhal number can be observed in the upper left part of the figures as light horizontal lines.

Figure 2.5 shows the pressure time series of the three cavity probes at four different resonance modes. Some resonances do not show excitations of some of the probes, indicating the presence of pressure nodes at that location. Also for the higher modes the excitations of the probes can be of opposite phase.

In figure 2.5 it can be seen that in the base resonance all probes are in phase with each other and have similar excitation amplitudes. This observation enables us to identify the base mode as a Helmholtz resonance. Using Eq. (2.1) and the experimental excitation frequency of around 800, the resonator added length is found to be $l = 2.4\delta$.

Even though the acoustic pressure amplitudes can be around 120 dB, it can be calculated that the energy transfer from flow to acoustics is low [5]. In figure 2.5 the maximum acoustic pressure amplitude is $|p| = 30$ Pa and $|p| = 100$ Pa for the 22 and 42 m/s case respectively. The estimated acoustic velocity amplitude $|u_{ac}|$ in the neck region for a lumped mass system can be estimated by:

$$\frac{|u_{ac}|}{U_0} \approx \frac{1}{U_0}\frac{V}{\rho_0 S}\left|\frac{d\rho}{dt}\right| = \frac{1}{U_0}\frac{V}{\rho_0 S c^2}\left|\frac{dp}{dt}\right| = \frac{1}{U_0}\frac{L_{cav}}{\delta}\frac{2\pi f D}{c}\frac{|p|}{\rho_0 c}, \qquad (2.6)$$

with $S = \delta W$ the area of the neck opening and $V = L_{cav}DW$ the cavity volume. Here we used $dp = c^2 d\rho$ with c the speed of sound.

Substituting $f = 800$ Hz, $U_0 = 22$ m/s, $|p| = 30$ Pa will give $\frac{|u_{ac}|}{U_0} \approx 1 \cdot 10^{-2}$ and substituting $f = 1600$ Hz, $U_0 = 42$ m/s, $|p| = 100$ Pa will give $\frac{|u_{ac}|}{U_0} \approx 3 \cdot 10^{-2}$.

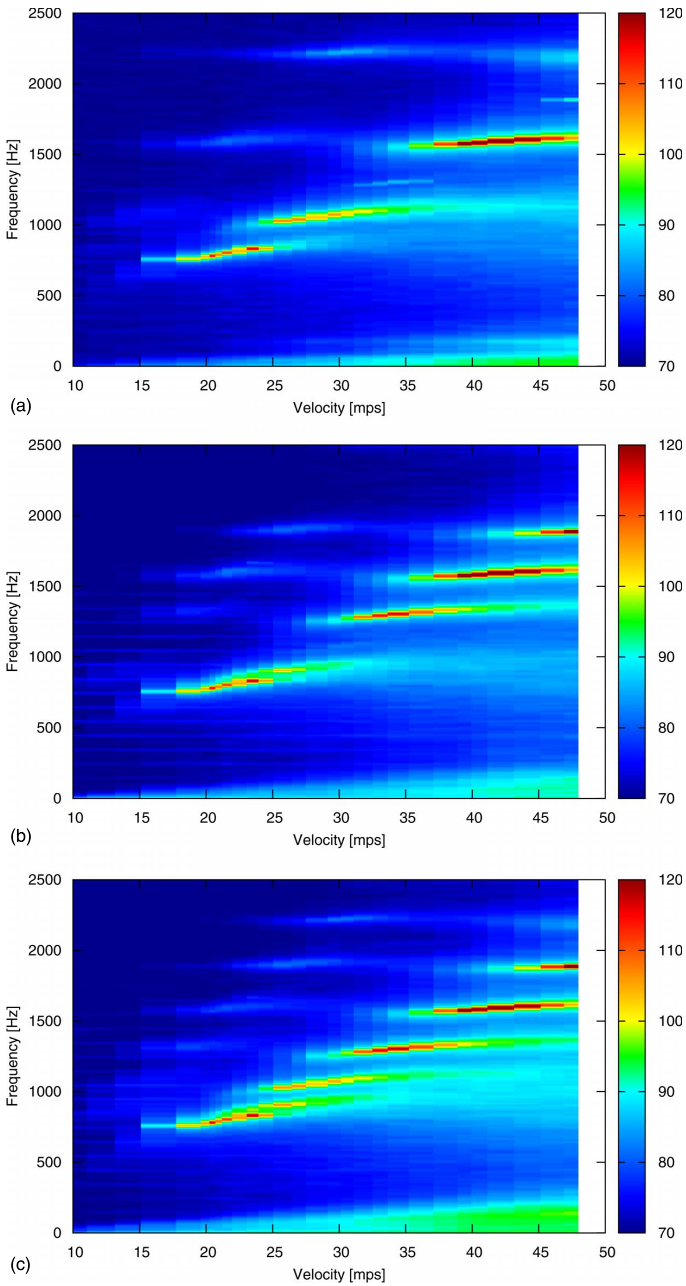

Figure 2.4: Spectrograms of the three internal pressure transducers, full 0.5 m span runs, level by sound pressure $[dB]$. From top to bottom: center, quarter, edge location.

Table 2.2: Comparison flow run mode frequencies with pure standing wave modes.

Mode	Exp. freq. [Hz]	Shape matching st. wave number $n_{st} = 2W/\lambda$	St. wave freq. [Hz]
1	830	n/a	n/a
2	900	1	340
3	1050	2	680
4	1300	3	1020
5	1600	4	1360
6	1900	5	1700

The low acoustical amplitude makes the lock-on hard to predict [24].

The higher modes are not simple pure standing waves according to Eq. (2.2), because standing waves that match the observed spanwise pressure variations do not match the observed frequencies. This is indicated in table 2.2, where frequencies of standing wave modes that match the phases and node locations indicated in figures 2.4 and 2.5 are compared to the experimentally observed frequencies. λ is the standing mode wavelength. Note that in this table the coherently excited base mode does not match any standing wave mode shape. The exact mechanism for the higher modes is not known yet based on the current experimental information. This is why in the next section the effect of a smaller span is investigated to reveal the influence of the total spanwise width.

2.4.3 Effect of a smaller span on the flow induced response

In order to investigate the higher modes with spanwise variation in more detail, flow runs with a reduced span of 0.3 m are conducted. All other dimensions remained the same compared to the 0.5 m span experiments. The spectrograms of the flow induced response for the edge probe is given in figure 2.6. The modes are all excited by the first stage Rossiter mode. The most noticeable differences compared to the 0.5 m span runs of the lower graph of figure 2.4 are the lower base mode resonance amplitude and location of the higher modes in the diagram.

The base mode has a frequency of around 800 Hz, which is the same as for the 0.5 m span cavity. This confirms that the slender Helmholtz added length l of Eq. (2.1) is independent of the cavity width W. By comparing the higher modes in the lower graph of figure 2.4 with figure 2.6, a distinct influence of the spanwise width can be observed. The higher modes are shifted to larger velocities and have higher frequencies. For example the second mode shifted from 26 m/s, 900 Hz to 28 m/s, 1000 Hz and the third mode shifted from 28 m/s, 1100 Hz to 34 m/s, 1400 Hz. The shifts cause less modes to appear in the used velocity interval of 10 m/s to 47 m/s. The smaller span runs reveal strong dependence of the higher mode excitation frequency on the spanwise length. The next section describes an experimental and numerical acoustic response test that will be used to obtain the exact mode shape of the observed modes.

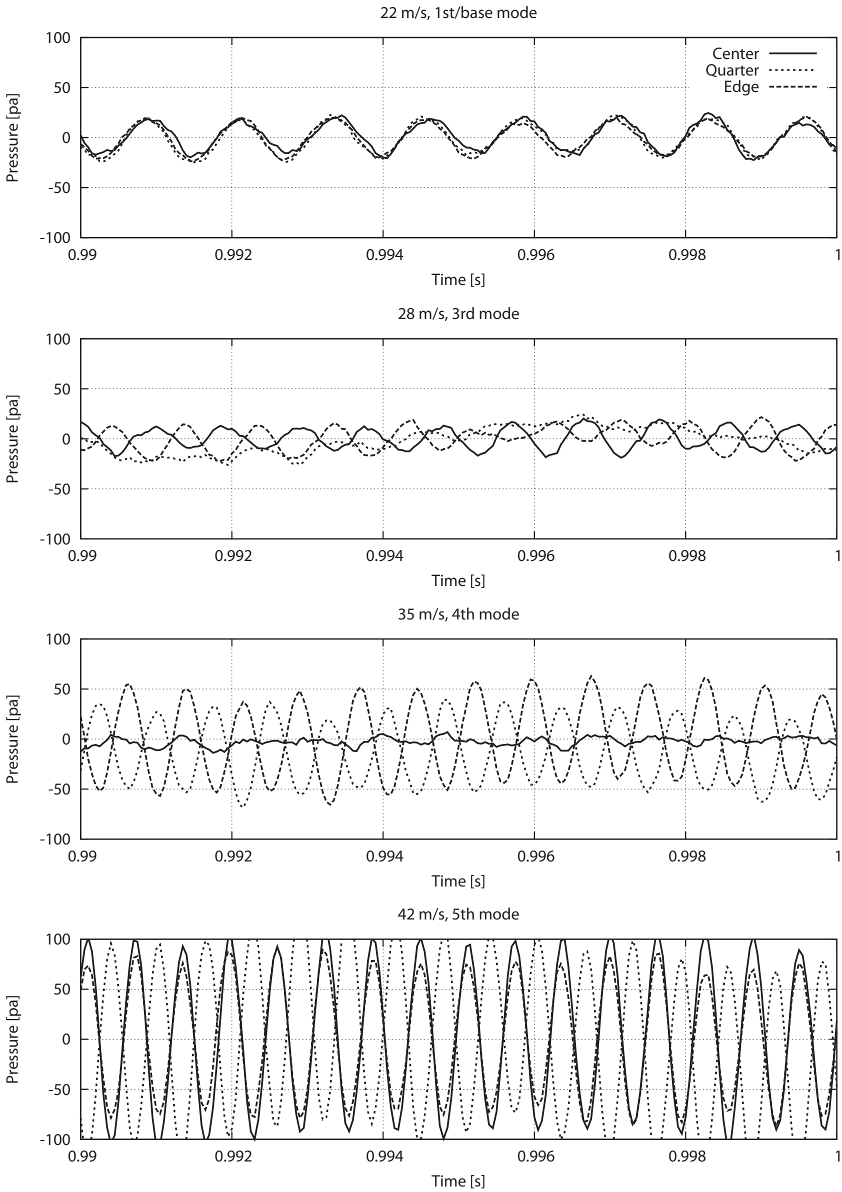

Figure 2.5: Pressure time series of the 3 cavity internal probes for some of the observed modes.

2.5 Acoustic response test

This section describes the numerical and the experimental acoustic response test (ART). An acoustic response test provides the acoustic reaction of the cavity setup

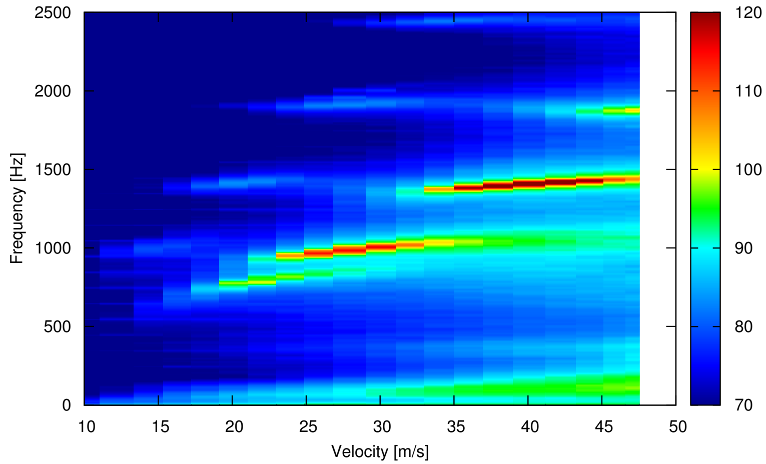

Figure 2.6: Spectogram of flow run with a 0.3 m span, edge location internal cavity probe, level by sound pressure $[dB]$.

in the absence of flow. The numerical simulation is used to obtain the exact mode shapes of the cavity resonances. The experimental ART is used to validate the numerical results.

2.5.1 ART setup

In an ART external speakers emitting a white noise signal are used to excite the cavity in the absence of flow. Microphones inside and outside gather the sound pressure level data.

The excitation of the cavity can be quantified using the complex transfer function. This is the complex ratio of the sound pressure spectrum inside the cavity to a reference outside the cavity. The resulting complex function in frequency is divided by the complex transfer function of a closed cavity where both the main and reference probe are outside. This last extra step provides a frequency dependent scaling to compensate for transfer losses of sound from the speaker toward the cavity region.

Two important properties of Helmholtz resonators are the resonance frequency f_H and the quality factor, Q. The resonance frequency is the frequency at which the strongest resonance might occur. The Q-factor describes the sharpness of the resonance peak (as a function of frequency) and can be related to the acoustic impedance of the resonator. The quality factor is defined as:

$$Q = \frac{f_H}{f_2 - f_1}, \tag{2.7}$$

with f_1 and f_2 frequencies at half the amplitude of the resonance frequency, where $f_1 < f_H$ and $f_2 > f_H$.

The experimental and numerical complex transfer ratios are compared with an analytical model for a resonator in order to obtain the resonance frequency f_H and quality factor Q. The analytical model is fitted with the results using a L2 vector fit in both phase and magnitude. The analytical expression for the transfer magnitude $\|H(f)\|$ is [10]:

$$\|H(f)\| = \frac{1}{k\sqrt{\left(1 - (f/f_H)^2\right)^2 + 4D^2\,(f/f_H)^2}} \tag{2.8}$$

with k the system stiffness and D the damping. The quality factor is related to the damping by $Q = \frac{1}{2D}$.

2.5.2 Numerical scheme; The Lattice Boltzmann Method

The numerical ART is obtained using the Lattice Boltzmann Method (LBM) [25]. LBM is an alternative numerical method to traditional CFD for simulating complex fluid flows. Unlike conventional methods based on macroscopic continuum equations, the LBM starts from mesoscopic kinetic equations, i.e. the Boltzmann equation, to determine macroscopic fluid dynamics. The commercial LBM based package PowerFLOW is used.

The Lattice Boltzmann equation has the following form:

$$f_i\left(\vec{x} + \vec{c_i}\Delta t, t + \Delta t\right) - f_i\left(\vec{x}, t\right) = C_i\left(\vec{x}, t\right), \tag{2.9}$$

where f_i is the particle distribution function moving in the ith direction, according to a finite set of the discrete velocity vectors $\{\vec{c_i} : i = 0, ..., N\}$. $\vec{c_i}\Delta t$ and Δt are space and time increments respectively. In the low frequency and long-wavelength limit, for a suitable choice of the set of discrete velocity vectors, one can recover the compressible Navier-Stokes equations through the Chapman-Enskog expansion for Mach numbers less than (approximately) 0.4 [25]. By recovering the compressible Navier-Stokes equations, including an ideal gas equation of state, LBM also inherently recovers acoustics. Some fundamental aeroacoustic capabilities of the scheme have been studied before, such as wave propagation and compressible behavior [26, 27]. In these cases the code has proven itself capable of correctly simulating these acoustics related problems. Examples of the use of the Lattice Boltzmann scheme in acoustics are simulation of radiation from waveguides, [28], acoustic pulses in flows and duct aeroacoustics [29], and side branches [27].

It should be noted that in the current paper the LBM method is only used for an acoustic response without mean flow, whereas full non-linear flow simulations

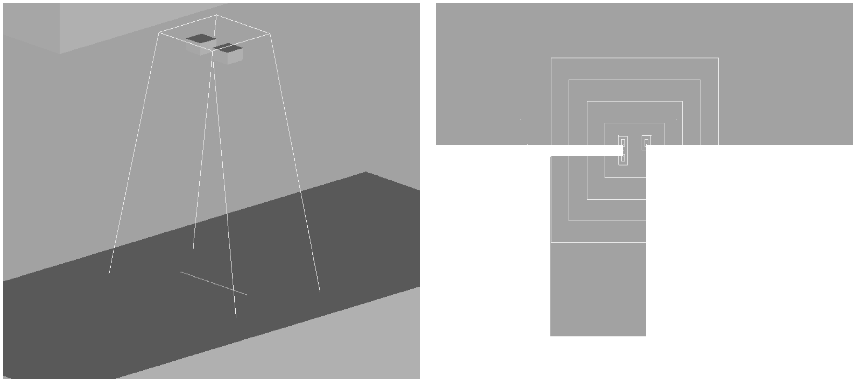

Figure 2.7: Acoustic response test simulation setup. The resolution region boundaries are indicated by white contours. Across these boundaries the linear resolution is increased by a factor of two, with the finest region having 8 cells/mm. Two speakers, each with their own white noise signal are suspended 2 m above the cavity. Left figure gives 3d view of domain with speakers in top of figure and cavity slot below, right figure shows a vertical slice through cavity.

are possible. Other options to simulate the ART are also possible, such as the boundary element method or finite element method. The authors are planning to perform flow simulations as well in a separate investigation in the future, and therefore LBM is chosen as method of preference.

2.5.3 Numerical setup

Both the simulated and experimental ART has the same setup and two-step approach of section 2.5.1. The full cavity 3d model is included in the simulation and there is no flow present. Two speakers, each with their own independent white noise signal, are used in the numerical setup. Both are positioned at a distance of 2 meters from the cavity (same as in experiment) and are relatively close to each other (30 cm between speaker centers). Both the experimental and numerical setup included 2 speakers to ensure excitation of the modes with spanwise variation.

The LBM is solved on a grid composed of cubic volumetric elements, and variable resolution is allowed, where the grid size changes by a factor of two for adjacent resolution regions. Figure 2.7 gives the resolution regions around the neck of the cavity and speakers. The finest region is located at the sharp edges of the cavity neck and is 8 cells/mm in resolution. This resolution setting has been chosen based on mesh convergence tests on a similar geometry performed by the authors. In addition, the experimental ART is used to validate the simulation setup. In both the experimental and numerical ART the cavity probes are located in the center on the cavity floor.

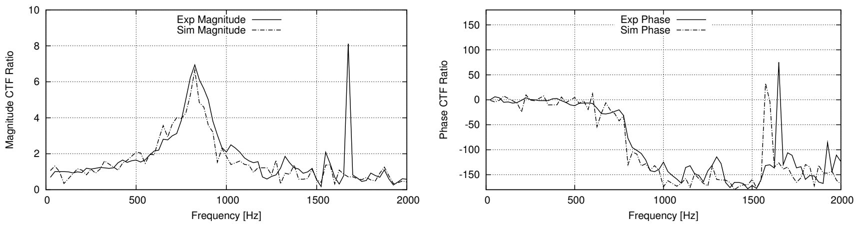

Figure 2.8: Acoustic response test experiment and simulation results of the complex transfer function ratio magnitude (left) and phase (right).

Table 2.3: Experimental and simulation resonance frequency and quality factor.

	f_H [Hz]	Q-factor
Simulation, sharp edges	803	5.0
Experiment, sharp edges	828	5.9

2.5.4 Comparison ART experiment and simulation

This section presents the ART results in order to validate the numerical simulation using the experimental ART. Figure 2.8 shows the phases and magnitudes of the experimental and numerical ART. For both the experimental and numerical ART, the microphones are positioned at the quarter location in span, as indicated in figure 2.1. Table 2.3 shows the resonance frequency and quality factor of the complex transfer ratio fits described in section 2.5.1. Due to the probe quarter location in the cavity some higher modes cannot be captured in this figure. The sound pressure level of the remaining higher mode around 1600 Hz is significantly lower and therefore not clearly distinguishable. Both in experiment and simulation there is a second dominant mode at around 3800 Hz that is not indicated in the figure because it is out of the range of interest.

According to table 2.3, the base resonance frequency is within 5 % of the experimental results. The acoustic non-compactness of the aperture causes high radiation losses, which accounts for the low observed Quality factors compared to compact aperture resonators [24]. The similarity between the experimental and numerical base resonance frequency and quality factor validate the use of an acoustic response test simulation to obtain the acoustic properties of slender cavities.

2.5.5 ART simulation band-filtered mappings

The previous section showed that the LBM simulations can predict the acoustic response of the investigated simplified slender cavities. The acoustic simulation results are now used to investigate the observed behavior in experimental flow runs by band-filtering the pressure signal of the ART simulation. In this way maps of acoustic pressure intensity are obtained to check for the acoustic cavity behavior around the higher resonant modes.

Figure 2.9 shows the result of band-filtering the cavity pressure spectra around the most prominent modes observed in the experimental flow runs. This is displayed in a vertical plane through the resonator center. The used bandwidth is 25 Hz. The pressure maps correspond well to the pressure nodes and phase of the flow experiment probes in figure 2.5. The shape of the modes can be viewed as the cavity subdividing itself into regions acting as separate Helmholtz resonators that interact with each other. The locations corresponding to the end masses of the Helmholtz resonators are then indicated in the figures by the low sound pressure regions and the locations of the Helmholtz resonator volumes themselves are indicated by the high sound pressure regions. In the next section an analytical model of the resonance frequency based on coupled Helmholtz resonators is derived based on these observations.

As mentioned in section 2.5.4, the ART complex transfer ratio shows a secondary dominant excitation at around 3800 Hz, an excitation which is not observed in the flow experiments. The band-filtered pressure map of Figure 2.10 shows the mechanism for this secondary peak. Instead of a Helmholtz mode, this is a vertical cavity standing wave mode.

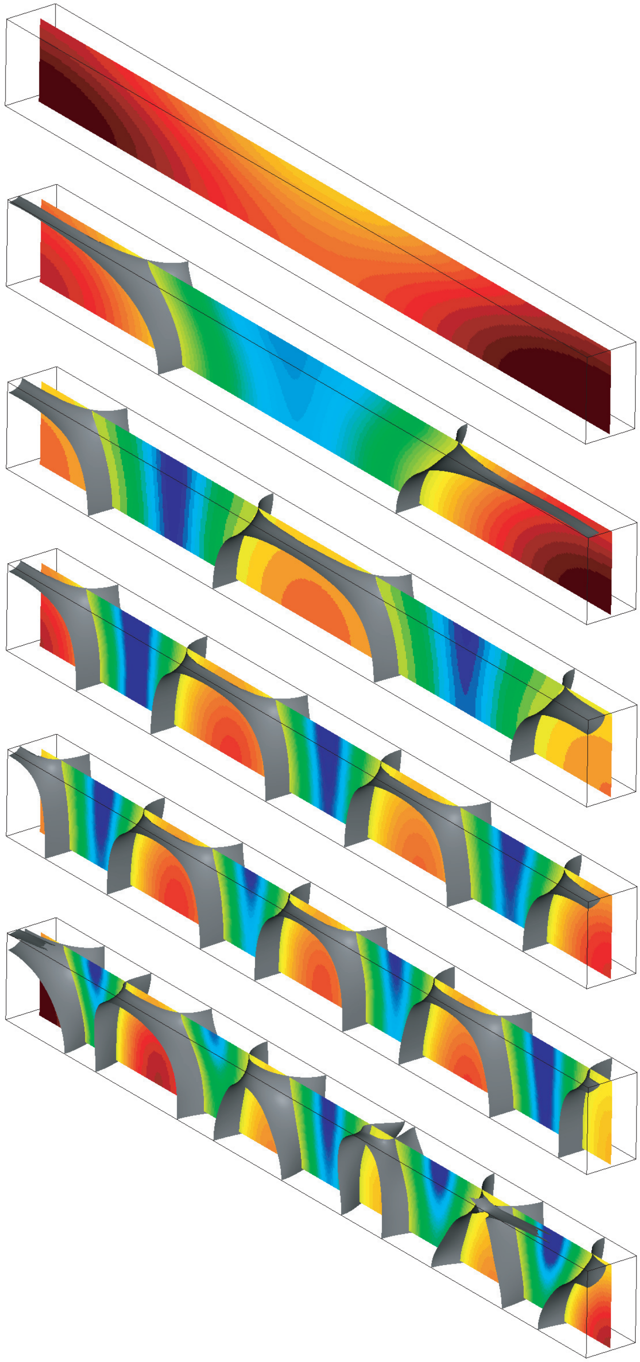

Figure 2.9: ART simulation band-filtered pressure signals in the cavity on a vertical plane through the cavity neck opening in dB for 825, 925, 1050, 1325, 1575 and 1925 Hz respectively. Level bandwidth is 20 dB, frequency bandwidth 25 Hz. 3d isosurfaces of constant sound pressure level are included. The cavity opening slot is located on top towards the viewer.

2.6 Analytical model of multiple Helmholtz resonators

A lumped mass analytical model of the higher resonance modes is derived using the hypothesis that spanwise sections act as separate coupled Helmholtz resonators. In this section the resonance frequency of a system of n spanwise resonators is determined and compared with the experimentally observed acoustic modes and simulation ART results.

2.6.1 Model derivation

The derivation of the lumped mass analytical model for the multiple Helmholtz resonator mode frequency is related to the derivation of the normal Helmholtz resonator frequency model. It is based on mass conservation in the resonator bodies and momentum conservation in the cavity openings and inter-resonator sections. The equations of a coupled system are explained in this section by using a setup of two spanwise resonators, see figure 2.11. In this figure m, S indicate the masses and surface areas of the moving air columns, V the volumes of the resonator sections and W the widths of the inter-resonator and resonator sections. It is assumed that inter-resonator coupling occurs only within the cavity; acoustic coupling outside the cavity is neglected. Coherent compression is assumed within each resonator body.

The integral mass conservation law applied to one resonator volume can be

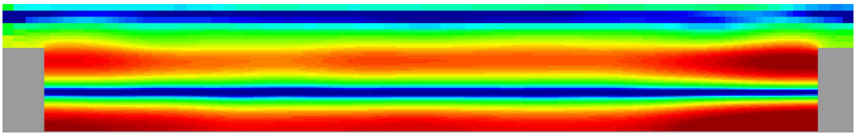

Figure 2.10: ART simulation band-filtered pressure signals in the cavity on a vertical plane through the cavity neck opening in dB for the 3800 Hz excitation standing wave mode. Level bandwidth is 20 dB, frequency bandwidth 100 Hz.

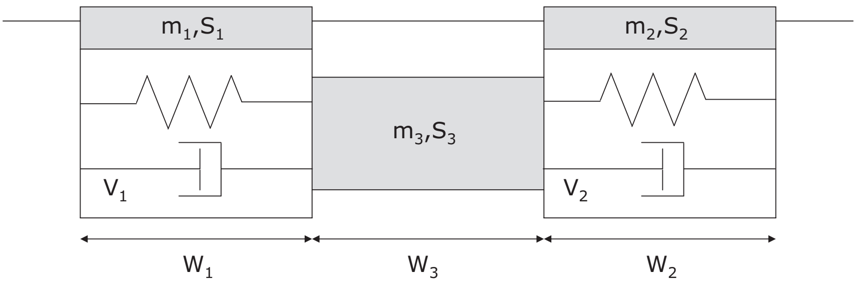

Figure 2.11: Two coupled spanwise Helmholtz resonators.

written as:

$$\frac{d}{dt}\int\int\int_V \rho dV = -\int\int_S \rho\vec{u}\cdot\vec{n}dS, \tag{2.10}$$

where S is a control surface enclosing V and $\vec{n}$ is the outer normal of S. Using a linear approximation and assuming uniform density ρ and velocity u and harmonic disturbances, Eq. (2.10) can be rewritten for the left and right resonator, respectively, as:

$$i\omega\frac{V_1}{c^2}p_1 = -\rho_0 u_1 S_1 - \rho_0 u_3 S_3 \tag{2.11}$$

$$i\omega\frac{V_2}{c^2}p_2 = -\rho_0 u_2 S_2 + \rho_0 u_3 S_3. \tag{2.12}$$

The only difference between a completely separate resonator and the coupled system is the right hand term $\rho_0 u_3 S_3$.

Application of the momentum law in a resonator neck opening yields in linear approximation:

$$\rho_0\frac{\partial u}{\partial t} = -\frac{\partial p}{\partial x}. \tag{2.13}$$

Assuming harmonic disturbances will give the following equations for the left and right resonator neck opening:

$$i\omega\rho_0 u_1 = \frac{p_1}{L_1'} \tag{2.14}$$

$$i\omega\rho_0 u_2 = \frac{p_2}{L_2'}. \tag{2.15}$$

Here $L' = L + l$ is the modified height of the oscillation mass in the cavity neck, as also used in Eq. (2.1). Application of the momentum law on the coupled mass in the center section yields:

$$i\omega\rho_0 u_3 = \frac{p_1 - p_2}{W_3}. \tag{2.16}$$

The two mass conservation Eqs. (2.11), (2.12) and the three momentum conservations Eqs. (2.14), (2.15) and (2.16) yield the following system:

$$\begin{bmatrix} i\omega\frac{V_1}{c^2} & \rho_0 S_1 & 0 & 0 & \rho_0 S_3 \\ 1 & -i\omega\rho_0 L_1' & 0 & 0 & 0 \\ 0 & 0 & i\omega\frac{V_2}{c^2} & \rho_0 S_2 & -\rho_0 S_3 \\ 0 & 0 & 1 & -i\omega\rho_0 L_2' & 0 \\ 1 & 0 & -1 & 0 & i\omega\rho_0 W_3 \end{bmatrix}\begin{bmatrix} p_1 \\ u_1 \\ p_2 \\ u_2 \\ u_3 \end{bmatrix} = \vec{0}. \tag{2.17}$$

The geometric setup of the model of figure 2.11 depends on the width W_3 and area S_3 of the inter-resonator section and width of the resonator section W_1. The influence of these parameters on the frequency response is investigated by introducing the non-dimensionalized width $\alpha_1 = \frac{W_1}{W}$ and $\alpha_3 = \frac{W_3}{W}$, and non-dimensionalized effective area $\gamma = \frac{S_3}{A}$, where A is the cross sectional area of the cavity. The model is assumed to be geometrically symmetric so that $W_1 = W_2$, $V_1 = V_2$, $S_1 = S_2$ and $L'_1 = L'_2 = L'$.

Solving the system of Eq. 2.17 for $f = \frac{\omega}{2\pi}$ yields an expression for the natural frequency:

$$f_2 = \frac{c}{2\pi}\sqrt{\frac{S}{VL'} + \frac{E}{W^2}}, \tag{2.18}$$

where

$$E = \left(\frac{2\gamma}{\alpha_1\alpha_3}\right). \tag{2.19}$$

Compared to the resonance frequency of a single Helmholtz resonator (Eq. (2.1)) there is an additional term depending on the spanwise length W.

The natural resonance frequency for a system of arbitrary number of resonators in the cavity span $n = 1, 2, 3, ..$ can be found by organizing the section width into a number of the dual resonator systems of Eq. 2.18 with reduced total span $\frac{W}{n-1}$. This will give:

$$f_n = \frac{c}{2\pi}\sqrt{\frac{S}{VL'} + \frac{E\,(n-1)^2}{W^2}}. \tag{2.20}$$

For $n = 1$, Eq. 2.1 is retrieved.

Using spanwise integration of the ART results bandfiltered cavity volume shown in figure 2.9, the magnitudes of α_1, α_2 can be estimated. This will give $\alpha_1 \approx \frac{1}{\pi}, \alpha_3 \approx \frac{2}{\pi}$. Note that due to the gradual change in span, the widths of the inter-resonator and resonator sections do not add up to the total spanwise width exactly, but partly overlap. Filling in will give:

$$f_n = \frac{c}{2\pi}\sqrt{\frac{S}{VL'} + \beta\left(\frac{\pi\,(n-1)}{W}\right)^2}, \tag{2.21}$$

with β of order 1, accounting for variations in resonator effective cross-section and widths. The used lumped mass model derivation indicates that n interacting Helmholtz resonators are present in the span. It should be noted however that equation 2.21 can also be interpreted as combination of Helmholtz resonance and spanwise planar wave modes.

Table 2.4: Comparison analytical model multiple Helmholtz resonators with flow run higher mode frequencies, $\beta = 0.97$. Large (0.5 m) and small (0.3 m) span flow experiments included.

large span (0.5 m) nr. of sections	analytical freq. [Hz]	exp. freq. [Hz] (flow-run based)
1	830 (set)	830
2	897	900
3	1074	1050
4	1318	1300
5	1597	1600
6	1897	1900
small span (0.3 m) nr. of sections	analytical freq. [Hz]	exp. freq. [Hz] (flow-run based)
1	830 (set)	830
2	1006	1000
3	1408	1420

2.6.2 Comparison of model with experiment

The derived analytical model for multiple Helmholtz resonators of Eqs. 2.21 is compared with the experimental flow run results in table 2.4. When $\beta = 0.97$ is chosen, a good match with the experimentally obtained modes can be found.

Table 2.4 includes flow run data from the 0.3 m and 0.5 m span cavity flow run experiments. The base Helmholtz resonance effective length L' is set to match the base resonance frequency. The analytical resonance frequencies are all within a few percent of the observed experimental values. This result is obtained by using only one chosen variable β and thus the analytical model seems to be able to describe the observed physical behavior.

2.7 Conclusions

In this paper the aeroacoustic response of slender covered cavities has been presented. In the investigated geometries several aeroacoustic resonances occur. The base resonance mechanism is of a simple slender Helmholtz type. The higher resonances show spanwise variations that do not correspond to pure simple standing wave modes. All observed resonances are excited by the first stage hydrodynamic mode.

The acoustic response (no flow) of the geometry is simulated using a Lattice Boltzmann method. This simulation is validated by comparing it with an experimental acoustic response test. The acoustic simulations revealed the mechanism for the higher resonance modes of the flow experiments by frequency band-filtering the simulation pressure signal in the entire cavity internal volume. The cavity higher modes with spanwise variation can be interpreted as spanwise sections that act as separate Helmholtz resonators interacting with each other.

A lumped mass analytical model for the coupled resonator sections is derived based on the experimental and numerical results that matches the observed mode frequencies well. The resonance frequency depends on the cavity total spanwise width. In the limit of one resonator, the original slender Helmholtz equation is retrieved.

Acknowledgments

We would like to thank Prof. Hirschberg from Eindhoven University of Technology for the helpful advice on cavity acoustics and advice on design of the experimental setup. We also would like to thank Stefan Bernardi at the Delft university of Technology low speed laboratory for helping setting up the wind tunnel experiments. From Exa Corp. we would like to thank Dr. Bernd Crouse, Dr. David Freed and Gana Balasubramanian for the support. At the aerodynamics department of Delft University we would like to thank Dr. Leo Veldhuis for his helpful discussions and Prof. Fulvio Scarano for his experimental expertise.

Bibliography

[1] Rossiter, J. E., *Wind-tunnel experiments on the flow over rectangular cavities at subsonic and transonic speeds*, London, H.M.S.O., 1st ed., 1967, pp. 1-32.

[2] Noger, C., Patrat, J. C., Peube, J., and Peube, J. L., "Aeroacoustical study of the TGV pantograph recess," *Journal of Sound and Vibration*, Vol. 231, 2000, pp. 563–575.

[3] Radavich, P. M., Selamet, A., and Novak, J. M., "A computational approach for flow-acoustic coupling in closed side branches," *Journal of the Acoustical Society of America*, Vol. 109, No. 4, 2001, pp. 1343–1353.

[4] Dequand, S., Hulshoff, S. J., and Hirschberg, A., "Self-sustained oscillations in a closed side branch system," *Journal of Sound and Vibration*, Vol. 265, 2003, pp. 359–386.

[5] Dequand, S., Luo, X., Willems, J., and Hirschberg, A., "Helmholtz-Like Resonator Self-Sustained Oscillations, Part 1: Acoustical Measurements and Analytical Models," *AIAA journal*, Vol. 41, No. 3, March 2003, pp. 408–415.

[6] Dequand, S., Hulshoff, S., Kuijk van, H., Willems, J., and Hirschberg, A., "Helmholtz-Like Resonator Self-Sustained Oscillations, Part 2: Detailed Flow Measurements and Numerical Simulations," *AIAA journal*, Vol. 41, No. 3, March 2003, pp. 416–424.

[7] Dequand, S., Willems, J. F. H., Leroux, M., Vullings, R., van Weert, M., Thieulot, C., and Hirschberg, A., "Simplified models of flue instruments: Influence of mouth geometry on the sound source," *Journal of the Acoustical Society of America*, Vol. 113, No. 3, March 2003, pp. 1724–1735.

[8] Coltman, J. W., "Jet Drive Mechanism in Edge Tones and Organ Pipes," *Journal of the Acoustical Society of America*, Vol. 60, No. 3, 1976, pp. 725–733.

[9] Elder, S. A., "On the Mechanism of Sound Production in Organ Pipes," *Journal of the Acoustical Society of America*, Vol. 54, 1973, pp. 1554–1564.

[10] Crouse, B., Senthooran, S., Balasubramanian, G., Freed, D., Noelting, S., Mongeau, L., and Hong, J. S., "Sunroof Buffeting of a Simplified Car Model: Simulations of the Acoustic and Flow-Induced Responses," *SAE Technical Paper*, 2005-01-2498, 2005, doi:10.4271/2005-01-2498.

[11] Ricot, D., Maillard, V., and Bailly, C., "Numerical Simulation of the Unsteady Flow past a Cavity and Application to Sunroof Buffeting," *7th AIAA/CEAS Aeroacoustics Conference*, Maastricht, The Netherlands, May 2001, pp. 1–11, AIAA-2001-2112.

[12] Ingard, U., "On the theory and design of acoustic resonators," *Journal of the Acoustical Society of America*, Vol. 25, No. 6, November 1953, pp. 1037–1061.

[13] Howe, M. S., "Low Strouhal number instabilities of flow over apertures and wall cavities," *Journal of the Acoustical Society of America*, Vol. 102, No. 2, 1997, pp. 772–780.

[14] Kooijman, G., Hirschberg, A., and Golliard, J., "Acoustical response of orifices under grazing flow: Effect of boundary layer profile and edge geometry," *Journal of Sound and Vibration*, Vol. 315, 2008, pp. 849–874.

[15] Nelson, P. A., Halliwell, N. A., and Doak, P. E., "Fluid Dynamics of a Flow Excited Resonance, Part I: Experiment," *Journal of Sound and Vibration*, Vol. 78, No. 1, 1981, pp. 15–38.

[16] Nelson, P. A., Halliwell, N. A., and Doak, P. E., "Fluid Dynamics of a Flow Excited Resonance, Part II: Flow Acoustic Interaction," *Journal of Sound and Vibration*, Vol. 91, No. 3, 1983, pp. 375–402.

[17] Henderson, B. S., "Category 6 Automobile Noise Involving Feedback - Sound Generated by Low Speed Cavity Tones," NASA Techical Report, 2000, 95-100.

[18] Henderson, B. S., "Category 5: Sound Generation in Viscous Problems, Problem 2: Sound Generation by Flow over a Cavity," NASA Technical Report, 2004, 71-77.

[19] Mongeau, L., Bezemek, J. D., and Danforth, R., "Pressure Fluctuations in a Flow-Excited Door Gap Model," *SAE Technical Paper*, 971923, 1997, doi:10.4271/971923.

[20] Larchevêque, L., Sagaut, P., Lê, T. H., and Comte, P., "Large-eddy simulation of a compressible flow in a three dimensional open cavity at high Reynolds number," *Journal of Fluid Mechanics*, Vol. 516, 2004, pp. 265–301.

[21] Elder, S. A., Farabee, T. M., and DeMetz, F. C., "Mechanisms of Flow-excited Cavity Tones at Low Mach Number," *Journal of the Acoustical Society of America*, Vol. 72, No. 2, 1982, pp. 532–549.

[22] Gloerfelt, X., "Cavity noise," `http://sin-web.paris.ensam.fr/squelettes/ref_biblio/Gloerfelt_VKI_2009a.pdf` (date last viewed 04/25/12), 2009.

[23] White, F. M., *Viscous Fluid Flow*, McGraw-Hill, New York, 2nd ed., 1991, pp. 409, 413.

[24] Hirschberg, A. and Rienstra, S. W., "An introduction to aeroacoustics," `http://www.win.tue.nl/~sjoerdr/papers/les-swr-mh.pdf` (date last viewed 04/25/12), Eindhoven University of Technology, July 2004.

[25] Succi, S., *The lattice Boltzmann equation for fluid dynamics and beyond*, Oxford University Press, 2001, pp. 11-13.

[26] Crouse, B., Freed, D. M., Balasubramanian, G., Senthooran, S., Lew, P., and Mongeau, L., "Fundamental Aeroacoustic Capabilities of the Lattice-Boltzmann Method," *12th AIAA/CEAS Aeroacoustics Conference*, No. AIAA-2006-2571, Cambridge, Massachussets, May 2006, pp. 2571–2588.

[27] Berlanger, A., Meskine, M., Caruelle, B., and Debatin, K., *11th AIAA/CEAS Aeroacoustics Conference*, Monterey, California.

[28] da Silva, A. A. and Scavone, G. P., "Lattice Boltzmann simulations of the acoustic radiation from waveguides," *Journal of Physics A*, Vol. 40, 2007, pp. 397–408.

[29] Li, X. M., Leung, R. C., and So, R. M. C., "One-Step Aeroacoustics Simulation Using Lattice Boltzmann Method," *AIAA Journal*, Vol. 44, No. 1, January 2006, pp. 78–89.

Chapter 3

The influence of flexible seals on cavity resonance

This chapter is based on experiments conducted at TUDelft together with Andreas Hazir from FKFS, Stuttgart Germany.

3.1 Introduction

In automotive, the transmission of sound generated by cavity bodies into the interior is an important topic. A door gap cavity can produce or amplify sound, and flexible seals that are used as a closure can transmit this into the cabin [1]. Compliance can influence the flow-driven aeroacoustic response of cavities. Flexible seals could influence the compliance of the cavity volume and therefore modify the resonance properties, such as resonance frequency. Also, seals could provide an additional viscous acoustic loss. For rigid slender cavities, the dominant acoustic energy losses arise due to radiation losses of the non-compact opening slot instead of viscous or thermal losses [2], therefore the effect of seals on resonance amplitude is expected to be small. In this chapter, the effect of seals on resonance amplitude and frequency is investigated. Also, the sound transmission properties of seals are studied.

The experimental setup is described in section 3.2 and the flow induced response is given in section 3.3. The analysis of the seals is divided into two parts: in section 3.4 the influence of the presence of flexible seals on the resonance frequency and amplitude is investigated and in section 3.5 the sound transmission

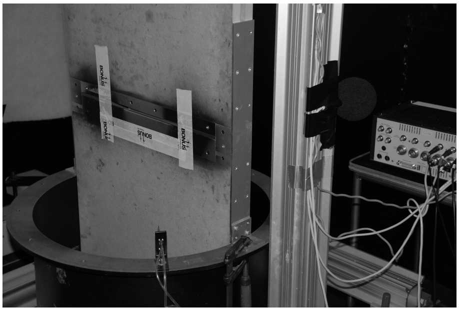

(a) front with resonator

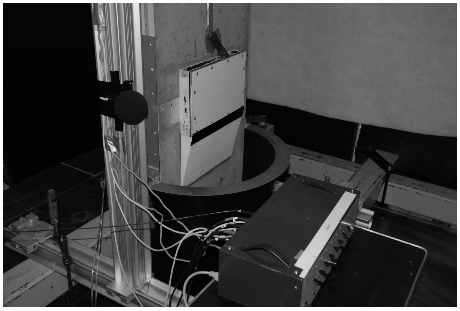

(b) back with acoustic cabin

Figure 3.1: Acoustic back cabin setups

properties of several seal designs are compared.

3.2 Experimental setup

In order to investigate the sound transmission of flexible seals in simplified door gap cavities an experimental campaign was conducted at the vertical wind tunnel of Delft University of Technology. The geometric setup consists of a splitter plate in an open low Mach number tunnel with a vertical outflow from 0 to 47 m/s through a circular opening of 0.6 m in diameter. The setup is depicted in figures 3.1 and 3.2. Due to the high contraction ratio of the settling chamber the quality of the airflow is high (low turbulence) and the tunnel is relatively silent with a background noise level of 20 dB at 25 m/s.

The boundary layer develops on the first section of the plate. By adjusting the length of the splitter plate and the location of trip wires the boundary layer is controlled in a precise and reproducible way. In the setup used for this publication, the splitter plate upstream flat plate section is set to 0.7 m and a 1 mm high zigzag type turbulator strip is located 10 cm from the splitter plate nose.

The cavity itself is constructed out of thick-walled aluminum to ensure enough rigidity to prevent fluid-structure resonance effects. Interchangeable parts are used to alter the neck geometry. The cavity body is slender, with spanwise width 250 mm, depth of 50 mm and streamwise length 32 mm. The cavity neck is equipped with sharp edges and a leading edge overhang, with an opening slot of 8 mm by 250 mm. Various seal designs have been tested, with variations in cross sectional shape (round or square), size, material thickness (2mm or 3mm) and material stiffness. The ones presented in this chapter are depicted in figure 3.3.

Due to the airflow being present on both sides of the splitter plate, the sound receiving cabin below the seal had to be small; 300x200x45 mm. The cabin is mounted on the opposite side of the splitter plate and the internal design of the cabins is depicted in the photographs of figure 3.4. Due to the small cabin size and the ambient noise, several measures were taken to minimize other sound sources

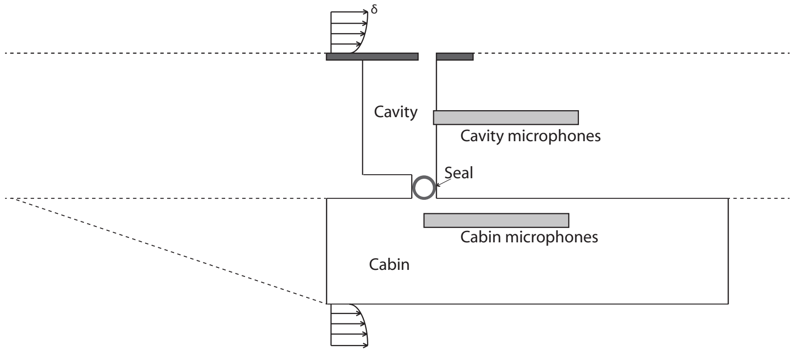

Figure 3.2: Overview of cavity and cabin with microphones

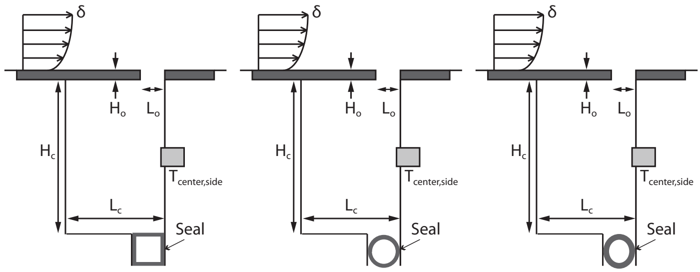

(a) square 2mm (b) round 2mm (c) round 3mm

Figure 3.3: Tested seal configurations

and reflections. The cabin was constructed with rubber padding, the cabin lid was made out of 10 mm thick aluminum and the outer shape of the cabin was streamlined to minimize aerodynamic noise. Two interior setups were implemented. One included acoustic foam and porous metal grading to minimize standing waves and dampen outside noise. The second one consisted of a solid aluminum block with a 10 mm wide channel carved 6 mm into the block.

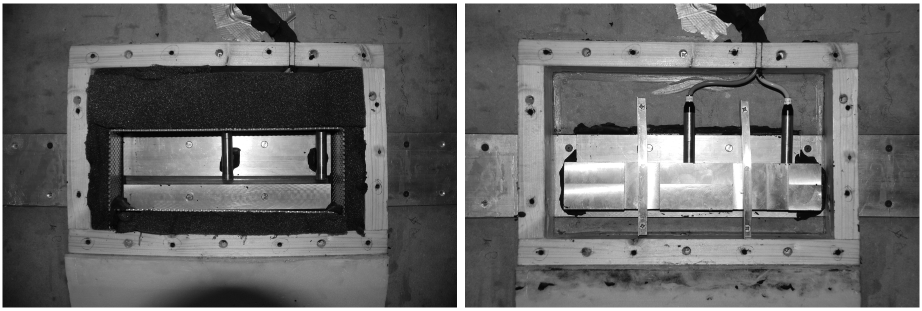

(a) padded acoustic cabin (b) aluminum block cabin

Figure 3.4: Acoustic back cabin setups

The sound transmission across the seal is measured using 5 microphones with a 5 kHz sample rate. The positioning of the internal microphones is indicated in figure 3.2. Two microphones are located in the cavity resonator body (in the spanwise center and on the spanwise side of the resonator), two were located in the cabin underneath the cavity resonator. One ambient noise level microphone is located outside the flow in the wind tunnel room.

3.3 Flow induced response

The flow induced response is depicted for all 5 microphones (for the 2mm, round seal configuration) in figure 3.5. The frequency of the excitation is shown at the horizontal axis and the free stream velocity on the vertical axis. The amplitude of the excitation in dB is indicated by level. Please note the differences in scaling (indicated next to each subfigure) for the various microphone locations. Both cavity microphones show a known resonance profile, with a Helmholtz resonance base mode and higher modes with spanwise variations. By comparing the MID (cabin center) with HR MID (resonator cavity center) spectrograms, one can observe a significant attenuation. In the cabin, the tonal modes are still transmitted, but the broadband level is of similar amplitude compared to the tonal components. This indicates that in the current design, the signal to noise level is not high. For low frequencies below 200 Hz, the overall sound pressure levels in the resonator cavity and cabin are of similar magnitude.

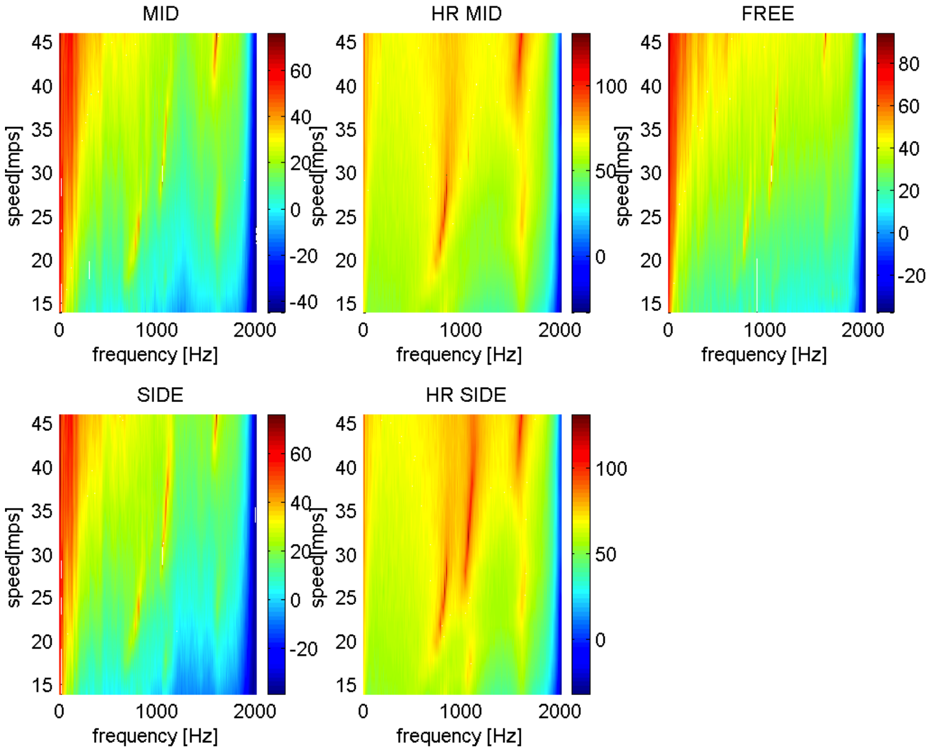

Figure 3.5: Observed resonance for the 2mm round seal configuration. Depicted are the cabin microphones (MID,SIDE), cavity resonator microphones (HR MID, HR SIDE), and outside microphones (FREE).

3.4 Influence of seals on cavity resonance frequency and amplitude

In order to evaluate the effect of flexible seals on resonance, 4 seal configurations with the padded cabin were selected. The configurations are three different seal designs as depicted in figure 3.3 and a fourth case where the cabin was closed off by a rigid metal body. The maximum sound pressure level amplitude and corresponding frequency as a function of free stream velocity are depicted in figure 3.6. The figure shows two resonance modes, with mode switching around 30 m/s. The effect of the seals on resonance amplitude cannot be distinguished, indicating that the increased sound damping of the seal is negligible compared to other acoustic losses [3]. The frequency of resonance is around one percent higher for the case without seal, which could be attributed to the lowered compliance due to the omission of seals that lower the resonance frequency. As the effect on the resonance frequency is low, one can conclude that the effect of the investigated

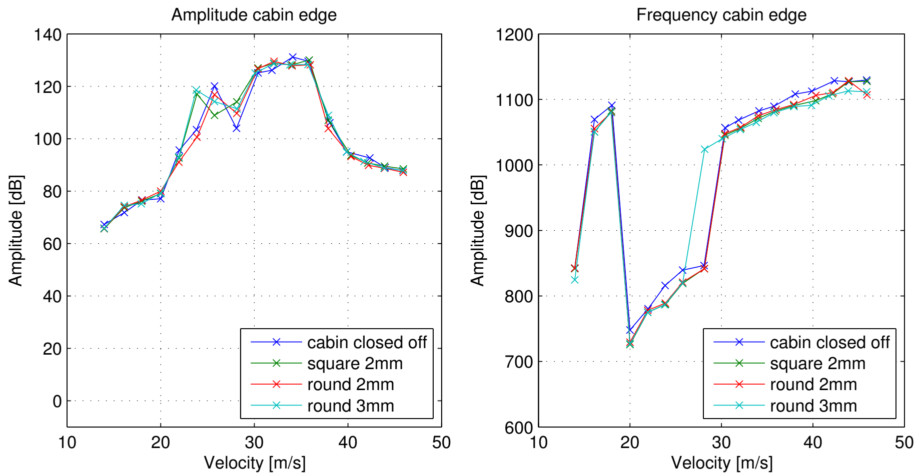

(a) Amplitude (b) Frequency

Figure 3.6: Amplitudes and frequencies of some padded cabin resonator configurations. Resonator edge microphone depicted.

flexible seals on the acoustic properties of the cabin is negligible.

3.5 Effect of seal design on sound transmission through the seal

In the currently presented experimented design, the small cabin and low signal to noise levels has made it difficult to evaluate the differences in sound transmission properties of the various seals. The aluminum block cabin is used in the sound transmission analysis due to the slightly better signal to noise ratio compared to the padded cabin setup. In order to evaluate sound attenuation, the first and second resonance mode were analyzed separately by band filtering around the corresponding resonance frequency. Resonator and aluminum block cabin sound pressure levels are depicted in figure 3.7 and the reduction in sound pressure level is shown in figure 3.8. Both resonance modes show a similar sound attenuation behavior, with the square 2 mm seal design having the highest attenuation, followed by the round 2 mm seal. The round 3 mm seal shows the lowest attenuation. It is currently unclear why the thicker seal has less attenuation.

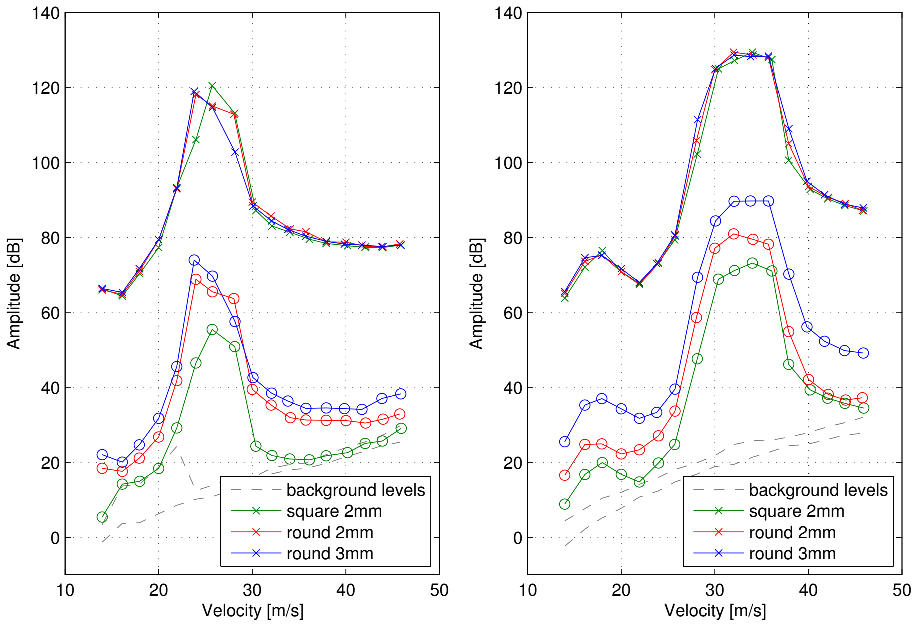

(a) Center microphone, mode 1 (600-900 Hz band-filtered)

(b) Edge microphone, mode 2 (900-1300 Hz band-filtered)

Figure 3.7: Amplitudes, resonator signals indicated by × symbol, acoustic cabin signals indicated by ∘ symbol. Background levels indicated by grey dashed lines.

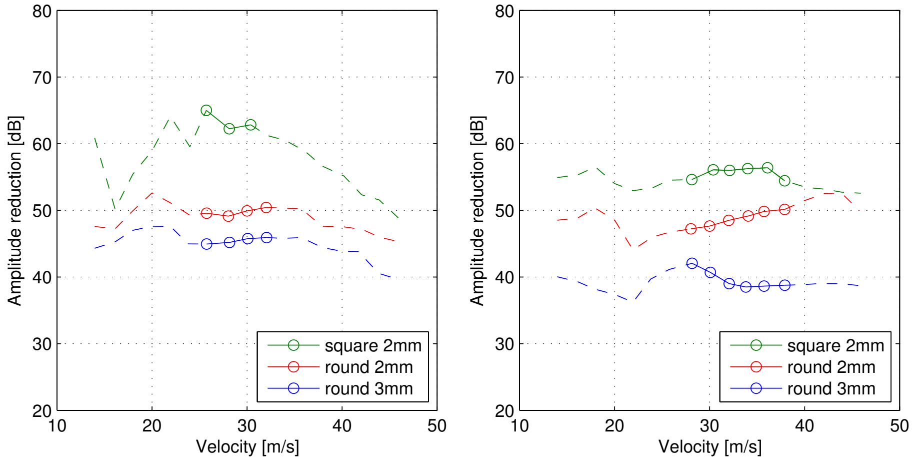

(a) center microphones, mode 1 (600-900 Hz band-filtered) (b) edge microphones, mode 2 (900-1300 Hz band-filtered)

Figure 3.8: Amplitude reduction, cabin signals which are less than 10 dB above the background noise are dashed.

3.6 Conclusions and recommendations

An initial experimental study has been performed using a slotted cavity with back cabin in a blown splitter plate with various seal designs in between the two volumes. The influence of the investigated flexible seals on the cavity aeroacoustic response amplitude is minimal. The presence of flexible seals slightly lowers the resonance frequency, which can be expected due to the higher cavity compliance. The sound transmission through the seal is masked by the present ambient sound field. For the aluminum block cavity, differences between transmission properties of the seals have been measured. A square seal showed more attenuation than a rounded seal. Interestingly, a round 3 mm seal showed less attenuation than a round 2mm seal. The reason for this effect is currently unclear.

For future investigations, an experimental campaign in an acoustic chamber with a single sided blown flow is recommended. In this way, the acoustic cabin can also be larger and better insulated to prevent sound from other transmission paths than the seal. A finite element analysis of the various seal designs could improve understanding of the differences in attenuation properties.

Acknowledgments

I would like to sincerely thank Andreas Hazir and Professor Wiedemann for their enjoyable cooperation in research and the availability of the measurement equipment.

Bibliography

[1] Mongeau, L., Bezemek, J. D., and Danforth, R., "Pressure Fluctuations in a Flow-Excited Door Gap Model," *SAE Technical Paper*, 971923, 1997, doi:10.4271/971923.

[2] Kooijman, G., Hirschberg, A., and Golliard, J., "Acoustical response of orifices under grazing flow: Effect of boundary layer profile and geometry," *Journal of Sound and Vibration*, Vol. 315, 2008, pp. 849–874.

[3] Howe, M. S., "Low Strouhal number instabilities of flow over apertures and wall cavities," *Journal of the Acoustical Society of America*, Vol. 102, No. 2, 1997, pp. 772–780.

Part II

Passive and active control of cavity noise

Chapter 4

Influence of opening geometry and flow conditions on resonance behavior of partially covered slender cavities

This chapter is based on the published journal paper:

The aeroacoustic resonance behavior of partially covered slender cavities
A.T. de Jong, H. Bijl, F. Scarano
Experiments in Fluids
Volume 51, Issue 5 (2011), Pages 1353-1367

(Submitted 26 October 2010, revised 13 April 2011, accepted 21 June 2011)

The present investigation focuses on the aeroacoustic resonance of cavities with a width much larger than their length or depth and partially covered, as often encountered in automotive door gaps. The cavities are under influence of a low Mach number flow with a relatively thick boundary layer. Under certain conditions, these cavities can acoustically resonate with the flow. The upstream and downstream edge of the opening as well as the cover lip overhang location and boundary layer thickness are parametrically varied in an experimental campaign and the effect of the parameters on the resonance amplitude is investigated. Slen-

der rectangular cavity geometries with an opening length of 8 mm and spanwise width of 500 mm are used. The cavity flow induced acoustic response is measured with pressure transducers at different spanwise locations inside the cavity. Hot-wire measurements are performed to quantify the boundary layer characteristics. Furthermore, high speed time resolved Particle Image velocimetry is used to capture the instantaneous velocity field around the opening geometries. When the boundary layer thickness is increased, the cavity resonance amplitude diminishes. The cover lip overhang location has a large influence on the resonance response, which can be attributed to changes in the cavity driven flow properties. Rounding of the upstream edge promotes resonance, whereas rounding of the downstream edge can diminish it. A possible explanation of the phenomenon is given on the basis of the PIV observations.

4.1 Introduction

The flow over cavities is often studied for their intrinsic resonant behavior and the consequent significance of aeroacoustic noise production [1]. Aeroacoustic research has focussed on a number of different cavity geometries, like for example cavities with cylindrical openings [2]. In the aircraft industry, most focus has been put on open shallow cavities. These cavities often resemble aircraft bays and landing gear wheel wells [3]. Deep cavity resonance has also been a topic of interest, for example in side branches of pipe systems [4, 5]. Generic partially covered cavity geometries have also been investigated in detail, where the cavity often behaves like a Helmholtz resonator. For example Dequand et. al. [6, 7] investigated the resonance lock-on amplitude of several rectangular Helmholtz resonator geometries under a thin boundary layer flow compared to the opening length. Examples of applications using partially covered cavities are the sound generation in flute like instruments [8, 9, 10], the buffeting of open car sunroofs and side windows [11, 12] and Helmholtz resonators used in acoustic liners [13].

The current investigation concerns the flow induced resonance behavior of cavity configurations that are slender (width much larger than length or depth) and under influence of a flow with a thick boundary layer compared to opening length and partially covered. These configurations are relevant in the automotive industry because they represent the properties of automobile door and trunk lid gaps. Under certain conditions, these gaps can resonate with the flow. Door gap like configurations with a high aspect ratio have not been examined in great detail. Nelson [14, 15] experimentally analyzed a Helmholtz resonator with a slotted opening with an aspect ratio of 60 in the center of the resonator. Laser Doppler velocimetry was used and the configuration was excited by a grazing flow of 17 to 26 m/s with a single boundary layer thickness. A detailed analysis of the flow was executed for this single configuration. In addition, Henderson [16, 17] presented benchmark experimental data of a resonator with an aspect ratio 55 opening and a thick and a thin boundary layer flow of 45 to 60 m/s. Only one single configuration was investigated, with a cover lip mounted from the upstream edge. A number of resonance modes were found, however the physical mechanism for a number of these modes was not entirely clear. Mongeau et. al. [18] show experimental results of a varying aspect ratio around 30 that resembles a door gap, including a seal fixture. The cover lip was mounted on the upstream edge and the downstream edge was varied between a 90 degree sharp corner and a 45 degree one. The effect of the boundary layer thickness was not investigated and the flow speed was 16 - 43 m/s. The cavity only showed a passive linear response to the outside flow.

The effect of the boundary layer characteristics is known for cavities of non-slender open type. For open cavities, it is known that the boundary layer has a large influence on the resonance behavior [19]. For a non-slender resonator, Kooijman et. al. [20] showed that by increasing the boundary layer momentum thickness compared to the opening length, the instability of the opening shear layer is reduced. Howe's theory [21] indicated that an increased aspect ratio modifies the impedance, thereby reducing the sensitivity to resonate due to a grazing flow. In fact, in general automotive door gaps only show a passive response to the flow, although there are cases where a resonance lock-on can occur [22]. For the slender cavities and in particular with partial cover of the leading and trailing edge, the influence of the boundary layer properties on the resonance behavior is not sufficiently explored. In the present study attention is focussed upon the effect of the boundary layer thickness to the onset of flow oscillations in the cavity.

For shallow open cavities and deep open cavities, like for example side-branches in pipe systems, the influence of the design of the upstream and downstream opening edges is considerable [5, 20, 23, 24]. The design of the opening edges are expected to have a large influence on gap resonance behavior as well, but this has not been investigated in detail to date. Mongeau showed that a modification of the trailing edge has an influence on the response amplitude. Differences in resonance response between the various investigated geometries [14, 15, 16, 17, 18] cannot be fully explained in terms of cavity dimensions and flow properties alone. Therefore in the current investigation, three parameters concerning the cavity opening geometry are varied to investigate the effect of the opening design on the resonance properties. Both the upstream and downstream edges are varied. In addition, the cover lip overhang location is moved between the upstream and downstream edges in order to investigate the effect of the opening geometry in more detail.

The current investigation concerns door gap cavity resonance behavior in order to reveal the influence of upstream and downstream opening geometry, opening location with respect to the underlying cavity and relative boundary layer thickness on resonance. The study is conducted on a simplified geometry, where the parameters of interest are systematically varied. The opening edges are implemented with sharp or round edges and the cover overhang location is moved between the upstream and downstream edges. PIV is known to be a valuable tool to assess the fluid mechanic behavior of cavities [25]. In order to quantify the effects of the parametric variations, high speed PIV is adopted to measure the flow field velocity above and inside the cavity.

4.2 Cavity excitation and resonance theory

The fluid enclosed in the volume of a cavity can act as an acoustic resonator to an excitation source in the cavity neck region. Excitation can either be due to a feedback mechanism of the perturbed shear layer or due to passive excitation by the pressure fluctuations in the turbulent flow (turbulent rumble) [26]. In case of feedback, the shear layer can roll up into discrete vortices impinging on the downstream edge coherently (a Rossiter mode) [3], or exhibit a flapping shear layer motion. In the low Mach number limit, a feedback mode corresponds to excitation at a fixed Strouhal number $Sr = \frac{fL_o}{U_\infty}$, with f the resonance frequency, L_o the cavity streamwise opening length and U_∞ the free stream velocity. If the excitation frequency is close to a resonance frequency, lock-on can occur and the system can resonate. In case of turbulent rumble the resonance should effectively be independent of velocity [26].

The resonance mechanism can either be of a Helmholtz type or of a standing wave type. In Helmholtz-like resonance the mass of air in the cavity is coherently compressed and expanded. The equation for a Helmholtz resonator is [22]:

$$f_H = \frac{c}{2\pi}\sqrt{\frac{S}{VH'_o}}. \tag{4.1}$$

Here V is the cavity volume, S is the cavity neck surface area and H'_o is the corrected vertical length of the cavity neck. The relation between the actual vertical cavity neck height H_o and H'_o is $H'_o = H_o + h$, where h is an end effect correction factor to account for the added resonating mass above and below the opening. For non-slender openings it is based on the surface area $h \propto \sqrt{S}$, whereas in the slotted opening of the current investigation, it is assumed to be related to the opening length only $h \propto L_o$ and independent of the slot width W [13]. For the currently investigated covered slender cavities, higher frequency resonance modes with spanwise variations can occur, where the mode frequency is dependent on the spanwise width [27]. The focus of the current investigation is the base Helmholtz mode.

For the currently investigated covered slender cavities, higher resonance modes with spanwise variations can be described by the following equation [27]:

$$f_n = \frac{c}{2\pi}\sqrt{\frac{S}{VH'_o} + \beta\left(\frac{\pi(n-1)}{W}\right)^2}, \tag{4.2}$$

with β of order 1, accounting for variations in resonator effective cross-section and widths. Note that this equation can be interpreted as the interaction between spanwise standing waves and Helmholtz resonance or as individual sections of the cavity acting as separate Helmholtz resonators that are coupled. The first $n = 1$ mode has constant properties along the span and corresponds to the Helmholtz mode. For the $n = 2$ mode, the opposite ends of the cavity are in anti-phase.

The normalized acoustic velocity amplitude $\frac{|d\epsilon/dt|}{U_\infty}$ in the neck region for a lumped mass system is a good indicator to evaluate the degree of acoustic lock-on [6]. It can be estimated by:

$$\frac{|d\epsilon/dt|}{U_\infty} \approx \frac{\frac{V_{cav}}{\rho_0 S}\left|\frac{d\rho}{dt}\right|}{U_\infty} = \frac{1}{2}\sqrt{\frac{V_{cav}}{V_m}}\frac{|p'|}{q}M \tag{4.3}$$

With ϵ the acoustic displacement, $|p'|$ the amplitude of the cavity acoustic excitation, $q = \frac{1}{2}\rho U_\infty^2$ the dynamic pressure, M the Mach number, $V_{cav} = L_c H_c W$ the cavity volume, $V_m = L_o H_o' W$ the modified volume of the opening section. In the derivation, conservation of mass in the resonator is used. Also $dp = c^2 d\rho$ and equation 4.1 for the Helmholtz resonator are used.

To whether or not a cavity will have resonance a linear stability analysis of the shear layer over the opening can be employed. Using linear stability analysis, Michalke [28, 29, 30] derived the stability properties of shear layers with a tangent hyperbolic (tanh) profile. This theory is further used by Bruggeman [31] and Kooijman et. al. [20] for side branches in pipe flow. The tanh profile is stable for Strouhal numbers below $Sr_{\theta,max} \equiv \frac{2\pi f\theta}{\Delta U} = 0.25$ [20].

In the next sections equation 4.1 will be used to predict the resonance frequency of the investigated configurations and equation 4.3 will be used to observe if the resonance amplitude is of high or low amplitude [6, 20]. Linear stability analysis of the tanh profile will be used to evaluate influence of the boundary layer properties on resonance and to evaluate the difference between shear layers of resonating and non-resonating geometries.

4.3 Experimental apparatus and procedure

4.3.1 Wind tunnel and model

Experiments are conducted in a low speed open jet wind tunnel at Delft University of Technology. The tunnel has a vertical outflow through a circular opening, 0.6 m in diameter. The tunnel contraction ratio is 250:1. The airflow in the test section has a turbulence intensity of 0.2 % and the wind tunnel acoustic background noise at 25 m/s is 20 dB.

The experimental geometry consists of a rectangular cavity partially covered by a rigid overhang plate attached at either the upstream or downstream corner of the cavity. The cavity opening is subjected to a flow with a thick (compared to the opening length L_o) boundary layer developed along a flat plate. Figure 4.1 shows the internal dimensions of the cavity. The aspect ratio of the cavity opening is $W/L_o = 62.5$, with a width of $W = 500$ mm. The base Helmholtz mode is expected to have coherent excitation along the span. The aspect ratio of the opening is chosen large enough $W/L_o >> 1$ to ensure to be clearly in the slender regime. As Mongeau [18] indicated, the ratio of internal cavity length to the opening length can be of importance. Therefore in the current investigation, the ratio of opening length and cavity internal length are set to resemble car

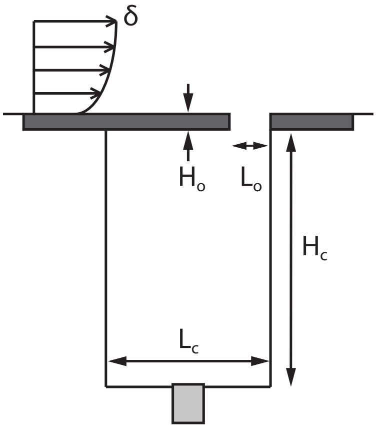

Figure 4.1: Cross sectional view of the cavity

door gaps more closely than similar configurations of [16, 17]. The cross-sectional internal dimensions are $L_c \times H_c = 32 \times 50$ mm and the opening dimensions are $L_o \times H_o = 8 \times 3.2$ mm. The expected Helmholtz resonance frequency based on equation 4.1 is around 800 Hz and expected velocity of maximum resonance is 25 m/s.

The model used in the wind tunnel is a cavity embedded in a splitter plate which has an elliptic nose cone. Figure 4.2 shows the setup mounted in the wind tunnel nozzle. The boundary layer develops on the first section of the splitter plate, upstream of the cavity. The boundary layer is controlled in a precise and reproducible way by adjusting the length of the upstream section of the plate L_p. In the setup used for this publication, it is chosen as $L_p = [0.2, 0.3, 0.5, 0.7, 0.9]$ m. A zigzag type turbulator strip of 1 mm height is located 10 cm downstream of the leading edge to trigger the transition of the laminar boundary layer into a turbulent one. By changing the plate length, the expected boundary layer thickness is varied. The maximum spanwise width of the cavity is set to 0.5 m, which is smaller than the 0.6 m width of the splitter plate itself to ensure constant flow properties along the span.

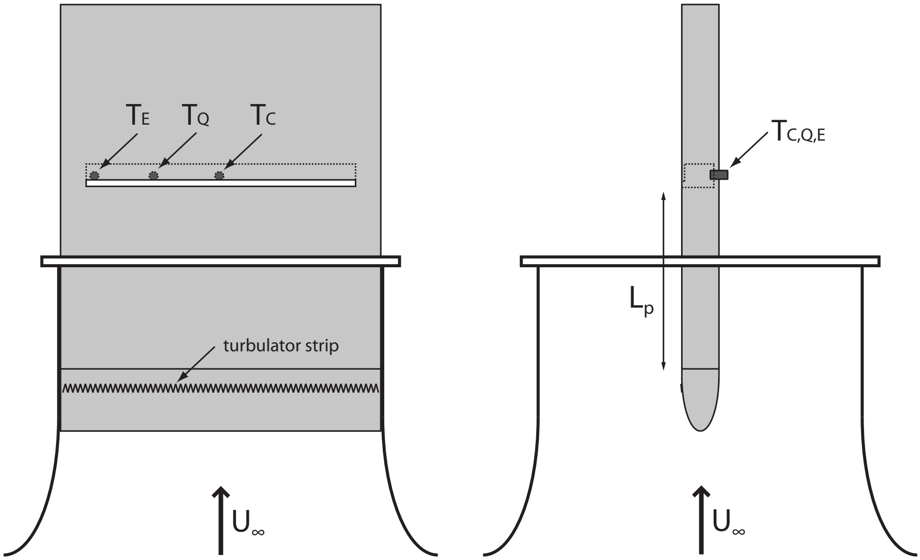

Figure 4.2: Front and side views of splitter plate with cavity mounted in wind tunnel nozzle. Cavity internal pressure transducer T_C, T_Q, T_E locations indicated by arrows.

The cavity itself is constructed out of thick-walled aluminum to ensure enough rigidity to prevent fluid-structure resonance effects. The cavity neck is equipped with sharp or round edges and an upstream or downstream cover lip overhang can be installed, leading to 8 different configurations investigated here. This is depicted in figure 4.3.

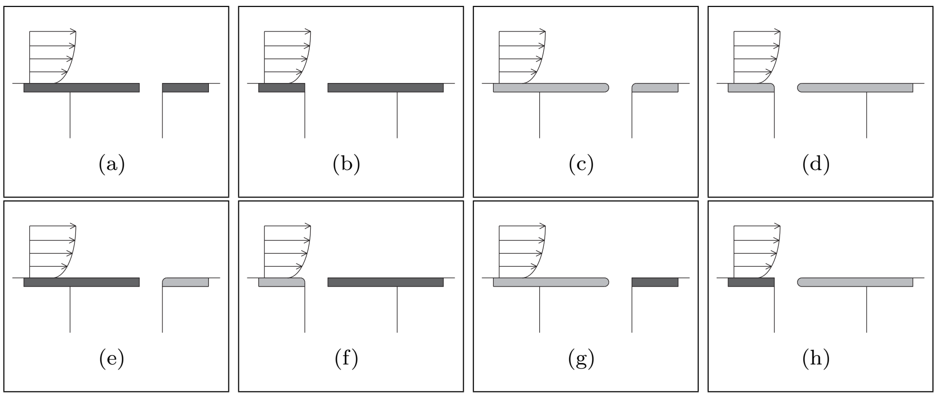

Figure 4.3: Cavity opening configurations

4.3.2 Measurement Equipment

The boundary layer characteristics are measured with a constant temperature hot-wire probe in absence of a cavity, for 4 different flow speeds (20, 24 , 30 and 40 m/s). Flow runs with open cavity have been performed to measure the flow induced sound pressure levels inside the cavity. The velocity is increased incrementally, up to the wind tunnel limit of approximately 47 m/s. The cavity internal sound pressure level is recorded using 3 Druck Inc. PDCR 22 pressure transducers. These are located at different spanwise locations (center, quarter, and edge) on the floor of the cavity, as indicated in figure 4.1.

In order to evaluate the flow in the opening region, high speed, time resolved particle image velocimetry (PIV) has been used. The PIV measurements are also used to capture the lower boundary layer characteristics and will be combined with hot-wire results in section 4.4. The PIV field of view is the region from 0 to 7 mm height in the boundary layer. Focus is put on the near wall region (0 to 0.5 mm) that is unresolved by hotwire measurements.

The illumination over an area of 25 by 16 mm is provided by a Quantronics Darwin-Duo 527 Nd:YLF laser. The field of view captures the cavity opening and the outer flow boundary layer up to 8 mm in height. The light sheet is positioned streamwise and perpendicular to the plate, with spanwise location 80 mm from the opening edge. A Photron Fastcam SA1.1 camera (1,024 x 1,024 pixels) is placed at a 90 degree angle with the illumination, and captures 1024x512 images. The illumination and recording devices are synchronized and controlled by a LaVision programmable timing unit (PTU v9) controlled by DaVis 7.3 software. Each measurement consists of 1000 image pairs at a recording frequency of 6000 Hz, which is sufficient to capture the temporal behavior of the flow (at approximately eight samples per resonance cycle). The double pulse interval is varied between 8 and 15 microseconds, depending on the velocity. The chosen magnification yields a typical digital resolution of 40 pixels/mm. The images were analyzed with the LaVision Davis 7.3 software, using a multi-step cross-correlation with a final interrogation window size of 16 by 16 pixels (0.4 by 0.4 mm^2) with 75% overlap.

4.4 Experimental results

The boundary layer properties as well as the cavity flow induced response are presented in the current section. The cavity properties are evaluated for a single configuration (depicted in figure 4.3(a)). The boundary layer is evaluated using hot-wire and PIV. The cavity resonance behavior is evaluated using the internal pressure transducers and the cavity opening flow field is evaluated using PIV results.

4.4.1 Incoming boundary layer

The boundary layer properties are obtained using both hot-wire and PIV measurements. Figure 4.4 illustrates the change in boundary layer mean flow charac-

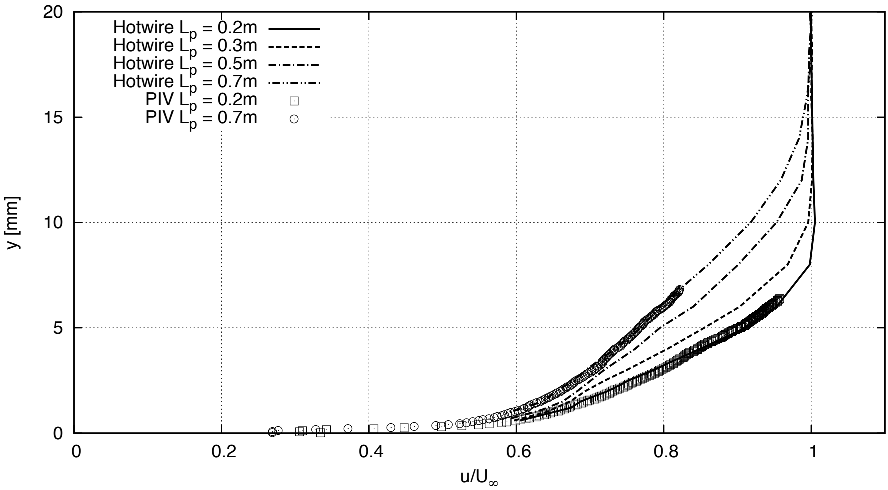

Figure 4.4: Experimental boundary layer mean profiles for different plate lengths

teristics due to variation in plate length L_p. PIV and hot-wire results are included in this figure. One can observe that the PIV results match the hot-wire results well.

Figure 4.5 shows a typical scaled logarithmic representation of the boundary layer properties, scaled by $u^+ = \frac{u}{v^*}$ and $y^+ = \frac{yv^*}{\nu}$, where v^* is the slip velocity and ν the kinematic viscosity [32]. There is a slightly higher wake component for the shortest ($L_c = 0.2$ m) plate. On overall, the shape of the boundary layer is a fully developed turbulent flat plate one, and the relative shape does not change with varying boundary layer thickness, indicating that self-similarity conditions are reached to a good degree.

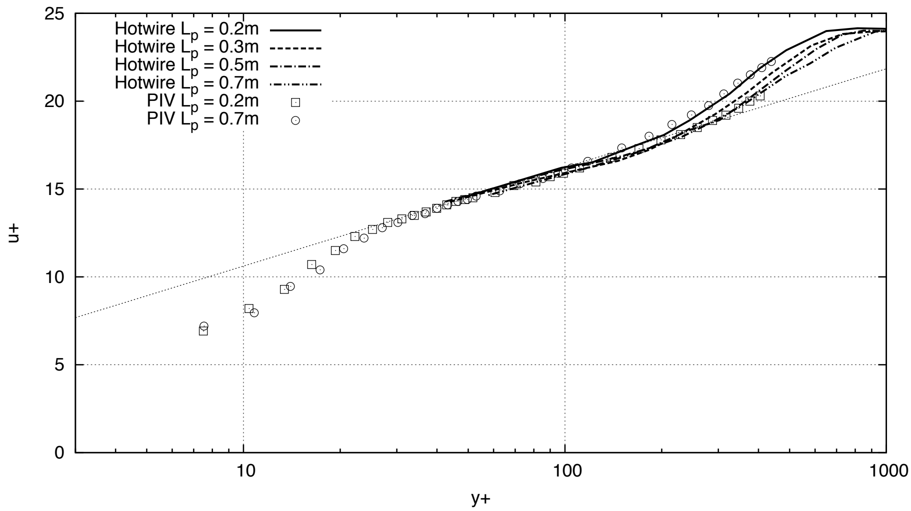

Figure 4.5: Experimental boundary layer scaled logarithmic profiles for different plate lengths, scaled as $u^+ = \frac{u}{v^*}$ and $y^+ = \frac{yv^*}{\nu}$. A dashed line indicating the turbulent log layer region [32] is added to the figure.

The fact that the boundary layer shape is similar for all measured boundary layers can also be observed by evaluating the boundary layer integral properties given in table 4.1. The following integral properties are evaluated; the displacement thickness δ^*, the momentum thickness θ, the shape factor H and the height at 99% of the mean flow δ_{99} , as defined in [32]. The shape factor does not vary, and corresponds to a value for a turbulent flat plate boundary layer [32]. Please note that in the table, the boundary layer properties for the 0.9m plate are not measured, but estimated based on data for all smaller plate lengths. The shape factor is set as the average of the measured boundary layer shape factors. The other integral properties are extrapolated using a least-squares linear regression through the data.

Table 4.1: Boundary layer properties at 24 m/s. Please note that 0.9m plate values are estimated using all other plate length data.

Plate length $[m]$	δ^*	θ	H	δ_{99}	θ/L_o
0.2	1.16	0.85	1.36	7.6	0.106
0.3	1.47	1.08	1.36	9.6	0.135
0.5	1.96	1.46	1.34	12.7	0.183
0.7	2.40	1.75	1.37	14.9	0.219
0.9*	2.81	2.05	1.36	17.3	0.256

*estimated

4.4.2 Pressure fluctuations in the cavity

The cavity flow induced resonance is investigated by measuring the internal pressure response. In the current section the results for the upstream overhang with sharp edges (depicted in figure 4.3(a)) and $L_p = 0.7$ m are presented. This configuration shows typical resonance properties and resembles previously investigated geometries most closely [16, 17].

The flow velocity is increased incrementally. The internal sound pressure levels of these velocity sweeps are gathered in spectrograms and given in figure 4.6 for all 3 pressure transducer locations (locations as indicated in figure 4.2). The frequency of the excitation is shown at the vertical axis and the free stream velocity on the horizontal one. The pressure amplitude of the excitation is indicated in dB, with standard $2 \cdot 10^{-5}$ Pa reference pressure. The figure shows several resonating modes with increasing velocity that have increasing mode frequencies. The first resonance mode is visible at all probe locations whereas for the higher modes some are not. This indicates a spanwise variation in the higher resonance modes.

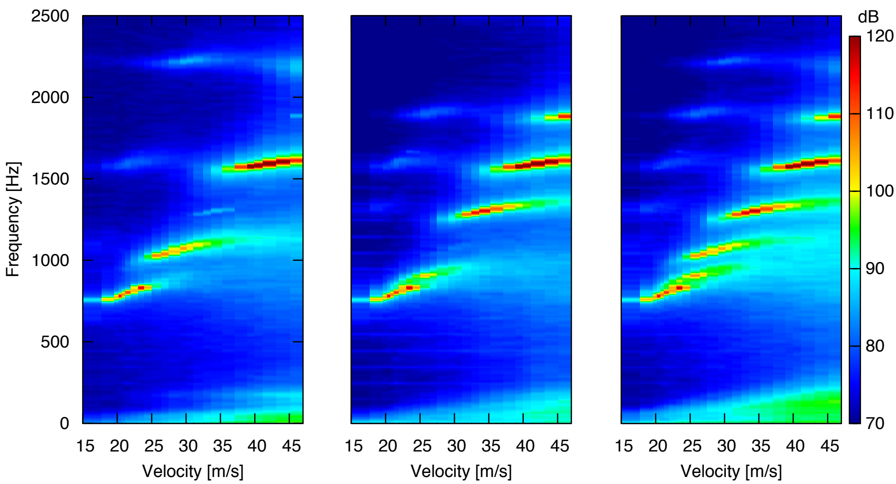

(a) T_C, Center location (b) T_Q, Quarter location (c) T_E, Edge location

Figure 4.6: Spectrograms of the three internal pressure probes, level by sound pressure $[dB]$

From figure 4.6 it is found that all the center points of the excitation modes show a linear relation between frequency and velocity. The Strouhal number $Sr = \frac{fL_o}{U_\infty}$ corresponding to this is approximately 0.3, indicating that all modes are hydrodynamically excited by the first stage Rossiter mode [3]. No excitation of the second stage Rossiter mode ($Sr \approx 0.7$) is present, although low amplitude onsets of resonance for this Strouhal number can be observed in the upper left part of the figures by low amplitude horizontal excitation lines.

The observed higher modes frequencies are corresponding to the description in section 4.2 [27] regarding equation 4.2. The modes can be interpreted as separate sections acting as individual resonators that are coupled to each other or as a superposition of spanwise modes and the base Helmholtz resonance mode. The 6 observed modes correspond to the $n = 1 - 6$ modes of equation 4.2. Modeled excitation frequencies are compared to the observed modes in table 4.2. The spanwise wavelength of the equivalent spanwise mode λ_W is given in the table, together with the corresponding pressure node locations. The corrected vertical length of the cavity neck H_o' is set to match modeled and observed base mode frequency, and is then used to determine the expected higher mode frequencies. The predicted spanwise variations are in agreement with the observed pressure transducer nodes of figure 4.6. The $n = 2, 4, 6$ modes have a pressure node at the center transducer location, and the $n = 3$ mode has a node at the quarter location. For the first $n = 1$ mode around 800 Hz, the whole cavity is coherently excited and no nodes are present. The 3 pressure transducer signals are also in phase at this mode. Thus for the base mode, acceptably uniform conditions across span are found.

Mode nr.	Modeled freq. [Hz]	Observed freq. [Hz]	Spanwise wavelength λ_W	Location pressure nodes
1	830 (set)	830	n/a (Helmholtz)	n/a
2	897	900	$2/1W_o$	$1/2W_o$
3	1074	1050	$2/2W_o$	$1/4W_o, 3/4W_o$
4	1318	1300	$2/3W_o$	$1/6W_o, 3/6W_o, 5/6W_o$
5	1597	1600	$2/4W_o$	$1/8W_o, 3/8W_o, 5/8W_o, ...$
6	1897	1900	$2/5W_o$	$1/10W_o, 3/10W_o, 5/10W_o, ...$

Table 4.2: Comparison analytical model multiple Helmholtz resonators with flow run higher mode frequencies, $\beta = 0.97$.

Even though the acoustic pressure amplitudes can be around 120 dB, it can be calculated that the energy transfer from flow to acoustics is low [6]. With the current cavity dimensions, equation 4.3 will give $\frac{|d\epsilon/dt|}{U_\infty} \approx 1 \cdot 10^{-2}$.

4.4.3 Shear layer characteristics

Both the time-resolved and phase averaged PIV flow fields are given in figure 4.7 for four phases during a resonance cycle. The volume flow through the opening is used as a phase averaging indicating. The volume flow is calculated from the inflow velocity at $x/L_o = 0 - 1, y/L_o = -0.5$. Using conservation of mass, the 4 chosen phases can be attributed with maximum cavity pressure, maximum outflow, minimum cavity pressure and maximum inflow.

The time-resolved visualizations resolve the coherent fluctuations in the incoming boundary layer and their interactions with the separated shear layer on the cavity opening. The turbulent structures interact strongly with the cavity shear layer. It is believed that these turbulent structures influence the resonance behavior in two ways. First of all the structures directly perturb the cavity, enabling resonance onset. They also break up the shear layer, thereby reducing the resonance amplitude. Turbulent structures can break up the spanwise coherency of the shear layer, however this effect cannot be measured from the current PIV measurements at a single span. The shear layer shows both shear flapping motion (first half of the opening) and vortex roll up (second half of the opening). The shed vortices are partly transported into the cavity due to the interaction with the downstream edge.

In the phase-averaged representation it is possible to identify more clearly the position of the shear layer corresponding to the 4 identified phases. Phase averaging distributes the vorticity so that a flapping shear layer with limited vortex roll-up appears in figure 4.7. The upstream part of the shear layer is stable and shows limited motion. Vortex roll-up occurs midway across the opening during the maximum outflow phase. This phase averaged shear layer pattern is corresponding to observations by [33]. The generated vortex is convected downstream and impinges on the downstream edge, where the vortex gets partly entrapped into the cavity. The influence of the interaction with turbulent fluctuations in the boundary layer manifests in a more diffuse shear layer compared to the instantaneous velocity fields.

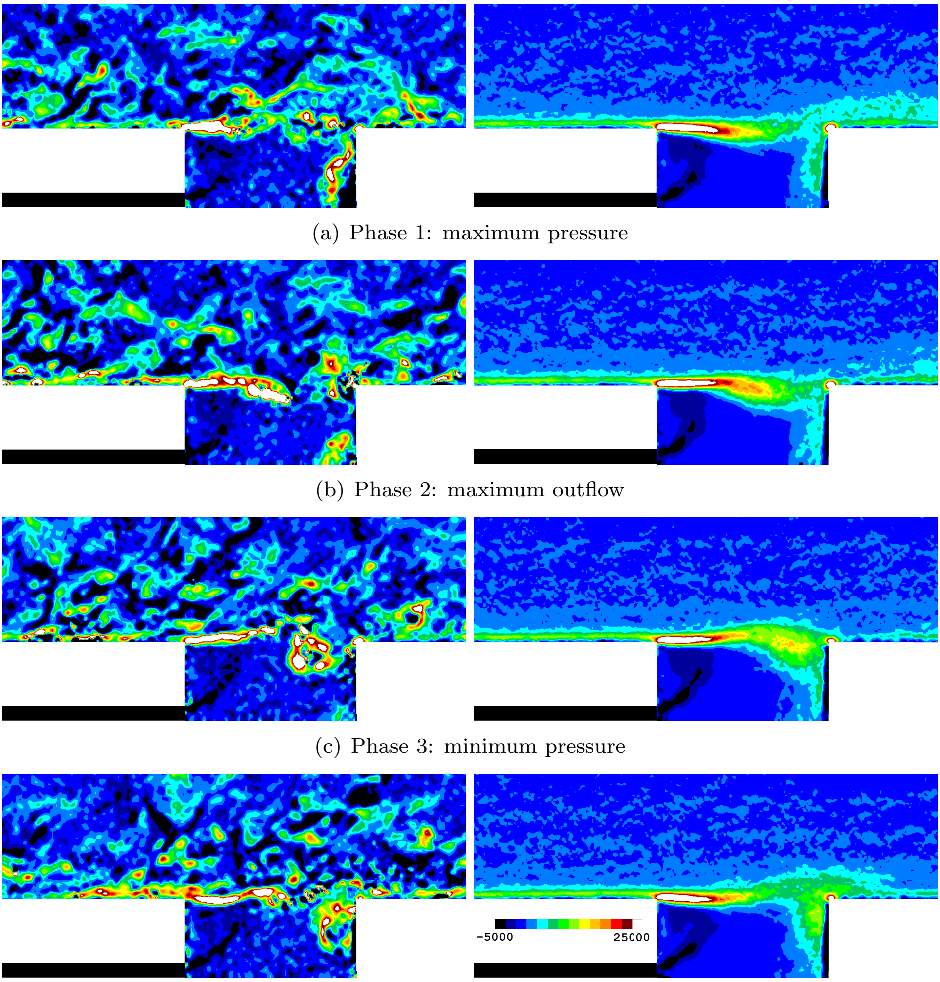

(a) Phase 1: maximum pressure

(b) Phase 2: maximum outflow

(c) Phase 3: minimum pressure

(d) Phase 4: maximum inflow

Figure 4.7: Phase-averaged and instantaneous PIV results, negative spanwise vorticity $-\omega_z$ indicated, sharp upstream edge overhang, rounded downstream edge setup used. $-\omega_z$ range -5000 to 25000 s^{-1}.

4.5 Parametric analysis of resonance modes

4.5.1 Cavity acoustic response

Figures 4.8 shows the influence of the boundary layer thickness and opening geometry on the excitation results. In this figure only the geometries with a cover lip attached at the upstream edge are considered. Figure 4.9 is a scaled representation of the amplitudes using equation 4.3, indicating the ratio of the acoustic velocity to the free stream velocity. One can observe that the acoustic amplitude in this case is relatively low, less than 1 percent of the mean flow in most cases.

With increasing boundary layer thickness, the resonance lock-on amplitudes diminish. Increasing the boundary layer thickness increases the stability of the shear layer, thereby reducing resonance [28, 29, 30]. Some modes diminish with the $\theta/L_o = 0.22$ boundary layer and the $\theta/L_o = 0.26$ m boundary layer shows no resonance lock-on anymore for all modes.

The θ/L_o resonance threshold values found here are above ones observed in literature for shallow cavities of around $(\theta/L_o)_{shallow} \approx 1 \cdot 10^{-2}$ to $6 \cdot 10^{-2}$ based on the current Reynolds number [24, 23, 34]. This indicates an increased tendency to lock-on due to coupling with a resonator volume.

In literature described in section 4.2 [28, 29, 30, 31, 20], a limit stability Strouhal number of $Sr_{\theta,max} = 0.25$ was found based on stability properties of a tanh profile. This Strouhal number corresponds to a limiting boundary layer momentum thickness $\theta_{max} = 1.2$ mm and ratio over opening of $\frac{\theta}{L_o}_{max} = 0.15$ above which no resonance is explected. According to figure 4.8 the stability limit is in the range $\frac{\theta}{L_o}_{max} = 0.18 - 0.26$, which is of the same order. The discrepancy can be attributed to the simplified tangent hyperbolic profile that does not match the real shear layer profile. Further analysis of the shear layer stability is given in section 4.5.2.

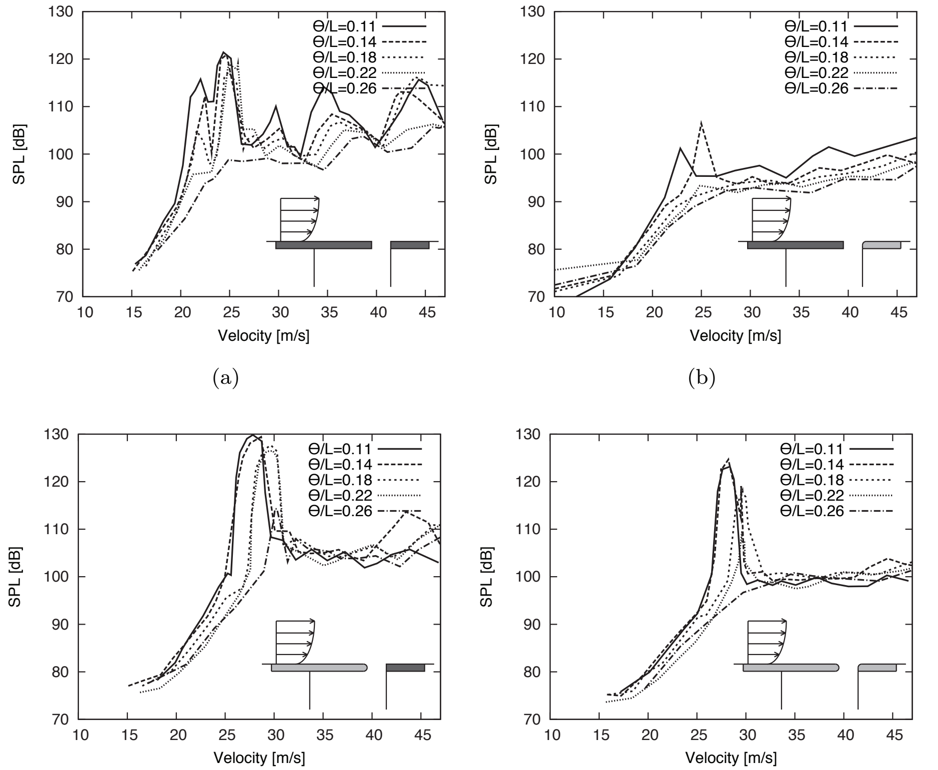

(a) (b)

(c) (d)

Figure 4.8: Maximum cavity internal pressure excitation amplitude all upstream cover lip overhang configurations. The opening configuration is depicted in the graph.

The shape of the upstream and downstream edges have different effects on the resonance amplitude. By comparing the upper and lower subfigures in figure 4.8 or 4.9, one can observe that rounding of the upstream edge will promote resonance. By comparing the left with the right subfigures one can observe that rounding of the downstream edge will diminish resonance. The cause of the effects of the upstream and downstream edges will be analyzed separately in section 4.5.3.

Only cases with upstream sharp edge overhang show additional modes with spanwise variations appearing at higher velocities. There is currently no explanation why the higher modes only were excited for these configurations. One possible reason can be the modification of the acoustic diffraction due to the edges promoting the onset of higher modes, but this is not confirmed by the present investigation.

The onset velocity for base resonance is higher for cavity geometries with open-

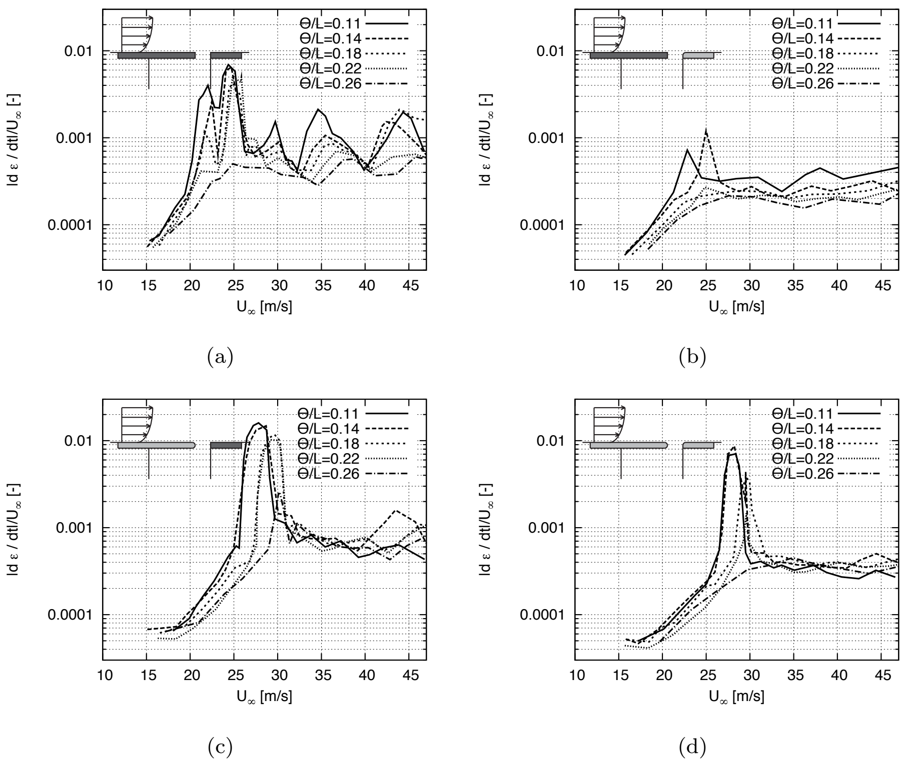

Figure 4.9: Maximum cavity internal pressure excitation amplitude all upstream cover lip overhang configurations, amplitude scaled as relative acoustic velocity magnitude $\frac{|d\epsilon/dt|}{U_\infty}$.

ing round-offs. Two reasons can be identified for this effect. The first possibility is a modification of the added resonating mass and thus a modification of the resonance frequency according to equation 4.1. Secondly the round-offs may modify the vortex convection time over the opening, leading to a change in excitation frequency. Figure 4.10 shows the spectra at maximum base mode resonance for the 3 resonating geometries. The frequency at maximum base mode resonance is similar for all rounded and sharp edged geometries (840 +/- 10 Hz), indicating that there is no significant change in added resonator mass. Therefore the effect must be attributed to a modified excitation frequency due to the round-offs. Similar effects have been observed by Dequand [6]. The change in excitation frequency can potentially be the result of a modified vortex path length due to the upstream and downstream round-offs and/or a modified vortex convection velocity over the opening.

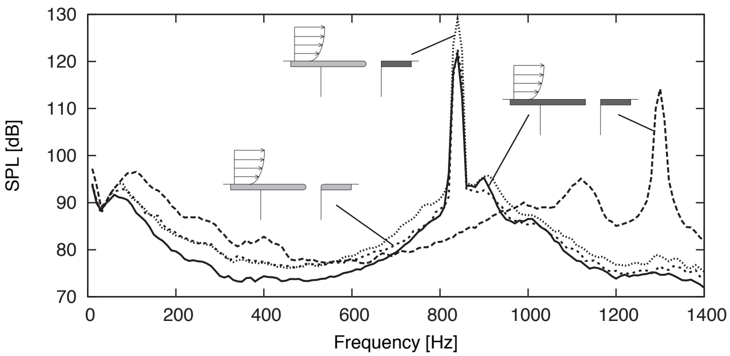

Figure 4.10: Pressure spectra inside cavity at maximum base mode resonance, $\theta/L_o = 0.11$. For sharp edge geometry, one higher mode at 35 m/s is included in addition to the base mode spectrum.

Figures 4.11 shows the influence of the boundary layer thickness and opening geometry for the cases with a cover lip attached at the downstream edge. Figure 4.12 is a scaled representation of the amplitudes using equation 4.3, indicating the ratio of the acoustic velocity to the free stream velocity. When comparing figures 4.8 and 4.11, the most striking point is that only geometries with an upstream overhang produce resonance lock-on. The geometries with a downstream cover lip overhang show no resonance for all boundary layer thicknesses. This indicates that the resonance behavior of a resonator cannot be estimated without considering the details of the opening geometry and flow inside the cavity body. The large influence of the cover lip location on the resonance behavior will be further analyzed in section 4.5.2.

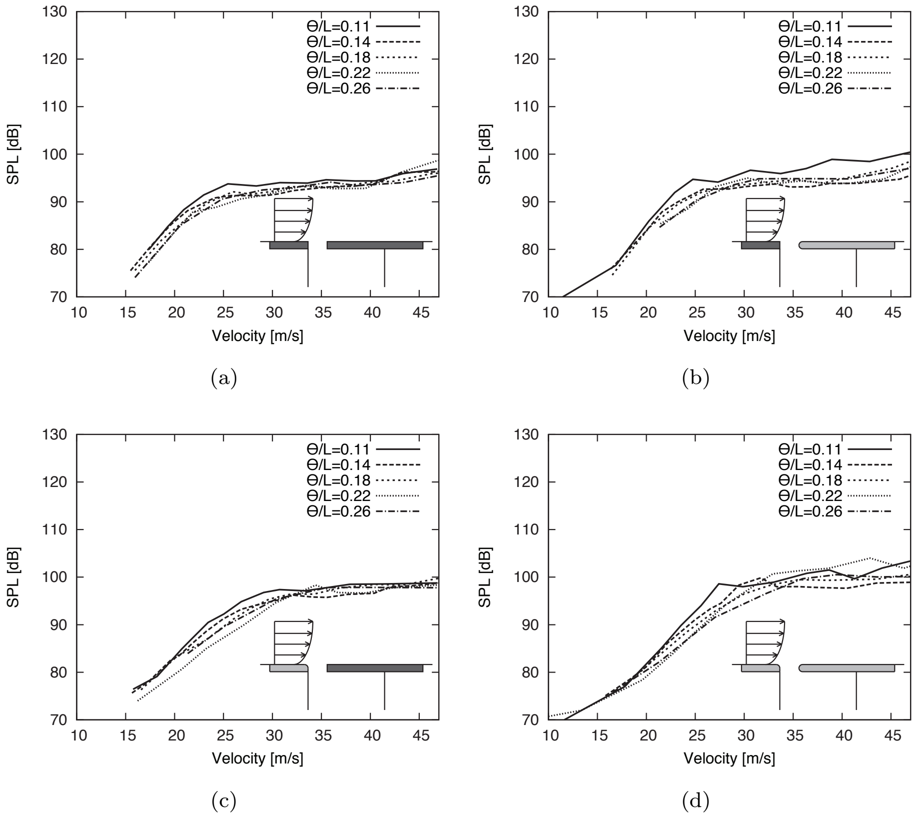

Figure 4.11: Maximum cavity internal pressure excitation amplitude all downstream cover lip overhang configurations.

Scaled figure 4.12 reveals an influence of the cavity geometry on the non-resonant behavior. Non-resonant areas can be identified by sections where $\left|d\epsilon/dt\right|/U_\infty$ is independent of the velocity magnitude U_∞. Table 4.3 gives the non-resonant average acoustic velocity $\left|d\epsilon/dt\right|/U_\infty$ for 30 - 45 m/s of the 4 largest boundary layer thicknesses ($L_p = 0.3, 0.5, 0.7, 0.9$ m). The table indicates that rounding of upstream as well as downstream edges increases the passive response of the cavity. The effect of rounding the downstream edge in this non-resonant case differs from the influence during resonance, where rounding of the downstream edge diminishes resonance. This difference can be explained due to the fact that acoustic energy losses (due to flow separation of the acoustic flow around the opening edges) are lower in case of a rounded downstream edge.

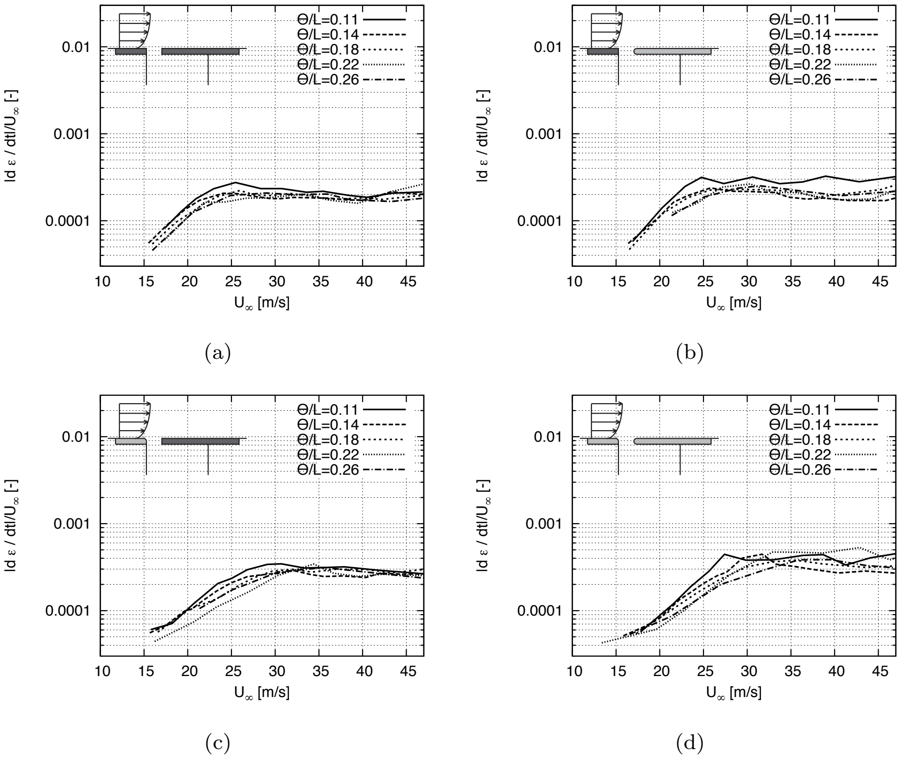

Figure 4.12: Maximum cavity internal pressure excitation amplitude all mixed upstream cover lip overhang configurations, amplitude scaled as relative acoustic velocity magnitude $\frac{|d\epsilon/dt|}{U_\infty}$.

	downstream edge sharp	downstream edge round
upstream edge sharp	$1.9 \cdot 10^{-3}$	$2.1 \cdot 10^{-3}$
upstream edge round	$2.8 \cdot 10^{-3}$	$3.6 \cdot 10^{-3}$

Table 4.3: Non-resonant acoustic velocity amplitude response due to boundary layer fluctuations, downstream cover overhang. Table indicates average $|d\epsilon/dt|/U_\infty$, for velocity range of 30-45 m/s and 4 largest boundary layer thicknesses.

4.5.2 Physical effect of cover lip overhang

Time averaged PIV results are used to explain the difference in response behavior between an upstream and downstream cover lip overhang. In the present research we observed no resonance for the downstream overhang locations, even though they are acoustically identical to resonating upstream overhang geometries. When comparing the flow field in the cavity opening, an interesting difference can be observed. Figure 4.13 shows the mean flow patterns for an upstream and downstream cover lip overhang setup. Note that the geometries with sharp edges are used in this comparison.

A large steady recirculation in the opening is observed in case of a downstream overhang, causing a local cavity driven flow. The driven flow component is accounting for an internal flow just below the opening of about $u_{int} \approx 0.1U_\infty$. In contrast, the upstream edge overhang shows an internal flow pattern with an inflow from the resonator volume and a separation region at the inner side of the upstream sidewall (visible in the lower left side of the figure 4.13(a)). This causes a considerably smaller cavity driven flow component compared to the downstream overhang geometry. The cavity driven flow influences the shear layer development along the opening. The effective shear is much lower for the downstream edge geometry and therefore the shear layer is more stable. This can be seen in the velocity plot of figure 4.14 and the effective shear given in figure 4.15. Here one can clearly observe a reduction in shear between the geometries close to the upstream edge. This can greatly modify the stability behavior of the shear layer. The vorticity thickness $\theta_\omega = \left(\frac{du}{dy}\right)_{max} / \left(U_\infty - u_{int}\right)$ is not changed when scaled with respect to the effective velocity difference of the outer and inner cavity flow $(U_\infty - u_{int})$.

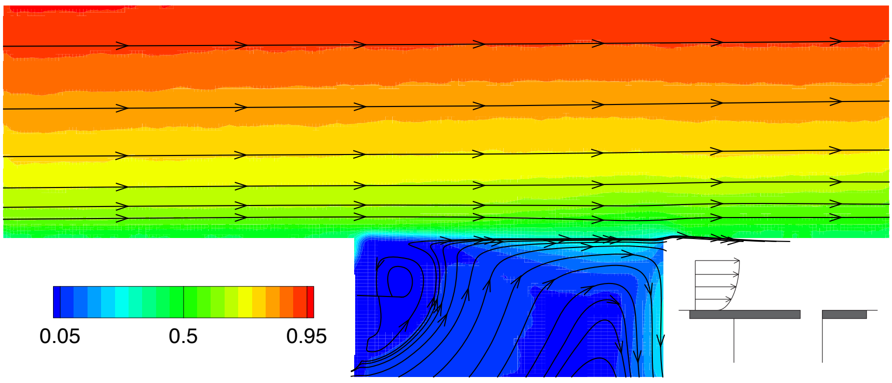

(a) Upstream cover lip overhang

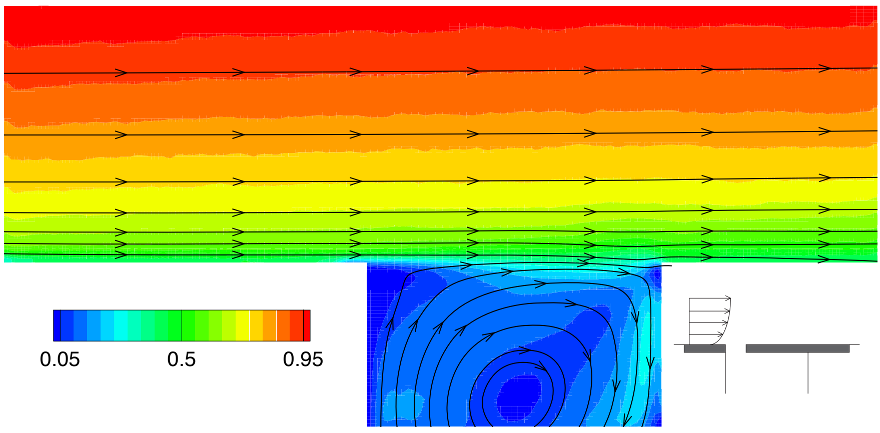

(b) Downstream cover lip overhang

Figure 4.13: Mean flow patterns in the cavity opening, color by normalized velocity magnitude $\frac{U}{U_\infty}$, with streamlines, sharp edges used.

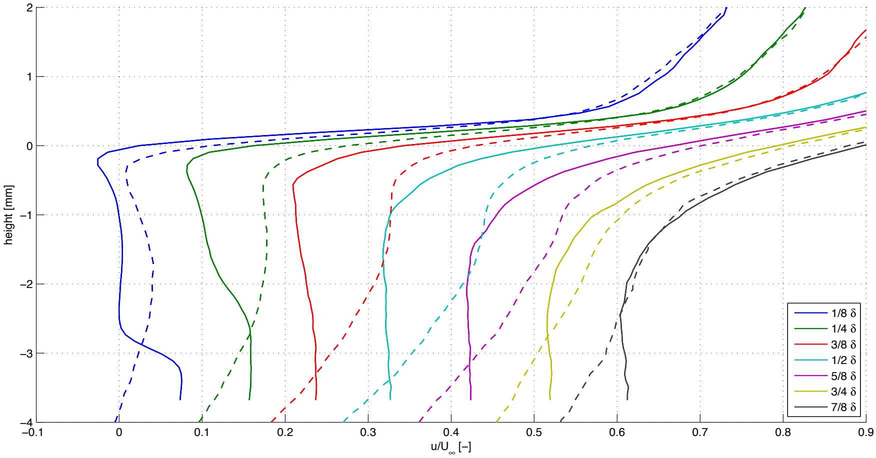

Figure 4.14: Comparison mean shear layer velocity profiles over the cavity opening. Plot in increments of $\Delta x = 1/8L_o$, starting at $x = 1/8L_o$. Lines separated by $0.1\frac{u}{U_\infty}$ shifts. Solid lines show upstream lip overhang, dashed downstream lip overhang.

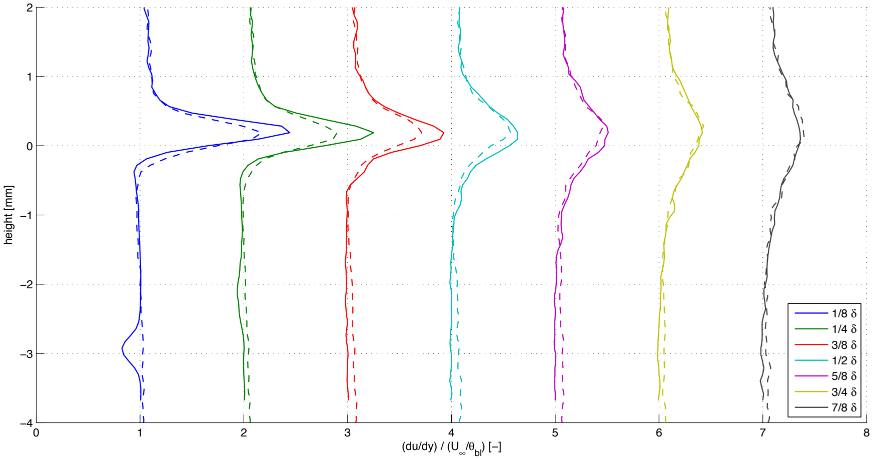

Figure 4.15: Comparison normalized shear patterns $\frac{(du/dy)}{U_\infty/\theta_{bl}}$, over the cavity opening, with θ_{bl} the upstream boundary layer momentum thickness. Plot in increments of $\Delta x = 1/8L_o$, starting at $x = 1/8L_o$. Lines separated by $1.0\frac{(du/dy)}{U_\infty/\theta_{bl}}$ shifts. Solid lines show upstream lip overhang, dashed downstream lip overhang.

In order to quantify the difference between upstream and downstream overhang resonance behavior, linear stability analysis of Michalke [28, 29, 30, 31, 20] is employed. To derive the properties of the current shear layer profiles is beyond the scope of the current work and planned for a future investigation. However, the tangent hyperbolic profile can be used to provide an estimation for the inherent stability of the shear layer. As mentioned before in section 4.2, Michalke found that a tanh profile is stable for Strouhal numbers $Sr_{\theta,max} = \frac{2\pi f\theta}{\Delta U} < 0.25$. Figure 4.16 shows the streamwise velocity profiles midway across the opening for both the upstream and downstream overhang case. Included in the figure are fitted tanh profiles. The fitting parameters θ_{fit}, U^-_{fit}/U_∞ and U^+_{fit}/U_∞ are depicted in the figure. Using the fitting parameters and $U_\infty = 25$ m/s and $f_{res} = 840$ Hz will give $Sr_{\theta,fit} = 0.20 < Sr_{\theta,max}$ for the resonating upstream overhang case and $Sr_{\theta,fit} = 0.27 > Sr_{\theta,max}$ for the non-resonating downstream overhang case, confirming the difference in resonance behavior between the two cases. Note that there is a 35% difference between the upstream and downstream overhang Strouhal numbers. Also the difference in modeled cavity driven flow $\Delta U^-_{fit}/U_\infty = 0.12$ is expected to stabilize the downstream shear layer even further [35, 36]. A more detailed analysis of the shear layer profiles is beyond the scope of the current work and planned for future investigations.

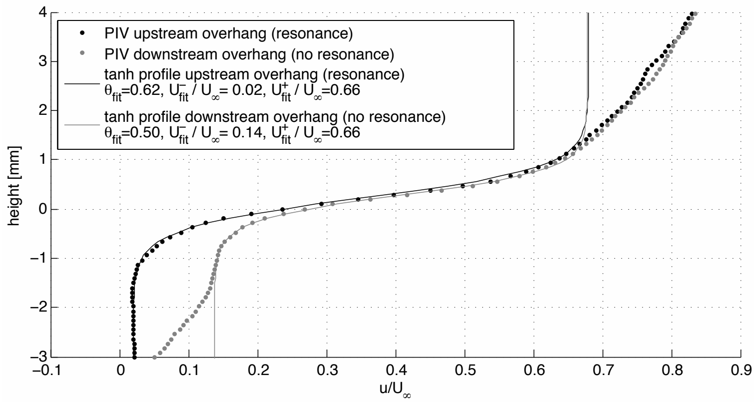

Figure 4.16: Mean shear layer velocity profiles over the cavity opening at $x/L_o = 0.5$. Included are tanh profiles with fitted parameters.

4.5.3 The role of edge rounding

As previously indicated, the resonance behavior is very sensitive to the edge geometry. Rounding of the downstream edge will reduce or even suppress the resonance behavior. This has already been indicated in literature, where vortex-edge interaction plays a critical role [20, 23]. PIV results are used to aid the physical interpretation of the mechanism.

Figure 4.17 shows streamlines of the time-averaged flow field in the opening and scaled vertical velocity fluctuation magnitude $\frac{|v'|}{|v'|_p}$. The fluctuation magnitude is scaled using the fluctuation magnitude in the shear layer at a point $|v'|_p$ located midway across the opening ($x/L_o = 0.5$, $y/L_o = 0.0$). In this way the fluctuation content can be compared independently of the amount of cavity feedback. The flow speed in this figure is 20 m/s and both cases have an upstream overhang lip with sharp upstream edges. Both cases do not have full resonance lock-on at these conditions.

The streamlines indicating a modified stagnation point location due to the downstream edge geometry. Also, the streamlined show a tendency of the flow to not get entrapped into the cavity, as the outside flow gets deflected outwards. This is confirmed by comparing $\frac{|v'|}{|v'|_p}$. Even through the shear layer fluctuation distribution is similar, more flow gets deflected into the cavity body.

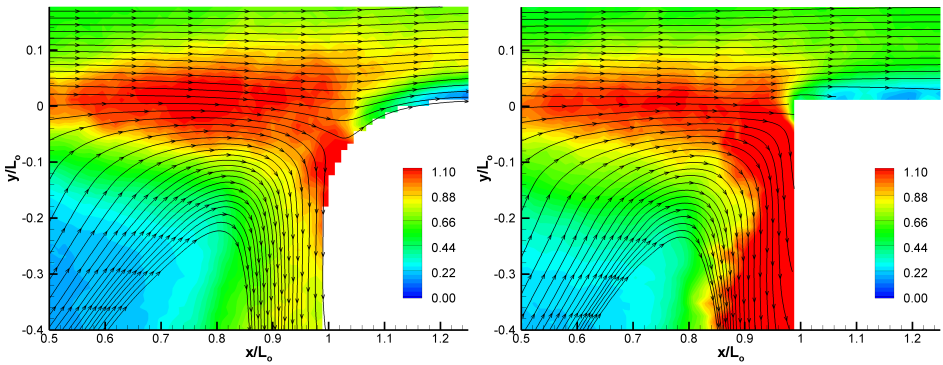

(a) Rounded downsteam edge (b) Sharp downsteam edge

Figure 4.17: Streamlines of mean flow with focus on the downstream edge, with scaled vertical velocity fluctuation magnitude in color $\frac{|v'|}{|v'|_p}$. The fluctuation magnitude is scaled using the fluctuation magnitude in the shear layer a point located midway across the opening $(x/L_o = 0.5, y/L_o = 0.0)$.

By comparing the maximum lock-on amplitudes in figure 4.9, one can see that rounding of the upstream edge leads to an increase in resonance lock-on amplitude. Figure 4.18 shows the mean flow streamline patterns in the opening for the configurations with an upstream cover lip overhang. Left subfigures show rounded upstream edges, right ones sharp upstream edges. Rounding of the upstream edge does not significantly change the mean flow pattern around the cavity opening.

An hypothesis for explaining the increased resonance amplitude in case of rounded upstream edges is that the free separation point of the rounded upstream edge compared to the fixed separation point of a sharp edge (due to Kutta condition) will decrease the stability of the shear layer. This is confirmed by examining vertical velocity fluctuation profiles scaled by maximum observed vertical velocity

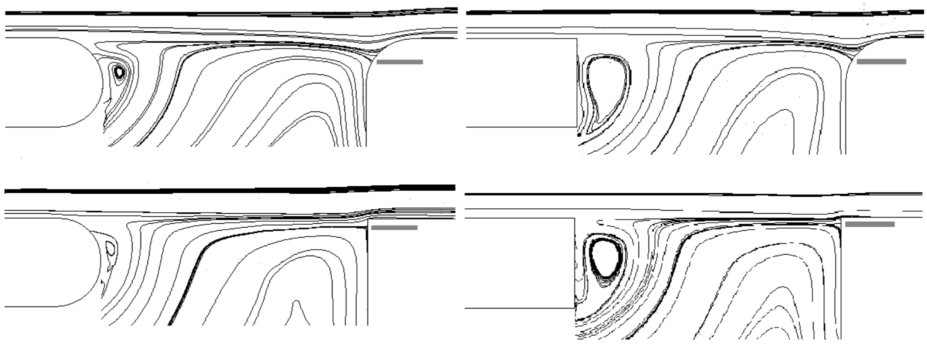

Figure 4.18: Streamlines of mean flow for all configurations with upstream cover lip overhang. Downstream mean flow stagnation point locations indicated by bars.

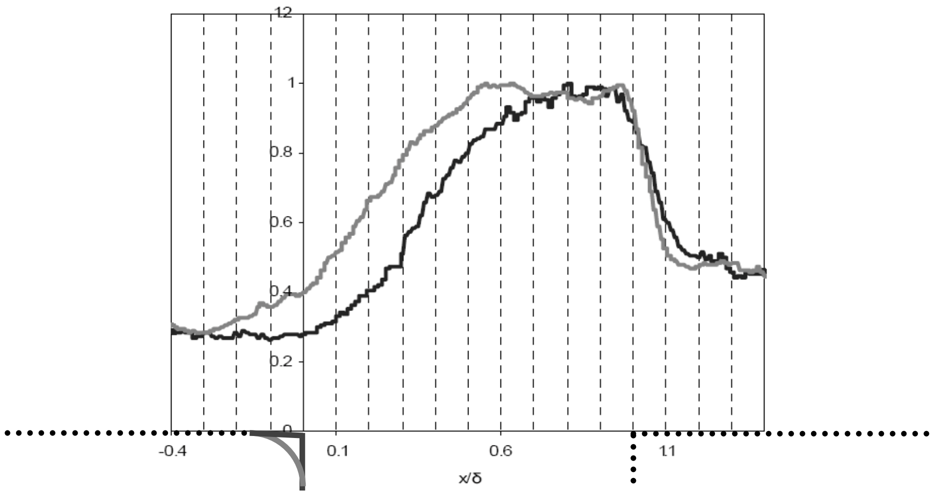

Figure 4.19: y-velocity rms profiles in a streamwise rake over the shear layer, 0.5 mm above the opening, scaled with maximum observed y-velocity fluctuation $\frac{|v'|}{|v'|_{max}}$. grey rounded upstream edge, black sharp upstream edge.

fluctuation $\frac{|v'|}{|v'|_{max}}$ of the shear layer in figure 4.19. The shear layer show larger fluctuations in the first section, even upstream of the rounded edge. Also the effective streamwise opening length is larger for the rounded edge, which promotes larger deflections at the downstream edge. In turn, this effect may cause a large amount of turbulent fluctuations to be entrained inside of the cavity.

4.6 Conclusions

An experimental investigation has been performed on simplified slender cavities that resemble automotive doors. A parametric study on the influence of the cavity opening geometry and boundary layer properties is conducted.

Several configurations showed resonance lock-on, where the acoustic velocity is about 1 percent of the free stream velocity. Higher modes with spanwise variations are observed, but only for some investigated geometries. The modes are described by a simple analytical model of coupled Helmholtz resonance with spanwise room modes.

The shear layer shows both flapping shear layer and vortex roll-up behavior. The shear layer growth is dominated by interaction with the turbulent boundary layer. Resonance behavior is highly sensitive to the boundary layer thickness. There is a cutoff ratio of boundary layer thickness compared to the opening length above which no resonance occurs.

Only geometries with an upstream cover lip overhang show resonance lock-on behavior. The difference in lock-on behavior between upstream and downstream edge overhangs can be explained by driven cavity internal flow patterns.

Rounding of the downstream edge reduces lock-on amplitude due to a reduction of flow entrapment into the cavity, thereby lowering feedback. Rounding of the upstream edge promotes resonance due to the increased mobility and instability of the shear layer, and an increased streamwise length to grow large deflections.

acknowledgements

We would like to thank Mico Hirschberg for his helpful advice. We also would like to thank Stefan Bernardy and Sina Ghaemi for help with the experimental setup.

Bibliography

[1] Rockwell, D. and Naudascher, E., "Self-sustained oscillations of impinging free shear layers," *Annual Review of Fluid Mechanics*, Vol. 11, 1979, pp. 67–94.

[2] Haigermoser, C., Scarano, F., and Onorato, M., "Investigation of the flow in a cirular cavity using stereo and tomographic particle image velocimetry," *Experiments in Fluids*, Vol. 46, 2009, pp. 517–526.

[3] Rossiter, J. E., *Wind-tunnel experiments on the flow over rectangular cavities at subsonic and transonic speeds*, London, H.M.S.O., 1st ed., 1967, pp. 1-32.

[4] Radavich, P. M., Selamet, A., and Novak, J. M., "A computational approach for flow-acoustic coupling in closed side branches," *Journal of the Acoustical Society of America*, Vol. 109, No. 4, 2001, pp. 1343–1353.

[5] Dequand, S., Hulshoff, S. J., and Hirschberg, A., "Self-sustained oscillations in a closed side branch system," *Journal of Sound and Vibration*, Vol. 265, 2003, pp. 359–386.

[6] Dequand, S., Luo, X., Willems, J., and Hirschberg, A., "Helmholtz-Like Resonator Self-Sustained Oscillations, Part 1: Acoustical Measurements and Analytical Models," *AIAA journal*, Vol. 41, No. 3, March 2003, pp. 408–415.

[7] Dequand, S., Hulshoff, S., Kuijk van, H., Willems, J., and Hirschberg, A., "Helmholtz-Like Resonator Self-Sustained Oscillations, Part 2: Detailed Flow Measurements and Numerical Simulations," *AIAA journal*, Vol. 41, No. 3, March 2003, pp. 416–424.

[8] Dequand, S., Willems, J. F. H., Leroux, M., Vullings, R., van Weert, M., Thieulot, C., and Hirschberg, A., "Simplified models of flue instruments: Influence of mouth geometry on the sound source," *Journal of the Acoustical Society of America*, Vol. 113, No. 3, March 2003, pp. 1724–1735.

[9] Coltman, J. W., "Jet Drive Mechanism in Edge Tones and Organ Pipes," *Journal of the Acoustical Society of America*, Vol. 60, No. 3, 1976, pp. 725–733.

[10] Elder, S. A., "On the Mechanism of Sound Production in Organ Pipes," *Journal of the Acoustical Society of America*, Vol. 54, 1973, pp. 1554–1564.

[11] Crouse, B., Senthooran, S., Balasubramanian, G., Freed, D., Noelting, S., Mongeau, L., and Hong, J. S., "Sunroof Buffeting of a Simplified Car Model: Simulations of the Acoustic and Flow-Induced Responses," *SAE Technical Paper*, 2005-01-2498, 2005, doi:10.4271/2005-01-2498.

[12] Ricot, D., Maillard, V., and Bailly, C., "Numerical Simulation of the Unsteady Flow past a Cavity and Application to Sunroof Buffeting," *7th AIAA/CEAS Aeroacoustics Conference*, Maastricht, The Netherlands, May 2001, pp. 1–11, AIAA-2001-2112.

[13] Ingard, U., "On the theory and design of acoustic resonators," *Journal of the Acoustical Society of America*, Vol. 25, No. 6, November 1953, pp. 1037–1061.

[14] Nelson, P. A., Halliwell, N. A., and Doak, P. E., "Fluid Dynamics of a Flow Excited Resonance, Part I: Experiment," *Journal of Sound and Vibration*, Vol. 78, No. 1, 1981, pp. 15–38.

[15] Nelson, P. A., Halliwell, N. A., and Doak, P. E., "Fluid Dynamics of a Flow Excited Resonance, Part II: Flow Acoustic Interaction," *Journal of Sound and Vibration*, Vol. 91, No. 3, 1983, pp. 375–402.

[16] Henderson, B. S., "Category 6 Automobile Noise Involving Feedback - Sound Generated by Low Speed Cavity Tones," NASA Techical Report, 2000, 95-100.

[17] Henderson, B. S., "Category 5: Sound Generation in Viscous Problems, Problem 2: Sound Generation by Flow over a Cavity," NASA Technical Report, 2004, 71-77.

[18] Mongeau, L., Bezemek, J. D., and Danforth, R., "Pressure Fluctuations in a Flow-Excited Door Gap Model," *SAE Technical Paper*, 971923, 1997, doi:10.4271/971923.

[19] Ahuja, K. and Mendoza, J., "Effects of cavity dimensions, boundary layer, and temperature on cavity noise with emphasis on benchmark data to validate computational aeroacoustic codes," *NASA contractor report*, , No. NASA/CR4653, 1995.

[20] Kooijman, G., Hirschberg, A., and Golliard, J., "Acoustical response of orifices under grazing flow: Effect of boundary layer profile and geometry," *Journal of Sound and Vibration*, Vol. 315, 2008, pp. 849–874.

[21] Howe, M. S., "Low Strouhal number instabilities of flow over apertures and wall cavities," *Journal of the Acoustical Society of America*, Vol. 102, No. 2, 1997, pp. 772–780.

[22] Gloerfelt, X., "Cavity noise," `http://sin-web.paris.ensam.fr/squelettes/ref_biblio/Gloerfelt_VKI_2009a.pdf` (date last viewed 04/25/12), 2009.

[23] Rockwell, D. and Knisely, C., "The organized nature of flow impingement upon a corner," *Journal of Fluid Mechanics*, Vol. 93, No. 3, 1979, pp. 413–432.

[24] Gharib, M. and Roshko, A., "The effect of flow oscillations on cavity drag," *Journal of Fluid Mechanics*, Vol. 177, 1987, pp. 501–530.

[25] Morris, S., "Shear Layer Instabilities: Particle Image Velocimetry Measurements and Implications for Acoustics," *Annual Review of Fluid Mechanics*, Vol. 43, 2011, pp. 529–550.

[26] Elder, S. A., Farabee, T. M., and DeMetz, F. C., "Mechanisms of Flow-excited Cavity Tones at Low Mach Number," *Journal of the Acoustical Society of America*, Vol. 72, No. 2, 1982, pp. 532–549.

[27] de Jong, A. T. and Bijl, H., "Investigation of higher spanwise Helmholtz resonance modes in slender covered cavities," *Journal of the Acoustical Society of America*, Vol. 128, No. 4, 2010, pp. 1668–1678.

[28] Michalke, A., "On spatially growing disturbances in an inviscid shear layer," *Journal of Fluid Mechanics*, Vol. 23, No. 3, 1965, pp. 521–544.

[29] Michalke, A., "The influence of the vorticity distribution on the inviscid instability of a free shear layer," *Fluid Dynamics Transactions*, Vol. 4, 1969, pp. 751–770.

[30] Michalke, A., “The instability of free shear layers, a survey on the state of art,” *Deutsche Luft- und Raumfart Mittelung*, Vol. 70, No. 4, 1970.

[31] Bruggeman, J., Hirschberg, A., Dongen, M. V., Wijnands, A., and Gorter, J., “Self-sustained aero-acoustic pulsations in gas transport systems: experimental study of the influence of closed side branches,” *Journal of Sound and Vibration*, Vol. 150, No. 3, 1991, pp. 371–393.

[32] White, F. M., *Viscous Fluid Flow*, McGraw-Hill, New York, 2nd ed., 1991, pp. 409, 413.

[33] Ma, R., Slaboch, P., and Morris, S., “Fluid mechanics of the flow-excited Helmholtz resonator,” *Journal of Fluid Mechanics*, Vol. 623, March 2009, pp. 1–26.

[34] Sarohia, V., “Experimental Investigation of Oscillations in Flows Over Shallow Cavities,” *AIAA journal*, Vol. 15, No. 7, 1977, pp. 984–998.

[35] Howe, M. S., “Influence of wall thickness on Rayleigh conductivity and flow-induced aperture tones,” *Journal of Fluids and Structures*, Vol. 11, Jan 1997, pp. 351366.

[36] Howe, M. S., “Rayleigh Conductivity and Self-Sustained Oscillations,” *Theoretical and Computational Fluid Dynamics*, Vol. 10, No. 1-4, Jan 1998, pp. 187–200.

Chapter 5

Edge type plasma actuators for cavity flow induced noise control

This chapter is based on the submitted journal paper:

Edge type plasma actuators for cavity flow induced noise control
A.T. de Jong and H. Bijl
AIAA Journal

(Submitted 26 December 2011, pending response)

A novel dielectric barrier discharge plasma actuator configuration for flow control is employed on open cavities to evaluate the potential for aeroacoustic tonal noise reduction. Instead of a planar configuration, the actuator is designed around the cavity opening edges. The investigation focusses on the effectiveness for tonal noise suppression and the associated fluid dynamics. The investigated cavities have a square cross-section. A low Mach flow with a thin laminar boundary layer introduces tonal sound emission due to hydrodynamic feedback. Both upstream and downstream edge actuators have been tested, and both cavity inwards and outwards actuation has been employed. The upstream mounted actuators influence cavity tonal feedback. A cavity inwards velocity inducing actuator completely suppresses the cavity tone up to a free-stream velocity of 12.5 m/s. An outwards inducing actuator influences mode switching. Downstream mounted actuators do not influence the cavity aeroacoustics. Particle image velocimetry (PIV) is used to investigate the fluid dynamics. The actuator can induce velocities up to 4 m/s

for an applied voltage of 15 kV at 4 kHz. The induced velocity is directed perpendicular to the free stream direction. A secondary circulating flow is developed in the cavity that modifies the hydrodynamic feedback mechanism.

5.1 Introduction

The current investigation concerns the reduction of cavity aeroacoustic feedback using active flow control by discharge plasma actuators. The aeroacoustic tonal feedback of a shear layer over a cavity opening can pose problematically high pressure oscillations and unwanted noise in for example aircraft landing gear and weapon bays. Therefore cavities have been intensively investigated before in literature to understand and control tonal feedback [1]. Active flow control has been of interest in aerospace for a large number of years. Active flow control can be employed for drag reduction, lift enhancement, but also for control of aeroacoustic noise and vibrations.

Out of various flow control actuator designs, there has been an increasing interest in the dielectric barrier discharge (DBD) flow actuator in the past 10 years. Its working principle is purely electric, with no moving parts or holes needed [2]. A typical DBD actuator consists of two electrodes where one is exposed to the air and one is covered under a dielectric. A weakly ionized glow discharge plasma is generated by applying an alternating current at high voltage. The asymmetry in plasma development during the AC cycle results in a body force along the surface in a region close to the surface [3]. Due to the actuation close to the surface, a plasma actuator is a good candidate for use in active flow control. One of the earliest demonstrations of aerodynamic flow control using a DBD plasma actuator was done by Roth et. al. [4], where a low speed boundary layer flow was modified using plasma actuators. Another example of flow control using plasma actuators was given by Thomas et. al. [5], where the vortex shedding from a cylinder was suppressed. Both Moreau [6] and Corke et. al. [2] provide an overview of the use of plasma actuators.

The interest of the current work is aeroacoustic flow control of open cavities. Numerous active flow control designs have been tested on cavity geometries in literature, an overview of these flow control methods for cavities is provided by Cattafesta [7]. Due to their simplicity (no holes, no moving parts), DBD plasma actuators are a good candidate for use in cavity flow control. Plasma actuators have been investigated for use in aeroacoustic cavity flow control before by Huang et.al. and Chan et.al. [8, 9, 10]. They demonstrated the effect of spanwise and streamwise oriented actuators located upstream of an open cavity geometry that exhibits tonal noise. They concluded that the spanwise oriented actuator had limited influence on the flow field, whereas a streamwise oriented actuator configuration introduced three dimensional flow variations upstream of the cavity, effecting the spanwise coherence of the cavity shear layer.

In previous investigations by the authors [11, 12, 13], the onset of tonal feedback was found to be sensitive to the geometry of cavity opening edges. Therefore in the current investigation, a new DBD plasma actuator configuration is employed on open cavities to evaluate the potential for noise reduction. The actuator design is related to the spanwise oriented actuator of Huang. Instead of a planar configuration, a new corner type actuator configuration is designed around the cavity opening edges where the electrodes are in different planes. This enables direct actuation on the developing shear layer over the cavity opening. Also the body force can now be applied perpendicular to the free stream flow direction. A similar design has been employed by Nati et. al. [14] for blunt trailing edge flow control, but never for aeroacoustic applications like suppression of cavity tonal resonance.

The current work investigates an edge type plasma actuator in aeroacoustic cavity noise control. The key questions are whether or not this type of actuator has the potential to suppress cavity tonal noise, and which fluid dynamics phenomena play a role. In order to investigate this, both upstream and downstream actuator locations have been tested, where the body force can be directed either into or away from the cavity. In this first study on the geometry, the actuators are operated in a continuous mode, without any pulsation or active feedback control. We experimentally investigate the cavity sound pressure level (SPL) reduction and the details of the flow field using high speed particle image velocimetry (PIV).

The experimental setup is described in section 5.2. A parametric analysis of the actuator influence is presented in section 5.4. In sections 5.5.2 and 5.5.1 PIV based flow field analysis is performed on actuator induced flow field in a quiescent fluid and on the effect of the actuator and cavity in presence of mean flow.

5.2 Experimental setup

A cavity with a square cross section is subjected to a low Mach number grazing flow with a laminar boundary layer in an open jet windtunnel. Four DBD actuator designs are tested around the cavity opening edges. The cavity sound pressure levels are recorded using internal microphones. Moreover, planar high speed PIV is employed to investigate the flow field.

5.2.1 Windtunnel and model

Experiments are conducted in a low-speed open jet wind tunnel at Delft University of Technology. The tunnel has a vertical outflow through a circular opening, 0.6 m in diameter. The tunnel contraction ratio is 250:1. The airflow in the test section has a turbulence intensity of 0.2 % and the wind tunnel acoustic background noise at 25 m/s is 20 dB. The cavity is evaluated for velocities from 5 to 20 m/s with 0.5 to 1 m/s increments.

The experimental geometry consists of an open cavity with length L over depth D ratio of 1. The model is displayed in figure 5.1. The dimensions are $L = D = 44$ mm, with a width $W = 220$ mm or $W = 5L$. The cavity is mounted in a 600 mm wide and 60 mm thick splitter plate with an elliptic nose cone. The cavity is mounted 200 mm from the splitter plate nose to ensure a thin laminar boundary

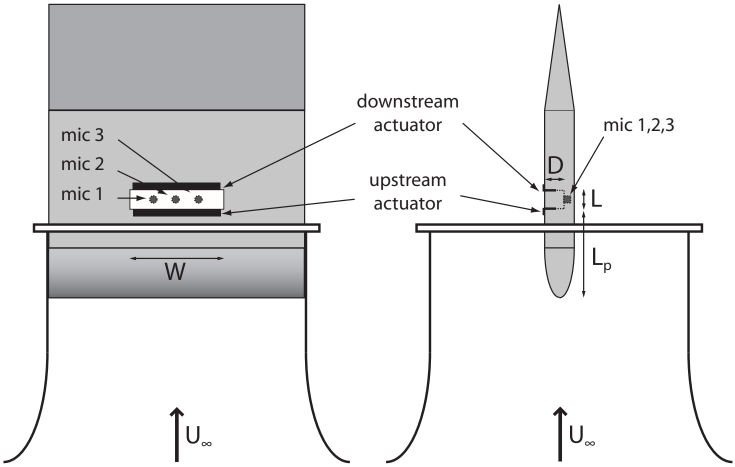

Figure 5.1: Model in windtunnel, the upstream and downstream actuators are indicated in red.

layer over the cavity opening.

5.2.2 Actuator design

The plasma actuator is a novel corner type design based on a modified planar single dielectric barrier discharge (SDBD) type actuator. Figure 5.2 shows the configuration. The actuators consist of a covered and an exposed electrode made of copper tape and a dielectrium of Kapton tape. The Kapton dielectricum is 127 μm thick. The plasma is created by applying a sinusoidal alternating voltage of 15 kVolts at 4 kHz. Similar to a classic planar configuration, the asymmetry in plasma during a voltage cycle causes a net induced momentum as a body force to the fluid near the actuator [2]. The net induced velocity is directed from the exposed electrode towards the covered electrode. The applied voltage and frequency are chosen based on results for planar type actuators [3]. The configurations of figure 5.2 can be applied to both the upstream and downstream corner of the investigated open cavity.

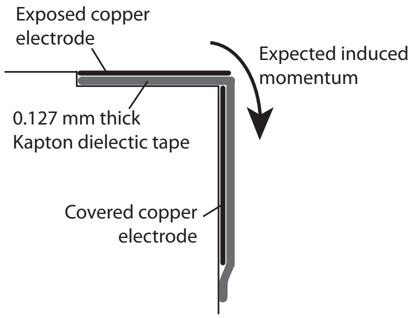

Figure 5.2: Corner type SDBD actuator design. Please note that electrode and Kapton thicknesses are not to scale.

Compared to previously investigated planar upstream spanwise actuators that only induce streamwise momentum [10, 3] , the corner type actuators are able to induce momentum perpendicular to the cavity shear layer and in the direction of the shear layer instabilities [14]. This gives the corner type actuators the potential to directly influence the linear stability properties of the cavity shear layer in case of upstream mounted actuators. Downstream mounted actuators can potentially modify the vortex impingement of the destabilized shear layer onto the downstream edge and thus modify the hydrodynamic feedback.

In the present investigation, the driving voltage is continuously supplied, no active control using feedback or feed-forward is present. The focus is to investigate the fluid dynamic potential of the actuators to modify the aeroacoustic behavior. When the actuators prove effective in passive actuation mode, future investigations will be planned on the application of active control of feedback or feed-forward [15].

5.2.3 Measurements

The cavity internal pressure is measured using 3 Sonion 8000 Series microphones flush mounted on the cavity floor. The location of the 3 microphones is indicated in figure 5.1. The microphones have been calibrated using a piston-phone. The measurements consist of 10 sec time samplings at 10000 Hz. For each setup and each velocity increment, signals are acquired without and with plasma actuation sequentially to ensure a high quality comparison. Because the focus of the current investigation is the difference in tonal excitation and not the absolute sound pressure level in the far field, only in cavity microphones and no far field microphones are used.

In order to evaluate the flow in the opening region, two-component, high-speed, time-resolved particle image velocimetry (PIV) has been used. The PIV measurements are also used to capture the laminar boundary layer characteristics.

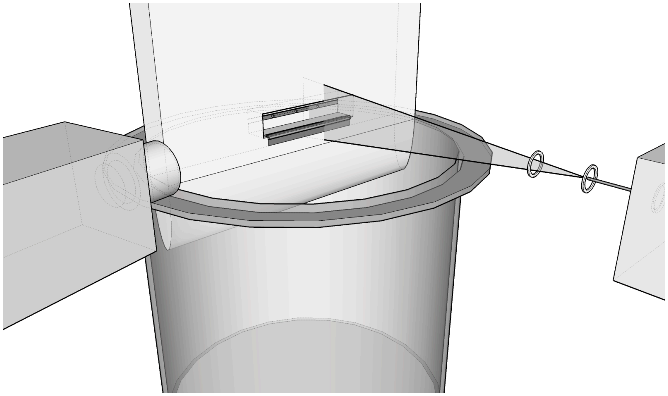

Figure 5.3: PIV setup in wind tunnel. High speed camera depicted to the left and laser to the right.

The setup is depicted in figure 5.3. Illumination over an area of 70 by 70 mm is provided by a Quantronics Darwin-Duo 527 Nd:YLF laser. The field of view captures the cavity and the outer flow boundary layer. The light sheet is positioned streamwise and perpendicular to the plate with spanwise location 80 mm from the cavity in spanwise direction. A Photron Fastcam SA1.1 camera is placed at an a 80 degree angle with the illumination and captures 1,024x1,024 images. The images are calibrated to compensate for the small off-perpendicular camera angle. The illumination and recording devices are synchronized and controlled by a LaVision programmable timing unit (PTU v9) controlled by DaVis 8.0 software. Each measurement consists of 1,000 image pairs at a recording frequency of 6,000 Hz, which is sufficient to cover the dynamics of the shear layer over the opening.

5.3 Experimental results of cavity aeroacoustics without plasma actuation

The boundary layer velocity profile obtained from PIV at the upstream corner of the cavity is depicted in figure 5.4. The boundary layer is resembling a laminar flat plate boundary layer [16]. To indicate this, the Blasius flat plate boundary layer solution is added to the figure.

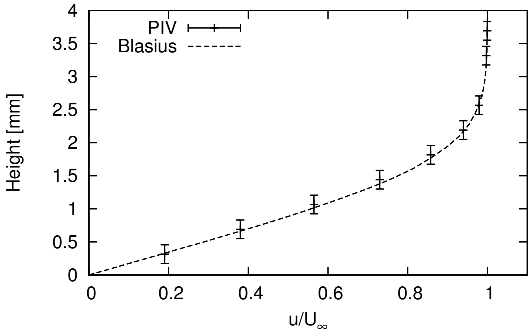

Figure 5.4: Boundary layer profile measured at the upstream corner of the cavity for 10 m/s mean flow

At 10 m/s flow speed, the parameters of the boundary layer are: displacement thickness $\delta^* = 1.0$ mm, momentum thickness $\theta = 0.4$ mm and height at 99 % of the freestream velocity $\delta_{99} = 2.9$ mm [16]. Using the profile of Blasius' theory this gives a boundary layer thickness of $\delta = 3.4$ mm. The boundary layer thickness is small compared to the cavity streamwise opening length, $(L/\delta)_{10m/s} \approx 13$.

Figure 5.5 shows the spectrogram of the cavity center floor microphone. The frequency is depicted on the horizontal axis, the velocity on the vertical one, and the amplitude in dB in color. Please note that for visualization purposes, the frequencies have been summed into bands of 10 Hz.

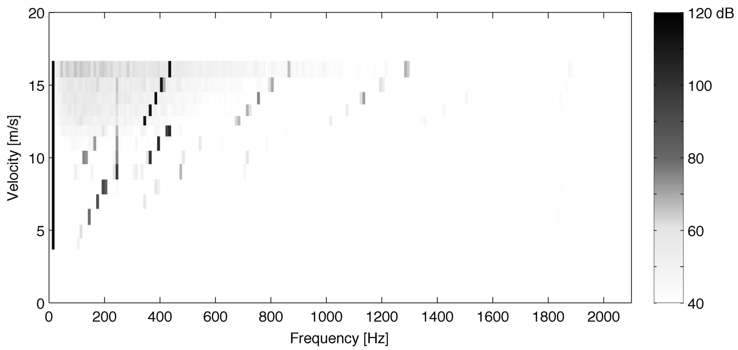

Figure 5.5: Spectrogram of cavity without actuation

Tonal modes start around 4 m/s, below that the shear layer is stable and no feedback lock-on occurs []. Hankey and Shang [17] deduced using linear stability theory that a minimum ratio of cavity streamwise length over boundary layer thickness $\frac{L}{\delta} > 2\pi$ is needed to destabilize the shear layer. Sarohia [18] found using experiments that cavity oscillations would occur if $\frac{L}{\delta}\sqrt{Re_\delta} > 290$. Around resonance onset, the currently measured ratios are $\left(\frac{L}{\delta}\right) = 8.1$ and $\frac{L}{\delta}\sqrt{Re_\delta} = 310$, which is in agreement with literature.

Most of the cavity tonal excitations show a linear relation between frequency and velocity, indicating Rossiter modes [19] . For low Mach nr flows, Rossiter modes are indicated by excitations at fixed Strouhal numbers $Sr = \frac{fL}{U_\infty}$. In the spectrogram, two modes are visible, at $Sr = 1.35$ and $Sr = 1.68$ (deduced from the peak amplitudes in figure 5.5). These correspond to the second and third Rossiter mode, with 2 and 3 (partial) vortices present in the opening respectively. This is confirmed by PIV time snapshot images of figure 5.14 and correlation phase of figure 5.15, where the third Rossiter mode is visible. With increasing velocity, the cavity switches between the above described modes. The results are in accordance with literature on open cavities [20]. In the higher velocity regime above 15 m/s, harmonics of the modes are clearly visible.

Next to the Rossiter modes, a weaker excitation at fixed frequency is visible around 240 Hz for flow speeds from 8 to 15 m/s. The frequency is independent of flow velocity, indicating that this originates from a resonance. Possible mechanisms can be coupling with tunnel modes in the tunnel opening section. As this mode is weaker than the hydrodynamic modes present in the cavity, it is not investigated in further detail.

5.4 Analysis of four plasma actuation configurations

Four actuator configurations have been investigated by using both upstream (U) and downstream (D) actuators and by applying both inwards induced velocity (I) and outwards induced velocity (O) actuation. This results in the following combinations: UI, UO, DI, DO, as depicted in 5.6.

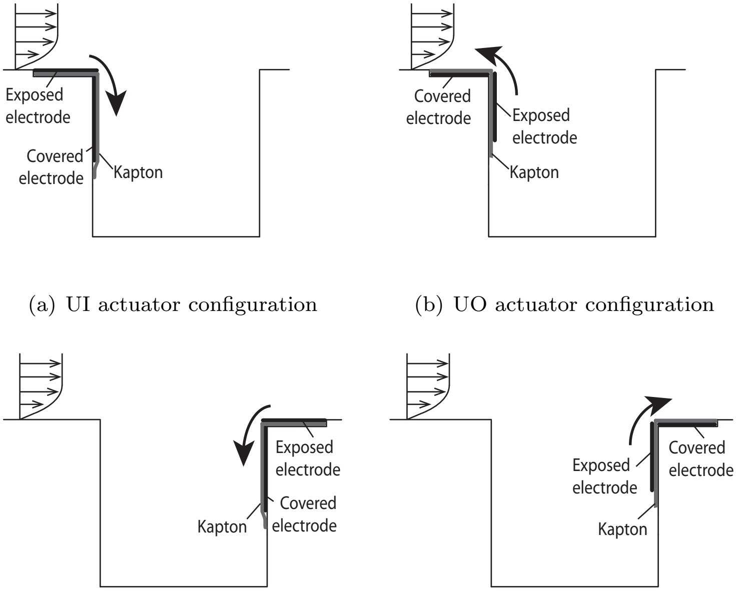

(a) UI actuator configuration (b) UO actuator configuration

(c) DI actuator configuration (d) DO actuator configuration

Figure 5.6: Overview of tested actuator configurations, please note that actuator thicknesses are not to scale

The microphone time series are converted to spectra with 1 Hz bandwidth for each velocity increment and combined into spectrograms, as displayed in figures 5.7 and 5.8. Please note that for visualization purposes, the frequencies have again been summed into bands of 10 Hz. When the actuators are active, a 2 kHz subharmonic of the 4 kHz actuator frequency is visible on the right side in the figures. In the spectrogram for the UI actuator of figure 5.7, one can see that the plasma actuator completely suppresses the tonal cavity noise otherwise present up to a velocity of 12.5 m/s. The result for the UI configuration is interesting, as one would initially expect an opposite behavior. Hydrodynamic feedback is enabled due to vortex impingement at the downstream cavity corner [20]. In case of inward actuation one would expect an increased impingement of the shear layer and thus an increased feedback tone. However the opposite is measured. This is further investigated in section 5.5. In case of an outward induced UO actuation (figure 5.8) tonal feedback is promoted for the second Rossiter mode around 10 m/s, where otherwise two weaker tones of different modes would be present. The actuator thus has an influence on mode selection.

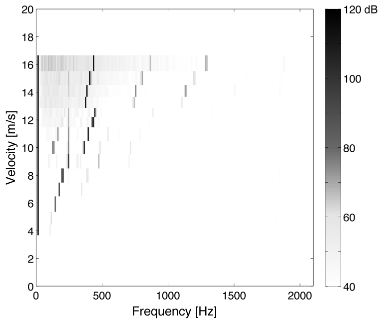

(a) without plasma actuation

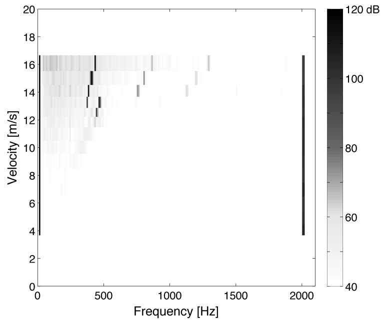

(b) with plasma actuation

Figure 5.7: Spectrograms for UI actuator

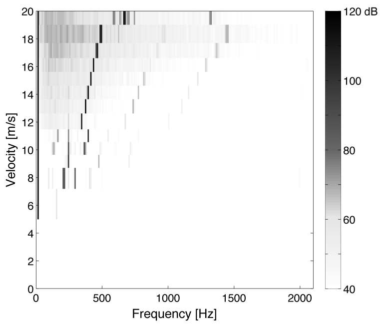

(a) without plasma actuation

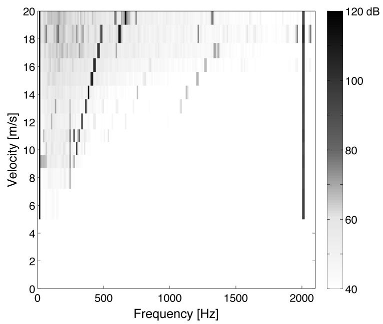

(b) with plasma actuation

Figure 5.8: Spectrograms for UO actuator

Example spectra at 11, 12, 12.5 and 13 m/s are depicted in figure 5.9, where the inward velocity inducing (UI) actuators are compared to the case without actuation. The reduction is around 50 dB at 11 m/s, around 40 dB at 12 m/s and around 10 dB at 12.5 m/s. The 2 kHz subharmonic of the driving voltage frequency is visible on the right of the figure. At 11 and 12 m/s, weaker tonal peaks are also diminished by actuation. At 13 m/s one can clearly identify the higher harmonics of the dominant tone for both the case with actuation off and on.

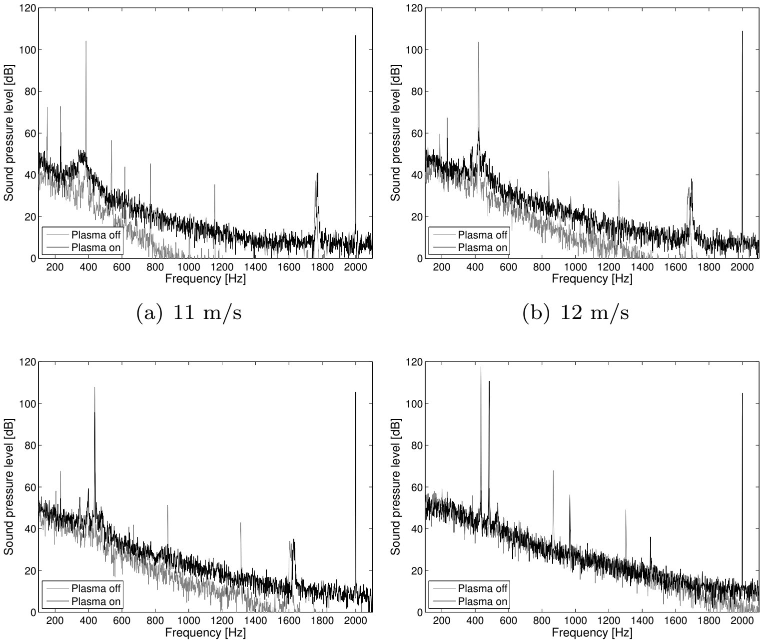

(a) 11 m/s (b) 12 m/s

(c) 12.5 m/s (d) 13 m/s

Figure 5.9: spectrum at 11, 12, 12.5 and 13 m/s for UI actuator

No results are depicted for the downstream positioned actuators, as the actuators did not have any measurable effect on the lock-on tone. At the downstream edge, the shear layer has already destabilized and formed distinct vortices (as will be shown in section 5.5.2). The currently used downstream actuators are not strong enough to modify the fluid dynamics of flow impingement to an extent that would modify the cavity aeroacoustics.

5.5 Flow field analysis of the most influential plasma actuation configuration

The upstream mounted, inward velocity inducing (UI, see figure 5.6(a)) plasma actuator has the largest effect on cavity flow dynamic tonal lock-on. Up till 12.5 m/s, cavity tonal lock-on is suppressed due to the actuator. In case of inward actuation one would at first glance expect an increased impingement of the shear layer on the downstream edge and thus an increased feedback. However the opposite is measured. In this section the fluid dynamics of this lock-on suppression and the discrepancy between expectation and observation is further investigated. A reduction in tonal feedback noise can have several possible causes:

- shear layer deflection away from downstream cavity edge, thus reducing the downstream vortex impingement
- blocking or deflection of feedback signal inside the cavity
- destabilization of shear layer prior to arrival of feedback signal, reducing the correlation between feedback signal and vortex formation
- Disruption of the spanwise coherence of the shear layer

The above mentioned causes will be evaluated in this discussion of the current section. PIV results will be used to aid the analysis.

5.5.1 Analysis of inwards inducing actuator in quiescent fluid

The flow field included by the upstream mounted inwards inducing actuator in case of absence of mean flow is depicted in figure 5.10. The induced velocity is mostly unidirectionally inwards, with some induced flow around the upstream edge. The maximum measured induced velocity is 4.1 m/s. The induced velocity field on the cavity inner wall corresponds closely to that of a planar type actuator [3]. Due to the design, the maximum velocity can occur close to the cavity outer edge. The induced velocity is comparable to measurements on planar actuators by Kotsonis et. al. [3]. The corner type actuator maximum induced velocity is slightly lower, which can be attributed to the nearby presence of the sharp edge.

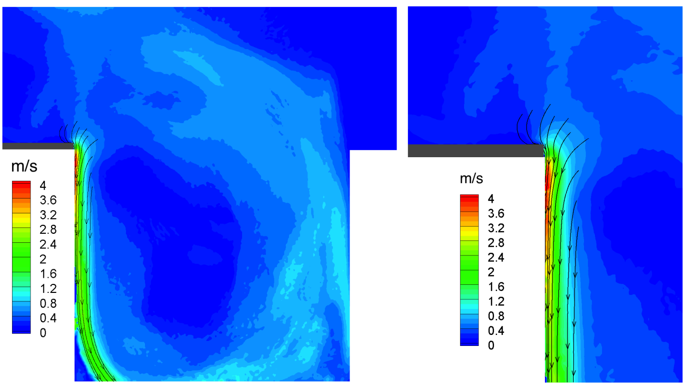

(a) Cavity overview (b) zoomed in view

Figure 5.10: Flow field induced by upstream mounted inwards inducing (UI) actuator, colored by velocity magnitude in m/s. Grey areas are blanked out due to reflections in PIV.

5.5.2 Analysis of cavity tonal noise reduction

The mean driven flow inside the cavity for both with or without plasma actuation is given in figure 5.11. A secondary region of circulating flow is present near the upstream cavity edge due to the plasma actuation. This modifies the fluid dynamics of the feedback needed to obtain a lock-on tone.

Figure 5.12 provides a zoomed in view of the circulating flow around the upstream edge. The fluid dynamics around the upstream edge are modified, which has an effect on the shear layer properties. The flow from the cavity is deflected and reaches the shear layer at a more downstream location. The stronger secondary vortex that is present in the case of actuation can cause an additional shear on the initial part of the shear layer, thereby making it more unstable.

Figure 5.13 shows the mean shear layer profiles over the opening for both with and without actuation. The mean shear layer thickness close to the downstream edge is increased towards the cavity, causing higher driven flow velocities inside the cavity. The shear layer is thus not only thickened, but also displaced inwards. This is in accordance with expectations, as the actuator produces cavity inward momentum. The increased impingement on the downstream corner due to the displacement causes an increased cavity driven flow, as was seen in figure 5.11. The observed reduction in feedback can not be explained by a deflection of the shear layer away from the downstream edge, because it is clear in figure 5.13 that the opposite is achieved with the UI actuator configuration.

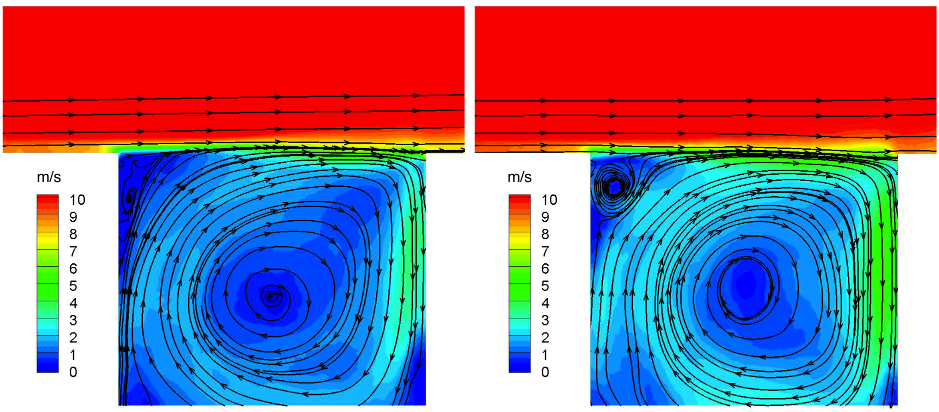

(a) without plasma actuation (b) with plasma actuation

Figure 5.11: Mean driven flow inside cavity with upstream mounted inwards inducing plasma actuator for $U_\infty = 10$ m/s, colored by velocity maginitude in m/s

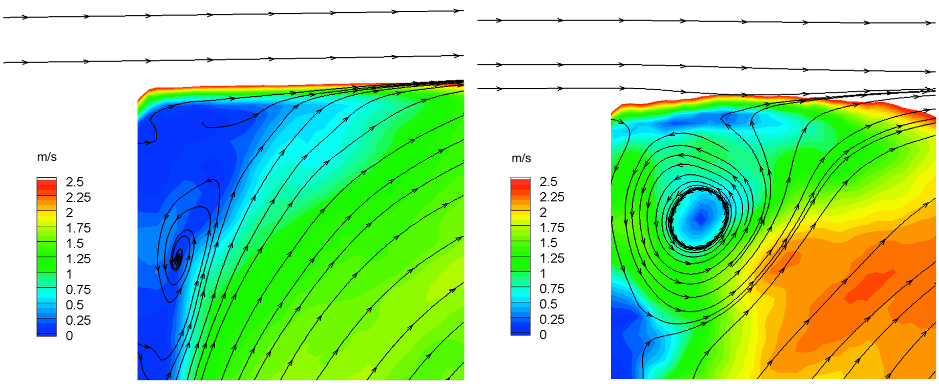

(a) without plasma actuation (b) with plasma actuation

Figure 5.12: Mean driven flow inside cavity with upstream mounted inwards inducing plasma actuator for $U_\infty = 10$ m/s, colored by velocity maginitude in m/s. Zoom around upstream region.

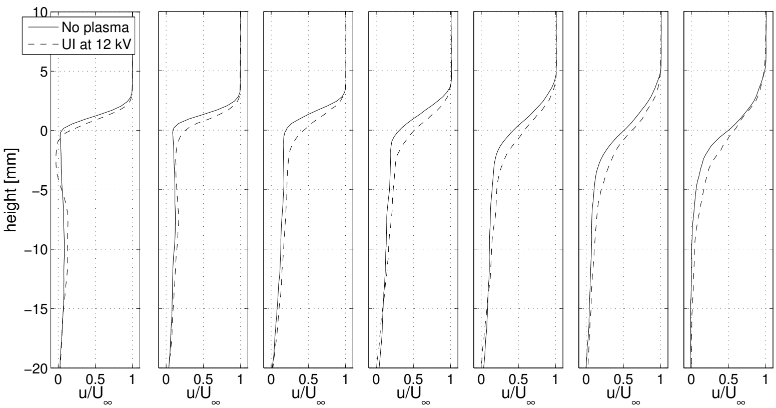

(a) $\frac{x}{L} = \frac{1}{8}$ (b) $\frac{x}{L} = \frac{2}{8}$ (c) $\frac{x}{L} = \frac{3}{8}$ (d) $\frac{x}{L} = \frac{4}{8}$ (e) $\frac{x}{L} = \frac{5}{8}$ (f) $\frac{x}{L} = \frac{6}{8}$ (g) $\frac{x}{L} = \frac{7}{8}$

Figure 5.13: Mean shear layer profiles over cavity opening, $U_\infty = 10$ m/s.

Figure 5.14 shows several time snapshots of vorticity in the shear layer. The flow impingement on the downstream edge is visible in the figures for both with and without actuation. However, the shear layer instabilities are not fully correlated with vortex impingement on the trailing edge in case of actuation (also visible in figure 5.15), indicating a reduction in the hydrodynamic feedback mechanism. The shear layer appears more unstable, which can be due to the increased shear around the upstream edge due to the observed secondary vortex. Deviations in actuation strength along the span can also cause a reduction in spanwise coherence. This last possibility cannot be tested however by the current PIV analysis at a single spanwise location.

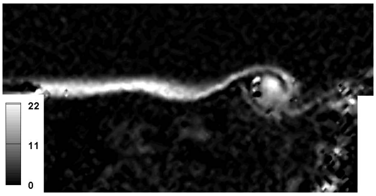

(a) without plasma actuation, t/T=0.0

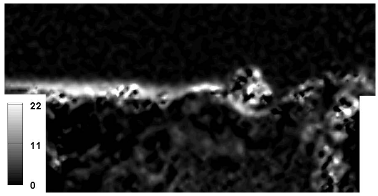

(b) with plasma actuation, t/T=0.0

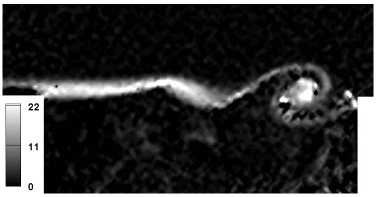

(c) without plasma actuation, t/T=0.25

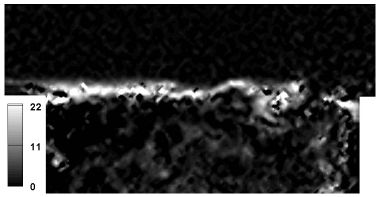

(d) with plasma actuation, t/T=0.25

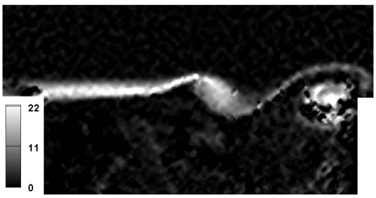

(e) without plasma actuation, t/T=0.5

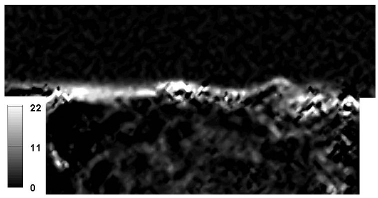

(f) with plasma actuation, t/T=0.5

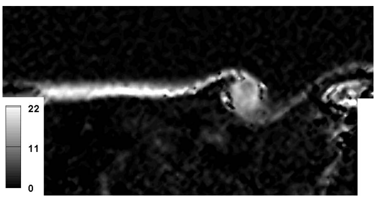

(g) without plasma actuation, t/T=0.75

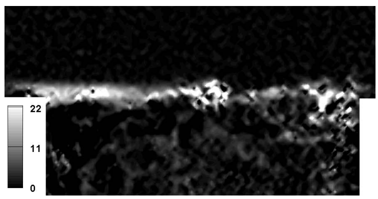

(h) with plasma actuation, t/T=0.75

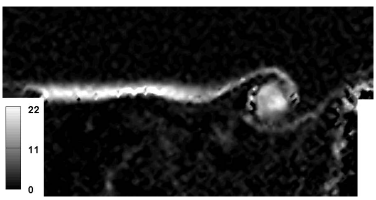

(i) without plasma actuation, t/T=1.0

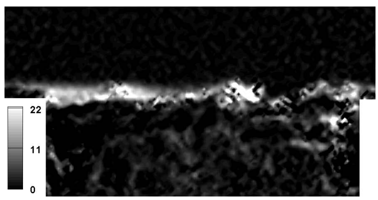

(j) with plasma actuation, t/T=1.0

Figure 5.14: Time snapshots of spanwise vorticity scaled by free stream velocity ω_z/U_∞ (in $1/s$) in shear layer during a single feedback cycle, $U_\infty = 10$ m/s

The reduced feedback can also be seen in figure 5.15, where the y-component of velocity across the shear layer is correlated to the tonal microphone pressure signal of the cavity without actuation. The correlation is normalized and the maximum amplitude with corresponding normalized phase are depicted. In case of UI actuation, the correlation is reduced compared to the situation without plasma actuation. The phase diagram confirms the appearance of the third Rossiter mode at $U_\infty = 10$ m/s. The gradient of the phase over x/L is lower in case of UI actuation in the second half of the opening, indicating an increased vortex convection velocity. This can be attributed to the increased driven flow inside the cavity (as observed before in figure 5.13) as a consequence of the inward induced momentum of the actuator. The correlation phase differs between the two cases, the mean vortex convection velocity in the second half of the opening as derived from the phase graph is $U_\omega = 0.58U_\infty$ and $U_\omega = 0.55U_\infty$ with and without actuation respectively.

5.6 Conclusions

The effect of novel corner type SDBD actuator configurations on the aeroacoustic lock-on behavior of open cavities has been tested. Only upstream mounted actuators were shown to have an effect on the cavity aeroacoustics. In the case of an inwards velocity inducing actuator, lock-on was suppressed for all velocities below 12.5 m/s. The outward velocity inducing actuator had an influence on the mode selection at certain flow speeds.

The inwards velocity inducing actuator has been investigated experimentally using high speed planar PIV. The cavity induced flow field in the absence of mean flow closely resembles that of planar actuator configurations in literature. During actuation, a secondary circulating flow region is created in the vicinity of the plasma actuator. This modifies the driven flow inside the cavity and the

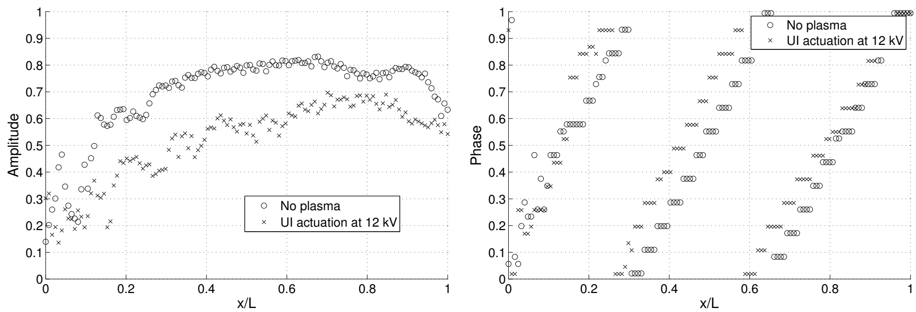

(a) Correlation maximum amplitude (b) Correlation phase at maximum amplitude

Figure 5.15: Normalized maximum correlation coefficient of vertical velocity U_y in shear layer across the opening as obtained by PIV at $U_\infty = 10$ m/s , with microphone pressure for the no plasma case as reference signal.

hydrodynamic feedback causing aeroacoustic lock-on. The current results with actuators continuously actuated show the potential for active flow control using feedback and/or periodic actuation to reduce cavity induced noise.

Acknowledgments

The authors would like to thank Marios Kotsonis for his help and expertise on plasma actuators, Sina Ghaemi for helping with the PIV setup, Prof. Pierro Cologne for being so kind to provide laser equipment, Valentina Koschatzky for her help with the initial experimental design, Prof. Fulvio Scarano for his experimental expertise and for providing the remaining PIV equipment, and Stefan Bernardy for his help with the final experimental setup.

Bibliography

[1] Gloerfelt, X., "Cavity noise," `http://sin-web.paris.ensam.fr/squelettes/ref_biblio/Gloerfelt_VKI_2009a.pdf` (date last viewed 04/25/12), 2009.

[2] Corke, T. C., Enloe, C. L., and Wilkinson, S. P., "Dielectric Barrier Discharge Plasma Actuators for Flow Control*," *Annual Review of Fluid Mechanics*, Vol. 42, No. 1, Jan 2010, pp. 505–529.

[3] Kotsonis, M., Ghaemi, S., Veldhuis, L., and Scarano, F., "Measurement of the body force field of plasma actuators," *Journal of Physics D: Applied Physics*, Vol. 44, 2011, pp. 045204 (11pp).

[4] Roth, J. R., Sherman, D. M., and Wilkinson, S. P., "Electrohydrodynamic flow control with a glow-discharge surface plasma," *AIAA journal*, Vol. 38, 2000, pp. 1166–1172.

[5] Thomas, F., Kozlov, A., and Corke, T., "Plasma actuators for bluff body flow control," *AIAA journal*, Vol. 46, 2008, pp. 1921–1931.

[6] Moreau, E., "Airflow control by non-thermal plasma actuators," *Journal of Physics D: Applied Physics*, Dec 2007.

[7] Cattafesta III, L., Song, Q., Williams, D., Rowley, C., and Farrukh, S., "Active control of flow-induced cavity oscillations," *Progress in Aerospace Sciences*, Vol. 44, Dec 2008, pp. 479–502.

[8] Huang, X., Chan, S., and Zhang, X., "Atmospheric plasma actuators for aeroacoustic applications," *IEEE Transactions in Plasma Sciences*, Vol. 35, No. 3, Jan 2007, pp. 693–695.

[9] Huang, X. and Zhang, X., "Streamwise and spanwise plasma actuators for flow-induced cavity noise control," *Physics of Fluids*, Vol. 20, No. 3, Jan 2008, pp. 7101–7110.

[10] Chan, S., Zhang, X., and Gabriel, S., "Attenuation of Low-Speed Flow-Induced Cavity Tones Using Plasma Actuators," *AIAA journal*, Vol. 45, No. 7, Jul 2007, pp. 1525–1538.

[11] de Jong, A. T. and Bijl, H., "The aero-acoustic resonance behavior of partially covered slender cavities," *Experiments in Fluids*, Vol. 51, No. 5, 2011, pp. 1353–1367.

[12] de Jong, A. T. and Bijl, H., "Investigation of higher spanwise Helmholtz resonance modes in slender covered cavities," *Journal of the Acoustical Society of America*, Vol. 128, No. 4, 2010, pp. 1668–1678.

[13] de Jong, A. T., Bijl, H., Hazir, A., and Wiedemann, J., "Aeroacoustic simulation of slender partially covered cavities using a Lattice Boltzmann method," (paper submitted).

[14] Nati, G., Paper submitted), Title = Suppression of vortex shedding from a truncated trailing edge by plasma actuation, Year = 2011.

[15] Huang, X., Chan, S., Zhang, X., and Gabriel, S., "Variable Structure Model for Flow-Induced Tonal Noise Control with Plasma Actuators," *AIAA journal*, Vol. 46, No. 1, Jan 2008, pp. 241–250.

[16] White, F. M., *Viscous Fluid Flow*, McGraw-Hill, 2nd ed., 1991.

[17] Hankey, F. and Shang, J., "Analyses of pressure oscillations in an open cavity," *AIAA journal*, Vol. 18, No. 8, 1979, pp. 892–898.

[18] Sarohia, V., "Experimental investigation of oscillations in flows over shallow cavities," *AIAA journal*, Vol. 15, No. 7, 1977, pp. 984–991.

[19] Rossiter, J., "Wind tunnel experiments on the flow over rectangular cavities at subsonic and transonic speeds," *Royal Aircraft Establishment*, , No. TR 64037.

[20] Chatellier, L., Laumonier, J., and Gervais, Y., "Aeroacoustic coupling in cavities at low Mach number," *7th AIAA/CEAS Aeroacoustics Conference*, No. AIAA-2001-2131, AIAA, Maastricht, The Netherlands, May 2001.

Part III

Simulation capabilities

Chapter 6

Airfoil sharp trailing edge aeroacoustics using a Lattice Boltzmann method

This chapter is based in part on a workshop paper:

First AIAA Workshop on Benchmark problems for Airframe Noise Computations (BANC-I)
Airfoil sharp trailing edge aeroacoustics using a Lattice Boltzmann method
A.T. de Jong and H. Bijl

Presented during the 2010 AIAA/CEAS Aeroacoustics conference
9-10 June 2010, Stockholm, Sweden

The Lattice Boltzmann method (LBM) is an inherently compressible scheme that is capable of simulating acoustic wave propagation as well as fluid flow. Turbulent airfoil sharp trailing edge noise has been selected as a test case for LBM to investigate the fluid dynamic and acoustic behavior. This because of the fluid dynamic features that are present (turbulent boundary layers) combined with more decoupled acoustics compared to cavity noise (no feedback or resonance). LBM is used to simulate aeroacoustic sharp trailing edge noise of NACA 0012 and DU 96-180 airfoils for 0 and 7 degrees angle of attack. Both natural and tripped turbulence transition has been investigated. For tripped simulations, a zigzag type turbulator has been implemented. An additional high resolution simulation has been conducted for the tripped NACA 0012 case at 0 degrees angle of attack. The far-field noise at two chords distance is calculated using a Ffowcs-Williams Hawkings (FW-H) formulation and is compared to simulated acoustics pressures directly obtained from the flow simulation domain. In order to compensate for the cyclic wall conditions in the spanwise direction, both a time based and frequency based analysis is conducted. Both FW-H and directly obtained sound field have been normalized and compared to results in literature. The high resolution simulation matches the sound pressure level and frequency distribution well, the lower resolution simulations show an over-prediction in sound pressure level.

6.1 Introduction

Noise reduction is an important part of engineering design in the transportation industries. Airplanes, automobiles and trains all produce noise that disturbs passengers, operators and the surrounding communities. On a typical airplane geometry there are several possible sources for aeroacoustic sound production [1]. These include broadband noise due to turbulent boundary layer vortices interacting with the wing and flap trailing edges [2].

A sharp trailing edge of an airfoil with a high Renolds number attached turbulent boundary layer emits broad band noise. In literature, most simulations employ a two-step approach, simulating the fluid flow first after which a separate acoustic simulation is employed [3], using sources from an acoustic analogy. In the current chapter, a single step simulation involving both the acoustic field and fluid dynamics in one simulation is evaluated instead.

The ability to directly simulate high Reynolds number trailing edge noise is investigated using the Lattice Boltzmann Method (LBM), an inherently compressible scheme that recovers acoustics as well as fluid dynamics. It is based on kinetic equations for particle distribution dynamics. Some fundamental aeroacoustic capabilities of the scheme have been studied before, such as wave propagation and compressible behavior [4, 5, 6, 7, 8, 9, 10, 11, 12, 13]. In these cases the method has been shown to correctly simulate these acoustics related problems. However, no detailed investigation of the ability of the scheme to simulate high Reynolds number turbulent trailing edge noise has been performed so far. Furthermore, only limited attempts have been made to capture the acoustic pressure fluctuations from LBM in the far field directly and compare with experiments. Sanjosé et. al. [14] simulated a controlled diffusion airfoil with LBM at a low Reynolds number around 10^5, where the effect of a laminar separation bubble was investigated in detail. The sound emissions where compared with experiments, where a 10 dB over-prediction from the simulation was observed

High Reynolds number trailing edge noise has been chosen for single-step LBM simulations because it is an interesting test case to evaluate if the aeroacoustic behavior of turbulent flows without feedback is adequately captured. The trailing edge noise mechanism does not involve feedback or resonance from the acoustic field. The research questions of the current investigation are: to evaluate the capability of the used LBM scheme to capture the right fluid dynamics and acoustic emission, and to investigate what is needed to directly obtain correct acoustic amplitudes in the far-field. As most simulations regarding trailing edge noise use an acoustic analogy, the acoustic far field is calculated using an analogy and compared to the directly obtained sound field. An investigation regarding the effect of the cyclic simulation boundary conditions in span is conducted as part of the comparison. Both the acoustic analogy and direct sound field are compared to experiments.

This paper concerns the simulation of sharp trailing edge noise of generic airfoil shapes. Two airfoils shapes are evaluated, NACA 0012 and DU 96-180, for 0 and 7 degrees angle of attack. The chord based Reynolds number is 10^6. Both free and forced turbulence transition have been implemented. Simulations are performed using the LBM based commercial code PowerFLOW. All simulations are fully three-dimensional, time-revolved, compressible and viscous.

Section 6.2 describes the Lattice Boltzmann method in detail and section 6.3 describes the numerical setup. The simulation details including computational costs are depicted for the 7 performed simulations in the same section. In sections 6.4 and 6.5 the fluid dynamics and acoustics results are given respectively.

6.2 Lattice Boltzmann Method

Numerical simulation results of flow and acoustics are obtained using the Lattice Boltzmann Method (LBM) [15]. LBM is an alternative numerical method to traditional partial differential equation based computational fluid dynamics for simulating complex fluid flows. Unlike conventional methods based on macroscopic continuum equations, the LBM starts from mesoscopic kinetic equations, i.e., the Boltzmann equation, to determine macroscopic fluid dynamics. The commercial LBM based package PowerFLOW is used.

Kinetic equations are solved on a cartesian mesh (the lattice) by explicit timestepping and collision modeling. The lattice Boltzmann equation has the following form:

$$f_i\left(\mathbf{x}+\mathbf{c_i}\Delta t, t+\Delta t\right)-f_i\left(\mathbf{x},t\right)=C_i\left(\mathbf{x},t\right), \tag{6.1}$$

where f_i is the particle distribution function moving in the ith direction, according to a finite set of the discrete velocity vectors $\{\mathbf{c_i} : i = 0, ..., N\}$. $\mathbf{c_i}\Delta t$ and Δt are space and time increments respectively. The collision term on the right hand side of Eq. (6.1) adopts the simplest and also the most popular form known as the Bhatnagar-Cross-Krook (BGK) form [16]:

$$C_i\left(\mathbf{x},t\right)=-\frac{\Delta t}{\tau}\left[f_i\left(\mathbf{x},t\right)-f_i^{\mathrm{eq}}\left(\mathbf{x},t\right)\right]. \tag{6.2}$$

Here τ is the relaxation time parameter, and f_i^{eq} is the local equilibrium distribution function, which depends on local fluid dynamic properties. The basic fluid dynamic quantities, such as fluid density ρ and velocity $\mathbf{u}$, are obtained through moment summations over the velocity vectors; i.e.

$$\rho\left(\mathbf{x},t\right)=\sum_i f_i\left(\mathbf{x},t\right),\ \rho\mathbf{u}\left(\mathbf{x},t\right)=\sum_i \mathbf{c_i}f_i.\left(\mathbf{x},t\right). \tag{6.3}$$

In the low frequency and long-wave-length limit, for a suitable choice of the set of discrete velocity vectors, one can recover the compressible Navier-Stokes equations through the Chapman-Enskog expansion [15]. The resulting equation of state obeys the ideal gas law, $p = \rho RT$. The kinematic viscosity of the fluid is related to the relaxation time parameter, τ , by [4]:

$$\tau = \frac{\nu}{RT} + \frac{\Delta t}{2}. \tag{6.4}$$

The combination of Eq. (6.1) to (6.4) forms the LBM scheme.

By recovering the compressible Navier-Stokes equations, including an ideal gas equation of state, LBM also inherently recovers acoustics. Some fundamental aeroacoustic capabilities of the scheme have been studied before, such as wave propagation and compressible behavior [4, 5, 6, 7, 8, 9, 10, 11, 12, 13]. In these cases the code has proven itself capable of correctly simulating these acoustics related problems. Examples of the use of the Lattice Boltzmann scheme in acoustics are simulation of radiation from waveguides, [17], acoustic pulses in flows and duct aeroacoustics [18], landing gear noise [19, 20], underbody and wind noise [21, 22], HVAC noise [23, 24] and sunroof buffeting [25, 26].

The Lattice Boltzmann equation is solved on a grid composed of cubic volumetric elements (the Lattice). Variable resolution is allowed, where the grid size changes by a factor of two for adjacent resolution regions.

Due to the explicit time-stepping characteristics of the scheme, the timestep size is increased with cell size in factors of two as well. This will cause the larger cells to not be evaluated for each timestep of the smallest cell and gives rise to the notion of timestep equivalent number of cells (number of cells scaled to operation at the shortest timestep) in addition to the total number of cells. The timestep equivalent number of cells is a better indicator for the amount of computational work than the total number of cells.

The kinematic viscosity of the fluid is related to the relaxation time parameter τ [27]. A viscosity model can be implemented through the relaxation time τ to locally adjust the numerical viscosity of the scheme. For the trailing edge simulations, an implicit large eddy simulation model (ILES) is used, where the subgrid scale viscosity is modeled through the numerical dissipation of the scheme. This allows for the direct simulation of smaller vortex structures compared to the turbulence model that is incorporated into the Powerflow LBM scheme. The original turbulence model consists of a two-equation $K-\epsilon$ Renormalization Group (RNG) modified to incorporate a swirl based correction that reduces the modeled turbulence in presence of large vortical structures. Due to the lower dissipation of the ILES scheme, a lower resolution is needed to ensure that enough vortex scales are simulated to obtain the correct fluid dynamic behavior. Fully resolving the near wall region is computationally too expensive for high-Reynolds-number turbulent flows. Therefore, a turbulent wall model is used to provide approximate boundary conditions. In the current study, the following wall- shear stress model based on the extension of the generalized law of wall is used [4, 21]

$$u^+ = f\left(\frac{y^+}{A}\right) = \frac{1}{\kappa}\ln\left(\frac{y^+}{A}\right) + B, \tag{6.5}$$

with

$$A = 1 + f\left(\frac{\mathrm{d}p}{\mathrm{d}x}\right). \tag{6.6}$$

This equation is iteratively solved to provide an estimated wall-shear stress for wall boundary conditions in the LBM calculation. A slip algorithm [4] (a generalization of bounce-back and specular reflection process) is then used for the boundary process.

6.3 Geometry outline and computational resources

The focus is broadband noise generation of actual airfoils in a uniform flow. The objective is to simulate the emitted noise from a sharpened 12% thick NACA 0012 and sharpened 18% thick DU 96-180 airfoils. Trailing edge sharpening has been included to omit tonal emissions due to vortex shedding. The free stream velocity is set to 70 m/s. For the NACA 0012 airfoil, the chord is 0.22 m, resulting in a Reynolds number of $1.0 \cdot 10^6$. For the DU 96-180 airfoil the chord is 0.5 m giving a Reynolds number of $2.3 \cdot 10^6$. The used angles of attack are 0 degrees and 7 degrees. The airfoil shapes are given in figure 6.1.

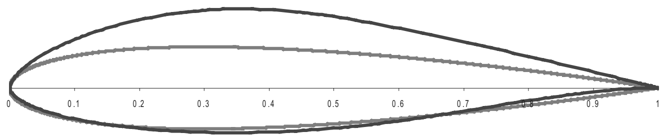

Figure 6.1: Investigated airfoil shapes: grey NACA 0012, black DU 96-180.

The simulations are three dimensional with a small spanwise width compared to the airfoil chord. Most simulations are performed with a spanwise width of 1/4 chord, except for one single high resolution simulation which is performed with a spanwise width of 1/8 chord. Further simulation details are provided in table 6.1. The 1/4 and 1/8 chord spans are sufficiently large compared to the boundary layer spanwise correlation length to ensure that no influences of the spanwise width occur. The simulation domain is periodic in the spanwise direction. The airfoil setups are shown in figure 6.5. The simulation domain contains damping regions in the far field with increased viscosity to eliminate acoustic reflections. The outer domain boundary is chosen far enough to assure that no remaining startup reflections will reach the airfoil within the simulation time.

Two distinctly different case setups have been implemented on the airfoil sections; a clean airfoil simulation and one with turbulator strips used as explicit turbulent tripping devices. In case of a clean airfoil, turbulent fluctuations are naturally introduced by flow instabilities in the boundary layer. The complete airfoil is then modeled as a friction wall. In case of a turbulated airfoil, a zigzag type turbulator strip has been included in the geometry at the maximum thickness location, on both the top and bottom side of the airfoil. A frictionless region is implemented upstream of the strip to proximate the effect of a thin laminar upstream boundary layer. The dimensions of the strip have been chosen to mimic turbulators used in windtunnel experiments conducted at Delft University of Technology in order to provide a means of direct comparison in the future. For the 0.22 m chord airfoil, the strip has a height of 0.63 mm, a streamwise length of 7 mm. The spanwise width of each V-shaped section varies, for the normal resolution simulations of spanwise width $\frac{W}{C} = 1/4$, 9 V-shaped sections have been implemented, resulting in a 6.1 mm wide section, or a V-shape angle of 47 degrees. For the high resolution simulation with a smaller spanwise domain width of $\frac{W}{C} = 1/8$ (run number 7 in table 6.1), 6 V-shaped sections have been implemented, resulting in a smaller section width of 4.6 mm and a sharper V-shape angle of 36 degrees. The sharper angle has been implemented to ensure sufficient breakup of spanwise correlations for the smaller spanwise simulation domain.

Simulation details are provided in table 6.1. Variable resolution regions have been implemented around the airfoil. The resolution regions are given in figure 6.2 for the clean, tripped and high resolution cases. The finest resolution is set around the zigzag strips and has 0.11 mm cell size. The boundary layer has a cell size of 0.43 mm, or 512 cells per chord length. The outer domain cell size is 28 mm. The resolution regions in the wake are extended beyond the airfoil in order to minimize erroneous non-physical noise sources from the passing of vortices through resolution regions. For the clean airfoil simulations, the two finest resolution regions around the turbulator strip are omitted and the boundary layer resolution region is extended to include the front of the airfoil section. In this case the boundary layer resolution with cell size 0.43 mm is the finest resolution region.

The computational load is also given in table 6.1. The CPU-hr count is based on simulation on 1 node with 8 processors, Intel Xeon E5520, 2.27 GHz. The total simulated physical time is around 0.25 seconds. Due to the Lattice Boltzmann collision scheme setup, a coarser resolution region is not calculated every timestep but every other timestep. An increase in local cell size by a factor 2N causes a reduction in needed timesteps by a factor 2N. By accounting for this gain in efficiency, the amount of fine equivalent volume cells can be evaluated. Both the total cell counts and the fine equivalent cell counts are included in table 6.1. One can also observe that for the same physical time, the turbulated simulations require 4 times the amount of timesteps due to the decrease in finest cell size compared to clean airfoil simulations.

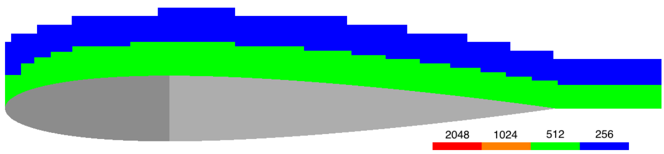

(a) Free transition, normal resolution

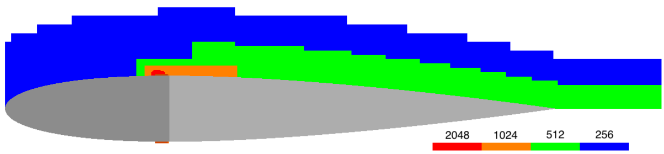

(b) Forced transition, normal resolution

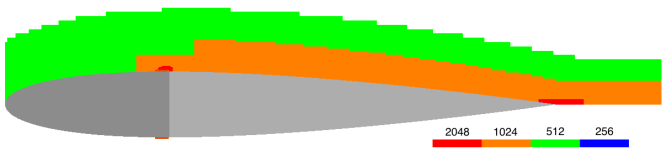

(c) Forced transition, high resolution

Figure 6.2: Resolution regions for airfoil with turbulator strips. Normal resolution settings (top, middle) and high resolution setting (bottom). Resolution described in voxels per chord length.

Run nr	1	2	3	4	5	6	7
Airfoil (NACA0012/DU96-180)	N	N	D	D	N	N	N
Transition (Free/Turbulator)	F	T	F	T	F	T	T
Resolution (Normal/High)	N	N	N	N	N	N	H
Angle [degrees]	7	7	7	7	0	0	0
Spanwise width/chord length [-]	1/4	1/4	1/4	1/4	1/4	1/4	1/8
Airfoil surface res. [cells/chord]	512	512	512	512	512	512	1024
Turbulator res. [cells/chord]	n/a	2048	n/a	2048	n/a	2048	2048
Trailing edge res. [cells/chord]	512	512	512	512	512	512	2048
Smallest cell size [mm] 0.43	0.11	0.43	0.11	0.43	0.11	0.11	0.11
Cell count [mln]	9.4	11.8	11.8	12.9	9.3	11.6	40.7
Fine equivalent cell count [mln]	3.8	2.6	3.9	2.5	3.7	2.5	19.6
Timesteps per 0.1 sec [x1000]	141	564	141	564	141	564	564
CPUhrs per 0.1 sec	266	816	284	781	283	785	3085

Table 6.1: Simulation setup and computational cost details

In the current chapter, most focus is put on the NACA0012 airfoil configuration at 0 degree angle of attack because of the availability of references in literature for this specific setup. The DU 96-180 geometry has been presented in more detail at the BANC-I workshop [28].

6.4 Fluid dynamic results

In the current section the fluid dynamic results are given. Mean pressure distributions and turbulent vortical structures are evaluated. The acoustics results are presented in section 6.5.

6.4.1 Pressure distributions

The LBM airfoil pressure distributions are compared to panel method calculations in order to check if the simulated fluid dynamic behavior shows the correct trends. Figure 6.3 shows the time averaged surface pressure coefficient Cp along the NACA 0012 airfoil at 0 degrees angle of attack. Both the free transition and the tripped case are depicted. Xfoil [29] panel method results have been added for comparison. 500 panels per surface have been implemented. Free boundary layer transition is calculated using an incorporated e^n method [29]. For forced transition, the transition location has been specified. Viscous and compressible solutions with matching Reynolds number and Mach number compared to LBM simulations have been calculated.

For the LBM free transition case, transition into turbulence occurs around $x/c \approx 0.6 - 0.7$, in agreement with the free transition location found in Xfoil of $x/c = 0.66$. The Cp distribution after the transition point shows some deviation compared to the reference, which might be attributed to the influence of local grid resolution on the transition process. This is not investigated in further detail at the moment. For the tripped airfoil case with turbulator strip at x/c=0.3 the Cp distribution of figure 6.3 also agrees well with the Xfoil reference. The presence of the turbulator strip is clearly visible in the Cp distribution,which might be attributed to the relative large height of the strip, 0.63 mm. The panel method calculations do not take into account the effect of turbulator thickness and therefore do not show the same gradients in Cp in the vicinity of the turbulator location.

Figure 6.4 shows the time averaged Cp on the NACA 0012 and DU 96-180 airfoil top and bottom surfaces at 7 degrees angle of attack. Xfoil viscous panel method results are again included for comparison. The results once again closely resemble those given by Xfoil. The blockage of the turbulator strip is visible at 30% chord in both subfigures.

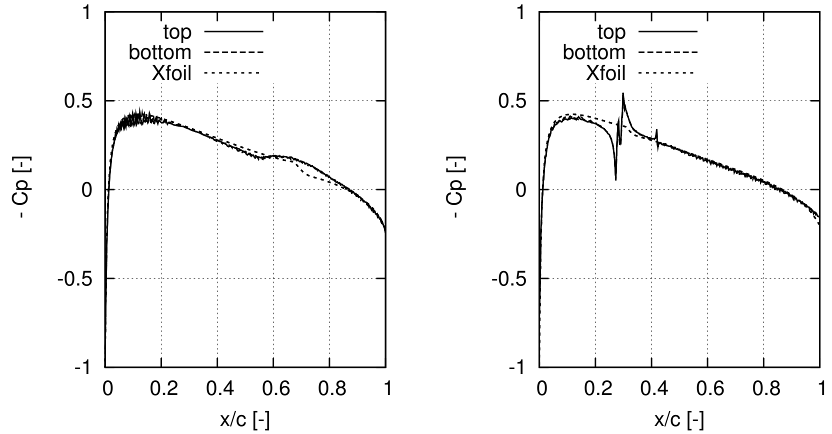

(a) clean airfoil (b) with turbulator

Figure 6.3: Time averaged Cp both sides, NACA 0012, 0 degrees angle of attack, Xfoil results included.

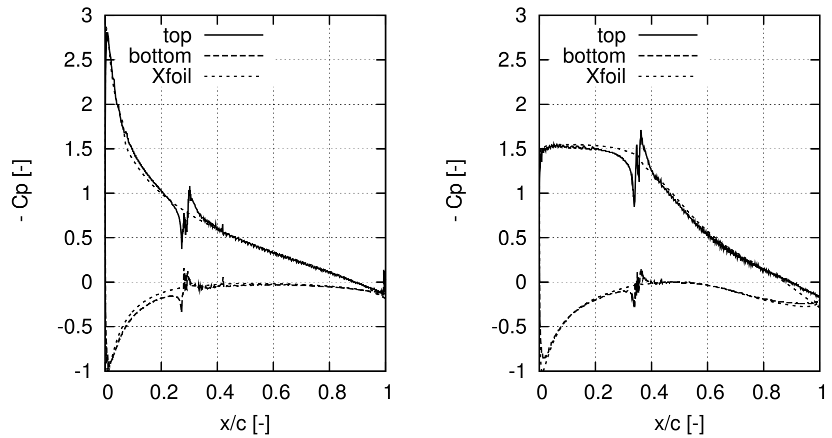

(a) NACA 0012, 7 degrees angle of attack, with turbulator (b) DU 96-180, 7 degrees angle of attack, with turbulator

Figure 6.4: Time averaged Cp both sides, 7 degrees angle of attack with turbulator, Xfoil results included.

6.4.2 Flow structures: free versus forced transition

The coherent vortex structures in the boundary layer and wake are visualized by plotting λ_2 iso-surfaces. λ_2 is the second largest Eigenvalue of $S^2 + \Lambda^2$, with S the symmetric deformation tensor and Λ the anti-symmetric spin tensor [30]. Figure 6.5 shows the NACA 0012 iso-surfaces of λ_2, colored by velocity magnitude. The angle of attack is 0 degrees, corresponding to the pressure distributions of figure 6.3. Both the tripped and free airfoil cases show a full development of breakup of spanwise correlations into turbulent structures. The free transition into turbulence around $x/c \approx 0.6$ is clearly visible. For the free transition case, the largest turbulent vortical structures are larger than in the tripped case, which can once more be attributed to the resolution of the simulation around free transition. For the tripped case, the turbulator strip located at 30% chord functions well, with wake structures from the strip disappearing into the turbulent fluctuations around 35-40% chord.

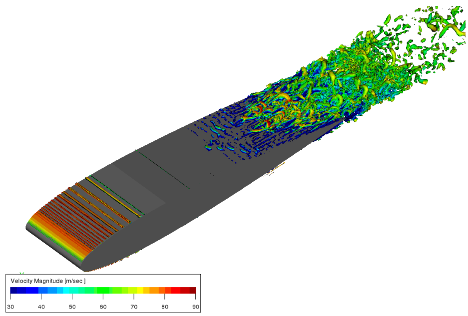

(a) Clean

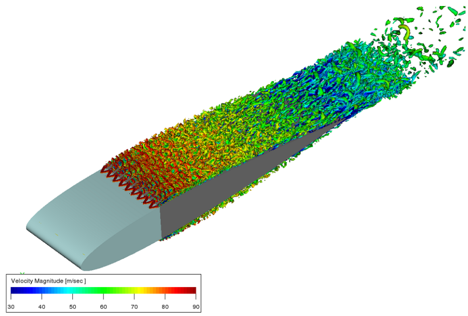

(b) Turbulator

Figure 6.5: NACA 0012, 0 degrees angle of attack, Isosurface of $\lambda 2 = -100$ colored by velocity magnitude. Frictionless regions are indicated in light blue.

The effect of angle of attack is investigated qualitatively in order to see if the trends in fluid dynamic behavior correspond to physical expectations. Figure 6.6 depict the iso-surfaces of λ_2 for the suction (top) and pressure (bottom) side of the NACA 0012 airfoil at 7 degrees angle of attack. By comparing the NACA 0012 airfoil of figure 6.6 for 7 degrees with figure 6.5 for 0 degrees, one can clearly see that the transition into turbulence is dependent on the angle of attack and therefore on the pressure gradient. For the NACA 0012, the transition point on the suction side has moved up to $x/c \approx 0.3$ for 7 degrees angle of attack. In case of tripping, there is a difference in turbulence intensity between the upper and lower airfoil side. The adverse pressure gradient on the suction side promotes development of turbulent vortical structures whereas on the pressure side turbulence intensities are reduced further downstream of the strip. The overall trends in behavior of both the airfoils due to the change in angle of attack is according to physical expectations. A more detailed quantitative investigation on the fluid dynamic effects is omitted here, as it is deemed outside the scope of the current work.

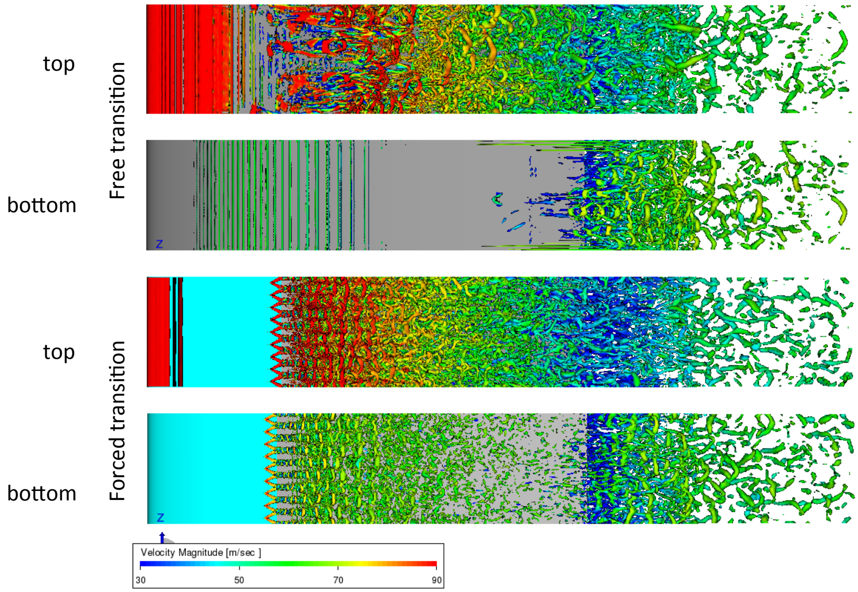

Figure 6.6: NACA 0012 at 7 degrees angle of attack, Isosurface of $\lambda 2 = -100$ colored by velocity magnitude. Frictionless regions are indicated in light blue.

6.4.3 Flow structures: normal versus high resolution

A high resolution simulation has been performed for the NACA 0012 airfoil at 0 degree angle of attack, (simulation number 7 from table 6.1). This is compared to the normal resolution case at similar conditions (simulation number 6 from table 6.1). A tripped setup was chosen for the high resolution simulation to eliminate the possible effect of grid resolution on transition location. To minimize computational costs, a smaller spanwise width of $\frac{W}{C} = 1/8W/C = 1/8$ was used and the turbulator strip was modified with sharper V-shaped angles to ensure sufficient breakdown of spanwise correlation within the simulation domain.

Figure 6.7 depicts the NACA 0012 λ_2 iso-surfaces at 0 degrees angle of attack for both the normal and high resolution case. The smaller spanwise width and modified turbulator strip are clearly visible in the figure. $\lambda_2 = -100$ is depicted for the normal resolution case and $\lambda_2 = -1200$ for the high resolution case. Figure 6.7 also shows a zoom around the airfoil trailing edge. The turbulent structures are smaller for the high resolution case, which is in accordance with expectations. As mentioned before in section 6.2, the implemented ILES model allows for direct simulation of small vortex structures. As the numerical dissipation of the scheme is employed as the viscous dissipation for small scales, smaller scale vortices are expected to appear with increasing resolution.

Figure 6.8 shows the instantaneous velocity magnitude from a streamwise vertical plane through the airfoil center. The sharper V-shape angle of the turbulator

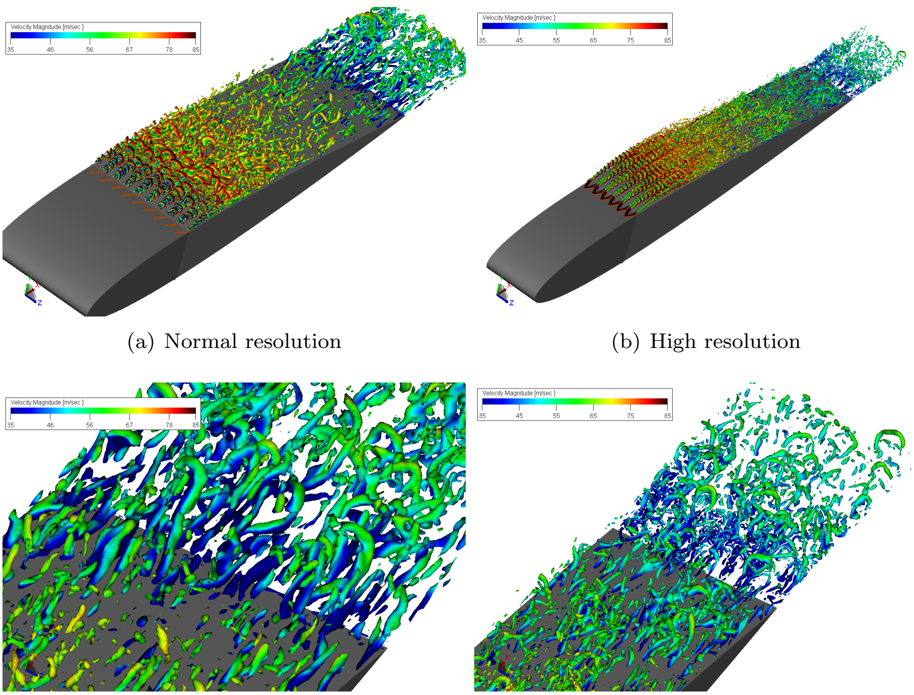

(a) Normal resolution

(b) High resolution

(c) Normal res., zoom around trailing edge

(d) High res., zoom around trailing edge

Figure 6.7: NACA 0012, 0 degrees angle of attack, Isosurface of λ_2 colored by velocity magnitude. Isosurface value $\lambda_2 = -100$ for normal resolution and $\lambda_2 = -1200$ for high resolution case. Please note that the viewpoints are the same for the normal and high resolution cases.

strip for the high resolution case (as explained in more detail in section 6.3) has an influence on the flow; the wake of the strip is moved up into the higher regions of the boundary layer. This in effect causes a velocity deficit in the higher regions of the boundary layer that spreads due to mixing. It is thus important to pay attention to the detailed design of the turbulator when using forced transition.

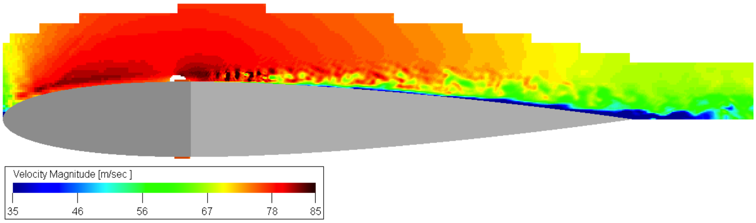

(a) Normal resolution

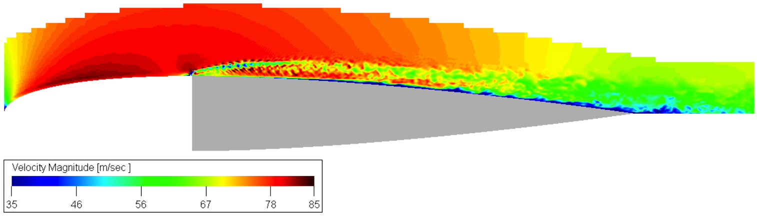

(b) High resolution

Figure 6.8: NACA 0012, 0 degrees angle of attack, instantaneous velocity magnitude.

6.5 Acoustics

Due to the fact that LBM is inherently compressible and provides a time-dependent solution, the sound pressure field can be directly obtained from the computational domain, provided that there is sufficient resolution to capture the acoustic waves [4, 5, 6, 7, 8, 9, 10, 11, 12, 13]. Figure 6.9 illustrates this by showing a sample time instance of the fluctuating direct pressure field in combination with a depiction of the vorticity around the airfoil.

Most trailing edge noise simulations employ an acoustic analogy to obtain the far-field noise. The research objective of this section is to investigate the ability of LBM to directly simulate the acoustic field. Therefore the directly obtained sound field from simulation is compared with an acoustic analogy based on the simulation fluid dynamics. In order to compare, an adjustment for the cyclic simulation domain in the spanwise direction is needed. Both methodologies for the simulation sound pressure level are then compared to experimental results from literature in order to assess if the acoustic emission from the trailing edge was simulated correctly.

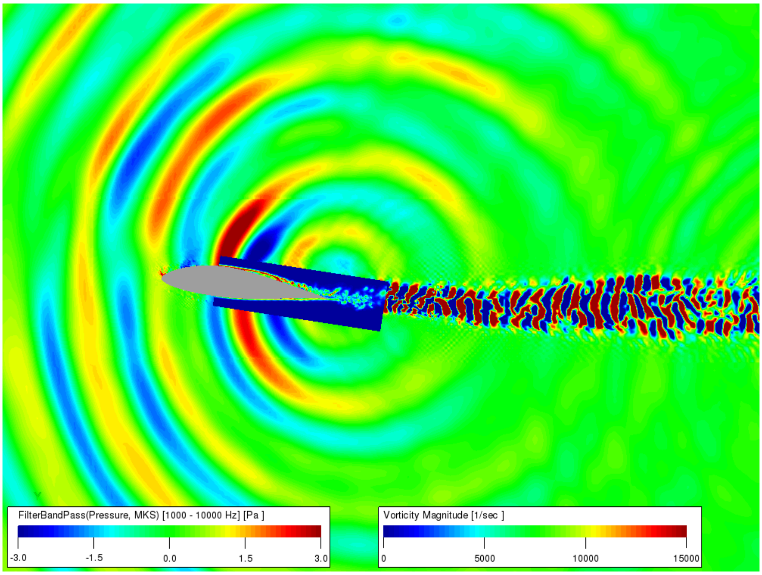

Figure 6.9: Directly simulated pressure band filtered from 1000 to 10000 Hz together with vorticity magnitude in the region around the airfoil

6.5.1 Direct sound field versus FW-H results

The ability of the LBM scheme to recover the acoustic field is tested by comparing with an indirect porous Ffowcs-Williams Hawkings [31] (FW-H) analogy method. The McGill Acoustic Analogy Package (MCAAP) is used for the indirect far-field sound prediction. MCAAP uses a modified porous Ffowcs-Williams Hawkings surface integral acoustic method, which takes into account the effect of mean flow on sound propagation. MCAAP utilizes the advanced time approach [32, 33, 34] to predict the far-field sound pressure history from the near-field data obtained from CFD simulations.

Due to the cyclic boundary conditions and the limited width of 1/4 or 1/8 chord, the sound pressure directly measured in the simulation domain contains contributions from mirrored coherent image sources of the airfoil arriving through the cyclic domain boundaries to the microphone location. This can alternatively be viewed as the airfoil sound emission arriving not only at the microphone but also at image microphones mirrored through the cyclic domain boundaries. The total sound field is then the addition of the signal from the microphone location and the mirrored microphone images. Figure 6.10 provides an scetch for the simulation cross-section with the mentioned image contributions. In order to compensate for these effects, a correction can be employed in the time domain or in the frequency domain. Both options are evaluated to compare the FW-H emissions with the directly measured sound field at two chord lengths distance above the airfoil.

In order to compare the results in the time domain, the FW-H signal is mod-

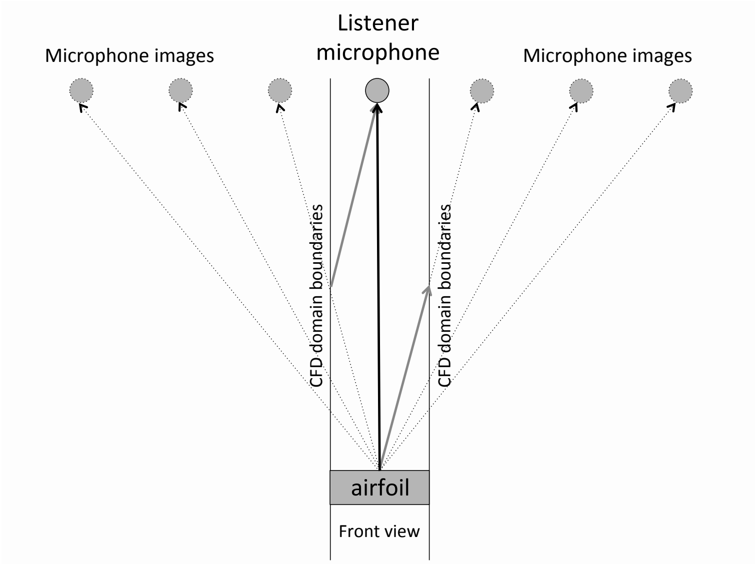

Figure 6.10: Acoustic images due to spanwise simulation domain boundaries

ified to match the conditions of the directly obtained signal. This is done by accounting for phase delay and reduction in sound amplitude due to the increased distance between the image sources and microphone location through the simulation boundaries. For a semi-spherical sound emission, the sound pressure level amplitude will decay proportional to increasing distance as $p \propto \frac{1}{d^2}$. The modified pressure time series based on phase delay and amplitude decay can be calculated as:

$$p_{FWH,mod}(t) = p_{FWH}(t) + 2\sum_{n=1}^{N} \alpha_n p_{FWH}(t - t_n). \tag{6.7}$$

Here $t_n = \frac{d_0 - d_n}{v_s}$ the time delay between the direct path to the measurement point d_0 and the path through the cyclic boundary conditions $d_n = \sqrt{d_0^2 + (n \cdot W)^2}$. v_s is the speed of sound and W the simulation domain width. $\alpha_n = \frac{d_0^2}{d_n^2}$ is the amplitude reduction due to wave expansion.

Figure 6.11 shows a sample of the time series for the model (2 chords distance, 90 degrees angle) both directly obtained and FW-H. With an increasing number of spanwise sections N the time-domain reconstructed signal (named FW-H cyclic in the figure) does approach the directly measured pressure signal. For 32 cyclic sections in the time domain, the signals match well. This confirms that the directly obtained pressure and FW-H signal provide the same data, only that a transformation is needed to take into account the effect of the cyclic domain on the acoustics. A amplitude scaled FW-H result included in the figure as well. This scaled FW-H result is obtained by simple amplitude scaling of the ratio of variances between the direct signal and the FW-H. In this way, one can observe that simple scaling does not match the directly measured signal shape. The correct transformation can thus not be obtained by simply scaling the amplitudes, the effect of phase shifts according to equation (6.7) need to be taken into account.

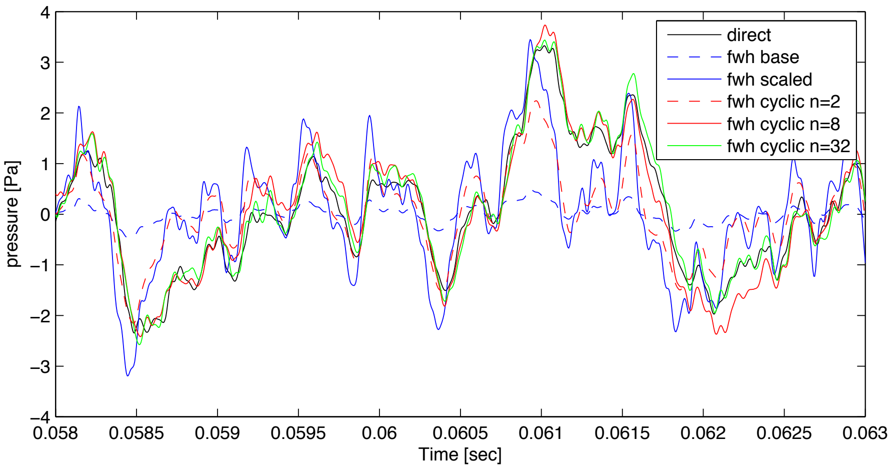

Figure 6.11: Comparison pressure time series modified FW-H solutions with directly obtained pressure signals at r=2c.

In addition to the time domain analysis presented above, a frequency domain adjustment to account for cyclic spanwise boundaries can be used. Oberai [3, 35] implemented a three-dimensional correction for low Mach number flows:

$$\hat{p}(r,\theta) = p(r,\theta)\frac{b(1+i)}{2}\sqrt{\frac{k}{\pi d}}, \tag{6.8}$$

where k is the wave number and d is the observer distance. For the current simulations with a limited domain width b this gives a frequency dependent spectral modifier for the sound pressure level in dB scaling:

$$\Delta L_{cyclic} = 10 \cdot log\left(\frac{fb^2}{v_c d}\right). \tag{6.9}$$

The spectra obtained using this scaling match the FW-H spectra well. The formulation of 6.9 is more useful than the time domain analysis, as it provides a way to modify the directly obtained pressure signal to be comparable to experimental results in unbounded three dimensional space.

6.5.2 Directivity

It is known from experiments and analytical investigations that the acoustic radiation of trailing edge noise has the highest sound pressure level in an oblique upstream direction [2, 36]. Also the frequency of maximum radiation increases with higher upstream angles. A check is performed whether or not the LBM results show an upstream directivity to the emitted sound pressure field.

In polar figure 6.12 the far field noise sound pressure levels are given at r/c=2 distance for various angles with respect to the trailing edge for a number of frequency bands. The sound pressure level is given with units of Pa. The plot shows that there is a tendency to propagate more trailing edge noise upstream, as observed in experiments [2]. Brooks et. al. [2] presented a directivity function for the emitted sound pressure levels:

$$D\left(\theta_r\right) = \frac{2sin^2\left(\theta_r/2\right)}{\left(1+Mcos\left(\theta_r\right)\right)\left[1+0.4Mcos\left(\theta_r\right)\right]^2}, \tag{6.10}$$

with θ_r the emission angle in retarded coordinates and M the Mach number. This directivity function is added to figure 6.12, scaled so that the amplitude of emission is matched to the 120 degree emission in simulation. It can be observed that the directivity of simulation matches the directivity function of equation (6.10) well. The smaller band directivity plots in the figure (1-2 and 2-4 kHz bands) shows that higher frequency emissions have a tendency to radiate forwards at sharper angles, which is in accordance with expectations.

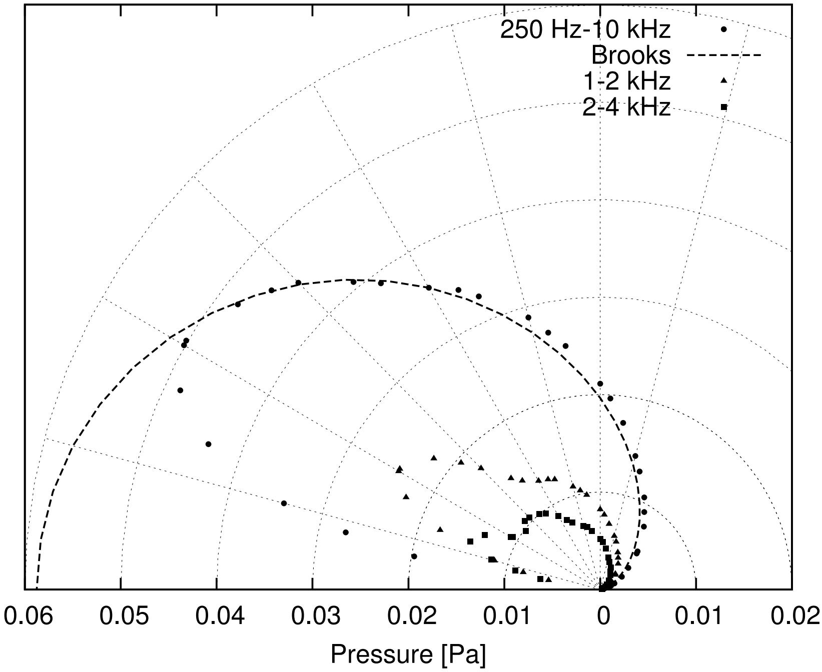

Figure 6.12: Polar plot of SPL directivity for 3 frequency bands. NACA 0012 high resolution case, airflow is from left to right. Directivity function according to Brooks et.al. [2] included.

6.5.3 Comparison with experimental far field measurements

Sound pressure spectra from simulation are compared to experimental results in literature. A variation in physical parameters such as airfoil spanwise width, distance from the trailing edge and Mach number influence obtained sound pressure levels in both simulation and experiment. In order to directly compare the current data with experimental results from literature, the sound pressure spectra obtained from both simulation and experiments are normalized according to [37]:

$$L_{p(1/3)norm} = L_{p(1/3)} - 50\log(M_\infty) - 10\log(\delta^* b/d^2), \tag{6.11}$$

$$Sr = f\delta^*/u_\infty. \tag{6.12}$$

This normalization is based on free stream properties, i.e. the free stream Mach number M_∞ and geometric parameters, such as the distance from the trailing edge d and airfoil width b. The sound pressure levels thus refer to far-field emissions of an airfoil of 1 m spanwise width at 1 m distance.

Figure 6.13 shows the obtained spectra for the NACA 0012 airfoil at 0 degrees angle of attack and 90 degree sound emission angle with respect to the trailing edge direction. The displacement thickness δ^* of the normal and high resolution simulation is 2.3 and 1.9 mm respectively. Both the FW-H based sound field prediction and the directly obtained pressure field from simulation (compensated for spanwise cyclic acoustic effects according to equation 6.9) are presented. In the figure, several experimental results from literature are depicted for comparison. All references concern a NACA 0012 airfoil at 0 degrees angle of attack. Herr [37] conducted experiments at the DLR acoustic open jet windtunnel, the case of a 0.4 m airfoil at 40 m/s is shown. Brooks [2] created a model for the trailing edge SPL based on windtunnel experiments. Oerlemans [38] conducted experiments in an open jet windtunnel for several chord lengths and flow speeds, depicted is the most closely matching case of c=0.22 m and $U_\infty = 73$ m/s. Herrig [39] conducted windtunnel experiments with a 0.2 m long airfoil at several flow speeds, the 60 m/s result is shown.

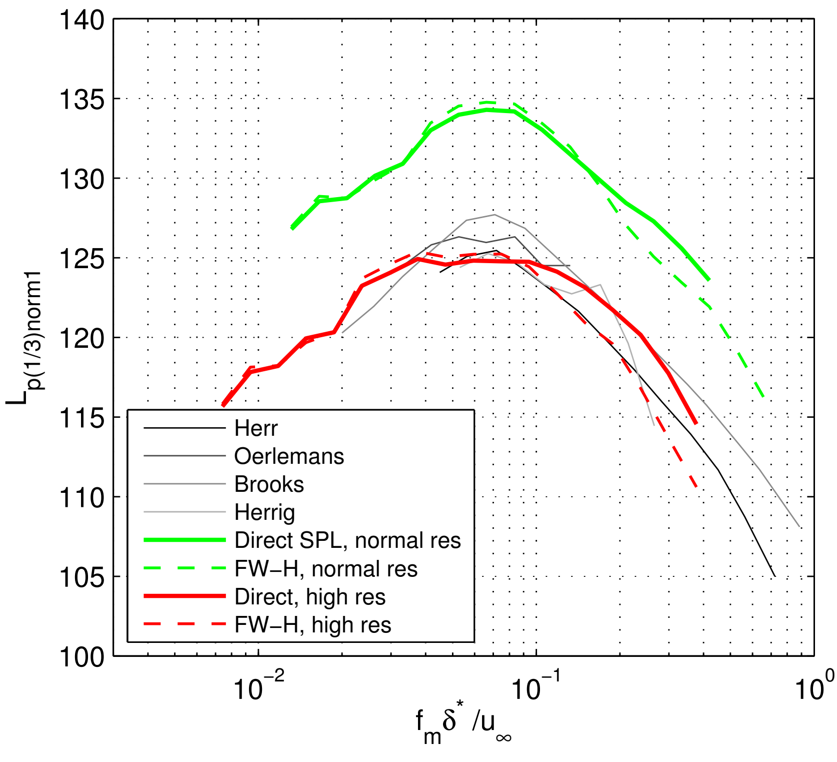

Figure 6.13: Comparison normalized spectra with results in literature for the NACA 0012 airfoil at 0 degrees angle of attack and 90 degree sound emission angle with respect to the trailing edge direction, experimental data and models from Herr [37], Oerlemans [38], Brooks [2] and Herrig [39].

There is some spread between the various sources in literature, even after normalization. This provides an indication of the level of uncertainty in experiment. In general the FW-H and direct method match well with each other. Only at higher frequencies the direct SPL is slightly higher, which could possibly be attributed to reflective noise from the simulation domain resolution interfaces. Considering the experimental spread, one can deduct that the high resolution LBM simulations match the experiments well, both for amplitude and spectral shape. The normal resolution simulations show an over-prediction of SPL, but a good match in frequency of maximum amplitude and spectral shape. The over-prediction in amplitude could be attributed to the increased boundary layer turbulent intensity, the size of the vortical structures, or the lack of resolution in the sound producing region around the trailing edge.

6.6 Conclusions

Three-dimensional aeroacoustic simulations using a Lattice Boltzmann method have been performed. Two airfoil types (NACA 0012, DU 96-180) and two angles of attack (0 and 7 degrees) have been implemented. The airfoils have been simulated with a clean configuration and with a turbulator strip that was forcing boundary layer transition at a fixed location. A final higher resolution simulation has been performed on the NACA 0012, 0 degrees angle of attack, tripped airfoil.

Mean fluid dynamic pressure distributions match reference Xfoil results well for all cases. The simulations show direct generation and convection of time resolved turbulent vortices in the airfoil boundary layer. The free transition location is dependent on the angle of attack. The largest turbulent structures are smaller in the case of tripping using a turbulence strip. The high resolution simulation shows smaller vortices compared to the normal resolution tripped case.

Direct measurements of pressure fluctuations in the simulation are compared to those obtained using the FW-H method and the effect of cyclic boundary conditions on the far-field noise has been investigated in both the time and frequency domain. When compensated for the cyclic spanwise simulation boundaries, the direct and FW-H results match well. The sound field is directed mostly upstream, in agreement with literature. A high resolution simulation sound emission matches well with experiments in literature for amplitude and spectral shape, indicating that the current method can predict both sound production and far field emission in one single simulation. The corresponding normal resolution simulation shows an over prediction of SPL, but a correct frequency of maximum amplitude and spectral shape.

Acknowledgments

I would like to greatly thank Dr. Phoi-tack Lew and Alireza Najafi-Yazdi, for their pleasant collaboration by providing the FW-H far-field calculations. Furthermore, I would like to thank Dr. Dave Freed, Dr. Guillaume Brès, Dr. Franck Pèrot, Dr.

Bernd Crouse and Dr. Swen Noelting from Exa Corp. for their help and useful comments on the simulation setup and for their support in my participation in the BANC-I workshop. I also thank Dr. Dave Freed and Dr. Franck Pèrot for their comments on the draft of this manuscript.

Bibliography

[1] Lilley, G., "The prediction of airframe noise and comparison with experiment," *Journal of Sound and Vibration*, Vol. 239, No. 4, 2001, pp. 849–859.

[2] Brooks, T., Pope, T., and Marcolini, M., "Airfoil self noise and prediction," Tech. Rep. 1218, NASA reference publication, 1989.

[3] Ewert, R. and Schröder, W., "On the simulation of trailing edge noise with a hybrid LES/APE method," *Journal of Sound and Vibration*, Vol. 270, No. 3, 2004, pp. 509–524.

[4] Chen, S. and Doolen, G., "Lattice Boltzmann method for fluid flows," *Annual Review of Fluid Mechanics*, Vol. 30, Jan 1998, pp. 329–364.

[5] Yu, D., Mei, R., Luo, L., and Shyy, W., "Viscous flow computations with the method of lattice Boltzmann equation," *Progress in Aerospace Sciences*, Vol. 39, No. 5, Jan 2003, pp. 329–367.

[6] Tsutahara, M., Kataoka, T., Shikata, K., and Takada, N., "New model and scheme for compressible fluids of the finite difference lattice Boltzmann method and direct simulations of aerodynamic sound," *Computers & Fluids*, Vol. 37, No. 1, Jan 2008, pp. 79–89.

[7] Li, X. M., So, R. M. C., and Leung, R. C., "Propagation Speed, Internal Energy, and Direct Aeroacoustics Simulation Using Lattice Boltzmann Method," *AIAA journal*, Vol. 44, No. 12, Dec 2006, pp. 2896–2903.

[8] Buick, J., Greated, G., and Campbell, D., "Lattice BGK simulation of sound waves," *Europhysics Letters*, Vol. 43, No. 3, Jan 1998, pp. 235–240.

[9] Buick, J., Buckley, C., Greated, C., and Gilbert, J., "Lattice Boltzmann BGK simulation of nonlinear sound waves: The development of a shock front," *Journal of Physics A: Mathematical and General*, Vol. 33, No. 21, Jan 2000, pp. 3917–3928.

[10] Crouse, B., Freed, D. M., Balasubramanian, G., Senthooran, S., Lew, P., and Mongeau, L., "Fundamental Aeroacoustic Capabilities of the Lattice-Boltzmann Method," *12th AIAA/CEAS Aeroacoustics Conference*, No. AIAA-2006-2571, Cambridge, Massachussets, May 2006, pp. 2571–2588.

[11] Brès, G., Pérot, F., and Freed, D. M., *15th AIAA/CEAS Aeroacoustics Conference*, Miami, Florida, May.

[12] Marié, S., Ricot, D., and Sagaut, P., "Accuracy of Lattice Boltzmann method for aeroacoustic simulations," *13th AIAA/CEAS Aeroacoustics Conference*, No. AIAA-2007-3515, Rome, Italy, May 2007.

[13] Marié, S., Ricot, D., and Sagaut, P., "Comparison between Lattice Boltzmann method and Navier-Stokes high order schemes for computational aeroacoustics," *Journal of Computational Physics*, Vol. 228, 2009, pp. 1056–1070.

[14] Sanjoseé, M., Moreau, S., Kim, M. S., and Pérot, F., "Direct Simulation of Trailing-Edge Noise Generated By a Controlled Diffusion Airfoil Using a Lattice-Boltzmann Method," *7th International Symposium on turbulence and shear flow phenomena*, Ottawa, Canada, July 2011.

[15] Succi, S., *The lattice Boltzmann equation for fluid dynamics and beyond*, Oxford University Press, 2001, pp. 11-13.

[16] Bhatnagar, P. L., Gross, E. P., and Krook, M., "A Model for Collision Processes in Gases. I. Small Amplitude Processes in Charged and Neutral One-Component Systems," *Physical Review*, Vol. 94, No. 3, May 1954, pp. 511–525.

[17] da Silva, A. A. and Scavone, G. P., "Lattice Boltzmann simulations of the acoustic radiation from waveguides," *Journal of Physics A*, Vol. 40, 2007, pp. 397–408.

[18] Li, X. M., Leung, R. C., and So, R. M. C., "One-Step Aeroacoustics Simulation Using Lattice Boltzmann Method," *AIAA Journal*, Vol. 44, No. 1, January 2006, pp. 78–89.

[19] Brès, G., Wessels, M., and Noelting, S., "Tandem Cylinder Noise Predictions Using Lattice Boltzmann and Ffowcs Williams-Hawkings Methods," *16th AIAA/CEAS Aeroacoustics Conference*, No. AIAA-2010-3791, Stockholm, Sweden, June 2010.

[20] Noelting, S., Wessels, M., and Freed, D. M., "Prediction of Aeroacoustic Noise from a Simplified Landing Gear Using a Lattice-Boltzmann-Scheme," *46th AIAA Aerospace Sciences Meeting and Exhibit*, No. AIAA-2008-20, Reno, Nevada, January 2008.

[21] Crouse, B., Freed, D. M., Senthooran, S., Ullrich, F., and Fertl, S., "Analysis of Underbody Windnoise Sources on a Production Vehicle using a Lattice Boltzmann Scheme," *SAE Technical Paper*, 2007-01-2400, 2007, doi:10.4271/2007-01-2400.

[22] Pérot, F., Meskine, M., and Vergne, S., "Investigation of the statistical properties of pressure loadings on real automotive side glasses," *15th AIAA/CEAS Aeroacoustics Conference*, No. AIAA-2009-3402, Miami, Florida, May 2009.

[23] Lee, D. K., Pérot, F., and Freed, D. M., "The prediction of the flow induced noise related to automotive HVAC systems," *SAE Technical Paper*, 2011-01-0493, 2011, doi:10.4271/2011-01-0493.

[24] Pérot, F., Kim, D. K., and Lee, D. K., "Direct aeroacoustics prediction of ducts and vents noise," *16th AIAA/CEAS Aeroacoustics Conference*, No. AIAA-2010-3724, Stockholm, Sweden, June 2010.

[25] Crouse, B., Senthooran, S., Balasubramanian, G., Freed, D. M., and Karbon, K., "Computational Aeroacoustics Investigation of Automobile Sunroof Buffeting," *SAE Technical Paper*, 2007-01-2403, 2007, doi:10.4271/2007-01-2403.

[26] Crouse, B., Balasubramanian, G., Senthooran, S., and Freed, D. M., "Investigation of gap deflector efficiency for reduction of sunroof buffeting," *SAE Technical Paper*, 2009-01-2233, 2009, doi:10.4271/2009-01-2233.

[27] Chen, H., "Extended Boltzmann Kinetic Equation for Turbulent Flows," *Science*, Vol. 301, No. 5633, Aug 2003, pp. 633–636.

[28] de Jong, A. T. and Bijl, H., "Airfoil sharp trailing edge aeroacoustics using a Lattice Boltzmann method," *1st AIAA Workshop on Benchmark problems for Airframe Noise Computations (BANC-I), 16th AIAA/CEAS Aeroacoustics Conference*, Stockholm, Sweden, June 2010.

[29] "Xfoil panel method," `http://web.mit.edu/drela/Public/web/xfoil/xfoil_doc.txt` (date last viewed 04/25/12).

[30] Jeong, J. and Hussian, F., "On the identification of a vortex," *Journal of Fluid Mechanics*, , No. 285, 1995, pp. 69–94.

[31] Najafi-Yazdi, A., Brès, G., and Mongeau, L., "An Acoustic Analogy Formulation for Moving Sources in Uniformly Moving Media," *Proceedings of the Royal Society A: Mathematical, Physical and Engineering Sciences*, 2010, pp. pp 1–22.

[32] Lyrintzis, A., "Surface Integral Methods in Computational Aeroacoustics from the (CFD) Near-Field to the (Acoustic) Far-field," *International journal of Aeroacoustics*, Vol. 2, No. 2, 2003, pp. 95–128.

[33]

[34] Brentner, K. and Farassat, F., "Modeling Aerodynamically Generated Sound of Helicopter Rotors," *Progress in Aerospace Sciences*, Vol. 39, No. 2-3, 2003, pp. 83–120.

[35] Oberai, A., Roknaldin, F., and Hughes, T., "Trailing-edge noise due to turbulent flows," Technical report Report No. 02-002, 2002, Boston University, 2002.

[36] Oberai, A. A., Roknaldin, F., and Hughes, T., "Computation of trailing-edge noise due to turbulent flow over an airfoil," *AIAA journal*, Vol. 40, No. 11, 2002, pp. 2206–2216.

[37] Herr, M., Appel, C., and Dierke, J., "Trailing-Edge Noise Data Quality Assessment for CAA Validation," *16th AIAA/CEAS Aeroacoustics Conference*, No. AIAA-2010-3877, Stockholm, Sweden, Dec 2010.

[38] Oerlemans, S., "Wind Tunnel Aeroacoustic Tests of Six Airfoils for Use on Small Wind Turbines," Tech. Rep. NREL/SR-500-35339, National Renewable Energy Laboratory Subcontractor Report, 2004.

[39] Herrig, A., Wuerz, W., E., K., and Wagner, S., "New CPV-Results of NACA0012 Trailing-Edge Noise," *International Conference on Methods of Aerophysical Research, ICMAR*, July 2008.

Chapter 7

Aeroacoustic simulation of slender partially covered cavities using a Lattice Boltzmann method

This chapter is based on the submitted journal paper:

Aeroacoustic simulation of slender partially covered cavities using a Lattice Boltzmann method
A.T. de Jong, H. Bijl, A. Hazir, J. Wiedemann
Journal of Sound and Vibration

(Submitted 16 August 2011, pending response)

The present investigation focuses on simulation of the aeroacoustic resonance of partially covered cavities with a width much larger than their length or depth that represent simplified door and trunk lid gaps. These cavities are under influence of a low Mach number flow with a relatively thick boundary layer. Under certain conditions, flow-induced acoustic resonance can occur. The requirements to simulate the resonance behavior using a Lattice Boltzmann method (LBM) model are investigated. Special focus is put on the effect of simulation spanwise width and inflow conditions.

In order to validate the simulations, experiments have been conducted on simplified geometries. The configuration consists of a partially covered, rectangular cavity geometry 32 x 50 x 250 mm in size, with opening dimensions of 8 x 250 mm. Cavity flow induced acoustic response is measured with microphones at different spanwise locations inside the cavity. Hot-wire measurements are performed to quantify the boundary layer characteristics. Furthermore, high speed time resolved Particle Image velocimetry is used to capture the instantaneous velocity field around the opening geometry.

Flow simulations show that the turbulent fluctuation content of the boundary layer is important to correctly simulate the flow induced resonance response. A minimum simulation spanwise width is needed to show good resemblance with experimental cavity pressure spectra. When a full spanwise width simulation is employed, base mode and higher modes are retrieved.

7.1 Introduction

In automotive applications, the cavity created by the door and trunk lid gaps can exhibit aeroacoustic excitation by the external flow. Door and trunk lid gaps are partially covered cavities that are slender (width much larger than length or depth) and under influence of a low Mach number flow ($M \approx 0.1$) with a relatively thick turbulent boundary layer. Under certain conditions the fluid enclosed in the volume of the cavity can act as an acoustic resonator to an excitation source in the opening region. The current investigation concerns a simplified cavity geometry for evaluation of the aeroacoustic resonance properties. The geometry can be interpreted as a simplified automotive door gap, but the investigation is also relevant for other applications with similar geometrical and flow features.

Excitation can either be due to a feedback mechanism of the perturbed shear layer or due to passive excitation by the pressure fluctuations in the turbulent flow (turbulent rumble) [1]. In case of feedback, the shear layer can roll up into vortices impinging on the downstream edge coherently (a Rossiter mode) [2], similar to the phenomenon of sunroof buffeting [3, 4]. If the excitation frequency is close to a resonance frequency, lock-on can occur and the system can resonate. For partially covered cavities, the resonance mechanism can be of a Helmholtz type, where the mass of air in the cavity is coherently compressed and expanded [5]. Also, for a slender resonator geometry, higher modes are possible that exhibit spanwise variations [6].

Both slenderness (high width compared to opening length $W/L_o >> 1$) and a thick turbulent boundary layer compared to opening length reduce the resonance response of a cavity. Howe's theory [7] indicates that an increased aspect ratio modifies the impedance, thereby reducing resonance. Kooijman et. al. [8] showed that by increasing the boundary layer momentum thickness compared to the opening length, the instability of the opening shear layer is reduced. For open cavities, a turbulent boundary layer reduces the sound production compared to a laminar one [5]. In fact, in door gaps generally only show a passive response to the flow, although there are cases where a resonance lock-on can occur. In case of lock-on, transfer of energy from flow to acoustics is low, the expected ratio of acoustic velocity compared to the free-stream velocity is $u'_{ac}/U_\infty \approx 10^{-2}$ [6]. The tendency for cavities of this type to show only limited and low-amplitude resonance makes it more difficult to simulate the aeroacoustic behavior correctly [9].

Slotted partially covered cavity geometries have been investigated to a lesser extend compared to open ones. The importance of the incoming boundary layer properties is often acknowledged, but the details of the boundary layer are not well documented. Examples of experimental investigations on partially covered cavities are Dequand et. al. [10, 11], Nelson [12, 13], Henderson [14, 15], Ma [16] and Mongeau et.al. [17]. Dequand et. al. [10, 11] investigated the resonance lock-on amplitude of several rectangular (non-slender) Helmholtz resonator geometries under a thin laminar boundary layer flow. Nelson [12, 13] experimentally analyzed a Helmholtz resonator with laser Doppler velocimetry, where a high aspect ratio opening slot was excited by a low Mach grazing turbulent flow of unknown boundary layer shape. In addition, Henderson [14, 15] presented benchmark experimental data of a resonator with a slot and flow of 45 to 60 m/s. The boundary layer detailed properties are only partially documented and due to the limited velocity range, only part of resonance lock-on is observed. Furthermore, there are unexplained spectral peaks in the cavity internal pressure signal. The authors observed modes with spanwise variations that can contribute to additional spectral peaks in the cavity internal pressure signal [6]. Ma et. al. [16] have investigated a slotted Helmholtz resonator using particle image velocimetry (PIV). Mongeau et. al. [17] show experimental results of a 250 mm wide cavity that resembles a door gap, including a seal fixture, where the cavity showed a passive response to the outside flow. In conclusion, for validation of resonance simulations of the currently investigated geometries a more complete experimental dataset would be advantageous.

Numerical simulation results in literature are mostly focussed on open cavity configurations [5], where the resonance or feedback mode is not of a Helmholtz type. Initially, open cavity resonance has been investigated using 2d and 3d Reynolds averaged Navier Stokes (RANS) methods [18, 19, 20]. For low Reynolds numbers, direct numerical simulation (DNS) methods have been used [21, 22, 23]. Recently, more focus has been put on Large Eddy Simulation (LES) [24, 25, 26, 27, 28, 29, 30] or hybrid RANS/LES (DES) methods [31] for open cavities. Partially covered cavities have been investigated less numerically. For example, based on the NASA benchmark geometry [14, 15], several 2d studies have been executed [32, 33, 34], showing variations in obtained excitation frequencies and amplitudes.

For direct evaluation of partially covered cavities, a compressible flow is needed to account for the compressibility of the fluid in the cavity body. A good candidate for compressible aeroacoustic simulation at low Mach number is the Lattice Boltzmann Method (LBM) [35, 36]. LBM uses kinetic theory to simulate compressible flows at low Mach numbers. It has been shown that LBM is capable of propagating acoustic waves as well as fluid flow [37, 38, 39, 40, 41, 42]. LBM is used in a number of aeroacoustic applications [43]. For partially covered cavities, the Lattice Boltzmann method has been applied by Malick et.al. [44] on the Nelson cavity geometry [12, 13]. A large discrepancy between onset velocities of around 40% is observed in LBM simulations, which was attributed to the boundary layer properties. A more extensive experimental dataset is needed in order to provide more insight in the exact influence of the boundary layer properties. The NASA benchmark geometry [14, 15] has been simulated by Wilde using a slender 3D LBM simulation setup [45]. Also recently Premnath et. al. [46] have simulated the benchmark using a Lattice Boltzmann method with an LES setup. The LBM studies reveal excitation frequencies in the experimental range, but with varying amplitude. A validation using a more extensive dataset would reveal the capabilities of LBM to simulate the currently investigated geometries. Also, most mentioned cavity simulations are two-dimensional or concern a three-dimensional slice of limited spanwise width, so that spanwise modes [6] are not retrieved. A full span simulation would reveal the capability of LBM to capture the spanwise modes in simulation and would also reveal the influence of spanwise width on resonance.

The purpose of the present research is to (1) provide a good validation set for LBM numerical simulations of aeroacoustic resonance and (2) to investigate the physical features that need to be incorporated in an LBM aeroacoustics simulation of the currently investigated geometry to reproduce the experimental behavior. This includes the question whether or not an LBM aeroacoustic simulation can reproduce the tonal resonance features of the experiments and depending on what inflow and boundary conditions. An extensive experimental investigation using PIV, hotwire and pressure transducer measurements is conducted by the authors to compare the boundary layer properties and flow structures in the opening. Measurements have been conducted in an open jet wind tunnel. The current work is a continuation of the authors' investigations on cavity modes [6] and an experimental parametric study on the influence of inflow conditions and opening geometry [47]. Compared to previous experiments in literature [14, 15], focus has been put on spanwise variations in pressure [6] and variations in flow conditions [47]. The boundary layer properties are measured in detail to allow improved matching of simulation conditions with experiments to reduce the large discrepancy between onset velocities as observed before in LBM simulations by Mallick et. al. [44]. The ability of a Lattice Boltzmann based model to simulate the cavity problem is investigated. Three dimensional flow acoustic simulations are performed using LBM and are compared with experimental results. Compared to previous work on cavity LBM simulation [45, 46], special attention is put on the effect of inflow conditions and spanwise simulation width up to full span on cavity resonance in order to derive the necessary physics needed to simulate door and trunk lid gap structures. The flow structures in the opening are compared to PIV results.

7.2 Experimental apparatus and procedure

7.2.1 Wind tunnel and model

Experiments are conducted in a low speed open jet wind tunnel at Delft University of Technology. The tunnel has a vertical outflow through a circular opening of 0.6 m in diameter. The tunnel contraction ratio is 250:1. The airflow in the test section

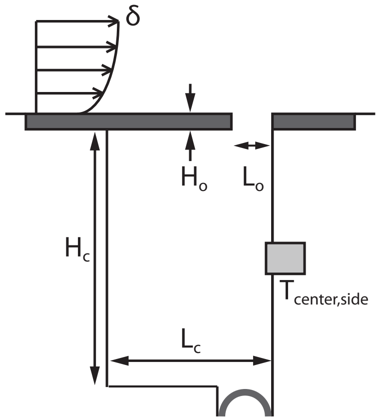

Figure 7.1: Cross sectional view of the cavity

has a turbulence intensity of 0.2 % and the wind tunnel acoustic background noise at 25 m/s is approximately 20 dB.

The experimental geometry consists of a rectangular cavity partially covered by a rigid overhang plate attached at either the upstream or downstream corner of the cavity. The cavity opening is subjected to a flow with a thick (compared to the opening length L_o) boundary layer developed along a flat plate. Figure 7.1 shows the internal dimensions of the cavity. The aspect ratio of the opening is $W/L_o = 31.25$, with a width of $W = 250$ mm. The cavity itself is constructed out of thick-walled aluminum to ensure enough rigidity to prevent fluid-structure resonance effects. As Mongeau [17] indicated, the ratio of internal cavity length to the opening length can be of importance. Therefore in the current investigation, the ratio of opening length and cavity internal length are set to resemble car door gaps more closely than similar configurations of [14, 15]. The cavity neck is designed to have interchangeable parts in order to investigate multiple opening geometries. In the current investigation, it is equipped with sharp edges and an upstream cover lip overhang. The cross-sectional internal dimensions are $L_c \times H_c = 32 \times 50$ mm and the opening dimensions are $L_o \times H_o = 8.0 \times 3.2$ mm. Based on the equation for a Helmholtz resonator $f_H = \frac{c}{2\pi}\sqrt{\frac{S}{VH_o'}}$, the expected base resonance frequency is around 800 Hz and expected velocity of maximum resonance is 25 m/s. Here c is the speed of sound, S the opening surface area, V the cavity volume and H' the modified opening height including end effects.

The model used in the wind tunnel is a cavity embedded in a splitter plate which has an elliptic nose cone. Figure 7.2 shows the setup mounted in the wind tunnel nozzle. The boundary layer develops on the first section of the splitter

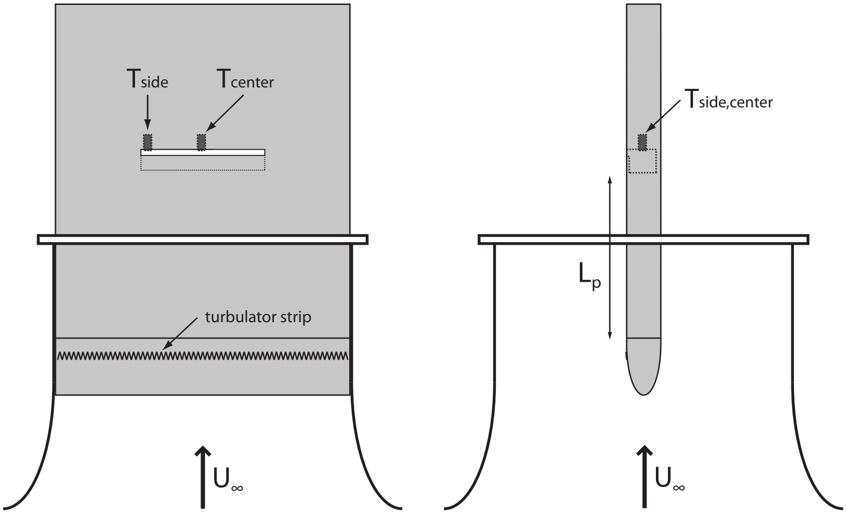

Figure 7.2: Front and side views of splitter plate with cavity mounted in wind tunnel nozzle. Cavity internal microphone T_C, T_E locations indicated by arrows.

plate, upstream of the cavity. The boundary layer is controlled in a precise and reproducible way by adjusting the length of the upstream section of the flat plate L_p. In the setup used for this study, it is chosen as $L_p = 0.2$ m. A zigzag type turbulator strip of 1 mm height is located 10 cm downstream of the leading edge to trigger the transition of the laminar boundary layer into a turbulent one. The maximum spanwise width of the cavity is smaller than the 0.6 m width of the splitter plate itself to ensure constant flow properties along the span.

7.2.2 Measurement Equipment

The boundary layer characteristics are measured with a constant temperature hot-wire probe in absence of a cavity. Flow runs with open cavity have been performed to measure the flow induced sound pressure levels inside the cavity. The velocity is increased incrementally from 12 m/s in steps of 2 m/s, up to the wind tunnel limit of approximately 46 m/s.

The cavity internal sound pressure level is recorded using two Brüel & Kjaer 1/2″ condensator microphones with a dynamic range of 14-142 dB. These are located at different spanwise locations (center and side) inside the cavity, as indicated in figure 7.1. The microphones recorded the pressure fluctuations with a sampling rate of 4000 Hz. The diagnosis-system SQlab in combination with the software ArtemiS, both products of HEAD acoustics, were used for the measurements.

In order to evaluate the flow in the opening region, high speed, time resolved Particle Image Velocimetry (PIV) has been used. The PIV measurements are also used to capture the lower boundary layer characteristics in combination with hot-wire results. Illumination over an area of 25 by 16 mm is provided by a Quantronics Darwin-Duo 527 Nd:YLF laser. The field of view captures the cavity opening and the outer flow boundary layer up to 8 mm in height. The light sheet is positioned streamwise and perpendicular to the plate, with spanwise location 80 mm from the opening edge. A Photron Fastcam SA1.1 camera (1,024 x 1,024 pixels) is placed at a 90 degree angle with the illumination, and captures 1024 x 512 images. The illumination and recording devices are synchronized and controlled by a LaVision programmable timing unit (PTU v9). Each measurement consists of 1000 image pairs at a recording frequency of 6000 Hz, which is sufficient to capture the temporal behavior of the flow (at approximately eight samples per resonance cycle). The double pulse interval is varied between 8 and 15 microseconds, depending on the velocity. The chosen magnification yields a typical digital resolution of 40 pixels/mm. The images were analyzed with the LaVision Davis 7.3 software, using a multi-step cross-correlation with a final interrogation window size of 16 by 16 pixels (0.4 by 0.4 mm^2) with 75% overlap.

7.2.3 Experimental cavity flow induced response

The cavity flow induced resonance is investigated by measuring the internal pressure response. The results for the upstream overhang with sharp edges are presented. This configuration shows typical resonance properties and resembles previously investigated geometries most closely [14, 15].

The flow velocity is increased incrementally. The internal sound pressure levels of these velocity sweeps are gathered in spectrograms and given in figure 7.3 for both microphone locations (locations as indicated in figure 7.2). The frequency of the excitation is shown at the vertical axis and the free stream velocity on the horizontal one. The pressure amplitude of the excitation is indicated in dB, with standard $2 \cdot 10^{-5}$ Pa reference pressure. The velocity sweep in the figure shows several resonating modes with increasing mode frequencies. The first resonance mode is visible at both probe locations whereas the second mode is only visible for the side probe. The observed higher mode frequencies correspond to coupling of Helmholtz resonance with spanwise modes [6] according to:

$$f_n = \frac{c}{2\pi}\sqrt{\frac{S}{VH_o'} + \beta\left(\frac{\pi\,(n-1)}{W}\right)^2}, \tag{7.1}$$

Here V is the cavity volume, S is the cavity neck surface area and H_o' is the corrected vertical length of the cavity neck. The relation between the actual vertical cavity neck height H_o and H_o' is $H_o' = H_o + h$, where h is an end effect correction factor to account for the added resonating mass above and below the opening. β is of order 1. The equation is a modified Helmholtz resonance model, accounting for variations due to spanwise modes. Note that this equation can be interpreted as the interaction between spanwise standing waves and Helmholtz resonance or as individual sections of the cavity acting as separate Helmholtz resonators that are coupled. The first $n = 1$ mode has constant properties along

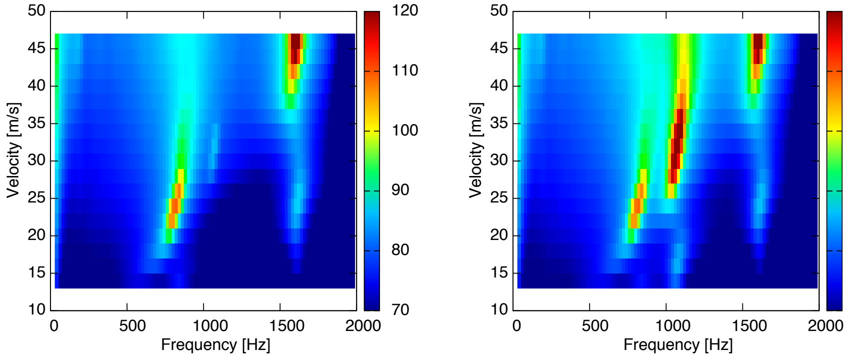

(a) T_C, Center location

(b) T_E, Edge location

Figure 7.3: Spectrograms of the three internal pressure probes, colored by sound pressure level [dB].

the span and corresponds to the Helmholtz mode. For the $n = 2$ mode, the opposite ends of the cavity are in anti-phase and a pressure node is present in the spanwise center, which is in agreement with figure 7.3.

From figure 7.3 it is found that all the center points of the excitation modes show a linear relation between frequency and velocity. The corresponding Strouhal number $Sr = \frac{fL_o}{U_\infty}$ is approximately 0.3, indicating that all modes are hydrodynamically excited by the first stage Rossiter mode [2]. No excitation of the second stage Rossiter mode ($Sr \approx 0.7$) is present, although low amplitude onsets of resonance for this Strouhal number can be observed in the upper left part of the figures by low amplitude horizontal excitation lines.

7.3 Lattice Boltzmann Method

Numerical simulation results of flow and acoustics are obtained using the Lattice Boltzmann Method (LBM) [48]. LBM is an alternative numerical method to traditional partial differential equation based computational fluid dynamics for simulating complex fluid flows. Unlike conventional methods based on macroscopic continuum equations, the LBM starts from mesoscopic kinetic equations, i.e. the Boltzmann equation, to determine macroscopic fluid dynamics. The commercial LBM based package PowerFLOW is used.

Kinetic equations are solved on a cartesian mesh (the lattice) by explicit timestepping and collision modeling. The lattice Boltzmann equation has the following form:

$$f_i\left(\mathbf{x} + \mathbf{c_i}\Delta t, t + \Delta t\right) - f_i\left(\mathbf{x}, t\right) = C_i\left(\mathbf{x}, t\right), \tag{7.2}$$

where f_i is the particle distribution function moving in the ith direction, according to a finite set of the discrete velocity vectors $\{\mathbf{c_i} : i = 0, ..., N\}$. $\mathbf{c_i}\Delta t$ and Δt are space and time increments respectively. The collision term on the right hand side of Eq. (7.2) adopts the simplest and also the most popular form known as the Bhatnagar-Cross-Krook (BGK) form [49]:

$$C_i(\mathbf{x}, t) = -\frac{\Delta t}{\tau}\left[f_i(\mathbf{x}, t) - f_i^{\mathrm{eq}}(\mathbf{x}, t)\right] \tag{7.3}$$

Here τ is the relaxation time parameter, and f_i^{eq} is the local equilibrium distribution function according to the BGK approximation [49], which depends on local fluid dynamic properties. The basic fluid dynamic quantities, such as fluid density ρ and velocity $\mathbf{u}$, are obtained through moment summations over the velocity vectors; i.e.

$$\rho(\mathbf{x}, t) = \sum_i f_i(\mathbf{x}, t), \ \rho\mathbf{u}(\mathbf{x}, t) = \sum_i \mathbf{c_i} f_i.(\mathbf{x}, t) \tag{7.4}$$

In the low frequency and long-wave-length limit, for a suitable choice of the set of discrete velocity vectors, one can recover the compressible Navier-Stokes equations through the Chapman-Enskog expansion [48]. The resulting equation of state obeys the ideal gas law, $p = \rho RT$. The kinematic viscosity of the fluid is related to the relaxation time parameter, τ , by [37]:

$$\tau = \frac{\nu}{RT} + \frac{\Delta t}{2}. \tag{7.5}$$

The combination of Eq. (7.2) to (7.5) forms the LBM scheme.

By recovering the compressible Navier-Stokes equations, including an ideal gas equation of state, LBM also inherently recovers acoustics. Some fundamental aeroacoustic capabilities of the scheme have been studied before, such as wave propagation and compressible behavior [37, 38, 39, 40, 41, 42, 50, 51, 35, 36]. In these cases the code has proven itself capable of correctly simulating these acoustics related problems. Examples of the use of the Lattice Boltzmann scheme in acoustics are simulation of radiation from waveguides, [52], acoustic pulses in flows and duct aeroacoustics [53], landing gear noise [54, 55], underbody and wind noise [56, 57], HVAC noise [58, 59] and sunroof buffeting [3, 4]. Slotted cavity resonance has been investigated by several authors [44, 45, 46].

The Lattice Boltzmann equation is solved on a grid composed of cubic volumetric elements (the Lattice). Variable resolution is allowed, where the grid size changes by a factor of two for adjacent resolution regions.

Due to the explicit timestepping characteristics of the scheme, the timestep size is increased with cell size in factors of two as well. This will cause the larger cells to not be evaluated for each timestep of the smallest cell and gives rise to the notion of timestep equivalent number of cells (number of cells scaled to operation at the shortest timestep) in addition to the total number of cells. The timestep equivalent number of cells is a better indicator for the amount of computational work than the total number of cells.

The kinematic viscosity of the fluid is related to the relaxation time parameter τ [43]. A viscosity model is implemented through the relaxation time τ to locally adjust the numerical viscosity of the scheme. In the approach a $k-\epsilon$ turbulence model is incorporated into the LBM scheme. The original two equation Renormalization Group (RNG) is modified to incorporate a swirl based correction. This correction reduces the modeled turbulence in presence of large vortical structures and is therefore able to capture these directly. This scheme is used to simulate a flat plate boundary layer including turbulator strip. For the cavity simulations, an Implicit Large Eddy Simulation model (ILES) is used, where the sub-grid scale viscosity is modeled through the numerical dissipation of the scheme. This allows for an effective low viscosity model needed to simulate the flow with small length scales around the resonator opening.

For high-Reynolds-number turbulent flows, fully resolving the near wall region is computationally too expensive. Therefore, a turbulent wall model is used to provide approximate boundary conditions. In the current study, the following wall- shear stress model based on the extension of the generalized law of wall is used [56, 37]:

$$u^+ = f\left(\frac{y^+}{A}\right) = \frac{1}{\kappa}\ln\left(\frac{y^+}{A}\right) + B, \tag{7.6}$$

with

$$A = 1 + f\left(\frac{\mathrm{d}p}{\mathrm{d}x}\right). \tag{7.7}$$

This equation is iteratively solved to provide an estimated wall-shear stress for wall boundary conditions in the LBM calculation. A slip algorithm [37] (a generalization of bounce-back and specular reflection process) is then used for the boundary process.

7.4 Flat plate boundary layer simulations

First, a flat plate boundary is simulated to investigate the capability of the LBM code to simulate the turbulent flow structures with the level of detail needed for the current application. The time-dependent flow structures obtained from this simulation are used as inlet conditions for cavity simulations. The boundary layer properties are compared to our PIV and hotwire experimental results.

7.4.1 Simulation setup

The simulation setup consists of a flat plate with a turbulator strip geometry of which a section is shown in figure 7.4. The boundary layer properties are measured 0.2 m after the turbulator, in the same way as in experiments. The turbulator strip is 1 mm thick with 10 mm streamwise length and 9 mm spanwise repetition of the teeth. The highest resolution region around the turbulator has 50 mm streamwise length. The wall upstream of the turbulator is set as a frictionless slip boundary. The full simulation width is set to $W_{sim} = 288$ mm in order to use the boundary layer time-dependent pressure and velocities as inlet conditions for full span cavity simulations of the same span. A resolution study has been performed on a reduced domain of 80 mm spanwise width, as depicted in figure 7.4.

Based on the resolution study given in section 7.4.2 below, the final 288 mm span simulation linear resolution in the lower region of the boundary layer is 4 cells/mm and around the strip it is 8 cells/mm. The average $y^+ \approx 15$, confirming the need for the implemented wall model. The total number of cells is 105 million and the timestep equivalent number of cells is 56.8 million. Due to the fact that in the flat plate simulation acoustics are not of interest, the simulation is run at a larger Mach nr $M \approx 0.3$ to allow larger timesteps. The physical run time is 0.3 seconds, corresponding to 452 thousand timesteps.

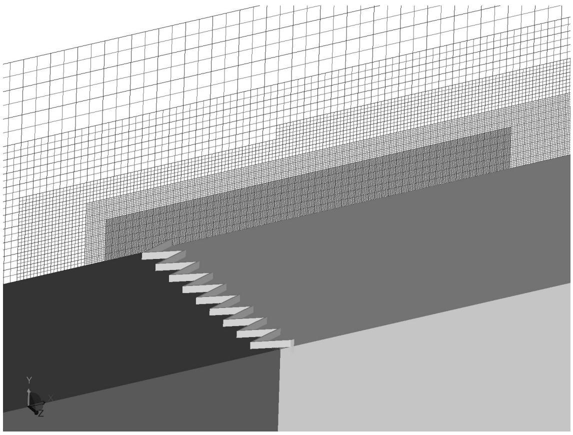

Figure 7.4: Flat plate with turbulator simulation setup, 80 mm wide section view of turbulator strip and resolution regions. Dark grey wall upstream of turbulator is set as frictionless. Highest resolution region has 50 mm streamwise length.

7.4.2 Resolution study and comparison with experiment

A resolution study has been performed on a plate of 80 mm spanwise width and 24 m/s flow speed. Both the resolution in the boundary layer (R_{bl}, expressed in cells/mm) and the resolution around the turbulator strip (R_{t}) are investigated. Figure 7.5 illustrates the influence of the resolution on the boundary layer by showing the mean and r.m.s. profiles of the simulation compared to experiments for 4 resolution settings, 0.2 m past the turbulator strip. Combinations of $R_{\mathrm{t}} = 4$ and 8 cells/mm and $R_{\mathrm{bl}} = 2$ and 4 cells/mm have been simulated. The experimental boundary layer results using hot-wire and PIV have been added. The resolution around the turbulator strip influences the fluctuation content and to a lesser extend the mean boundary layer profile as well. A resolution setting of of $R_{\mathrm{t}} = 8$, $R_{\mathrm{bl}} = 4$

cells/mm is sufficient to resolve the boundary layer turbulent fluctuations and is used in the full-width flat plate simulations.

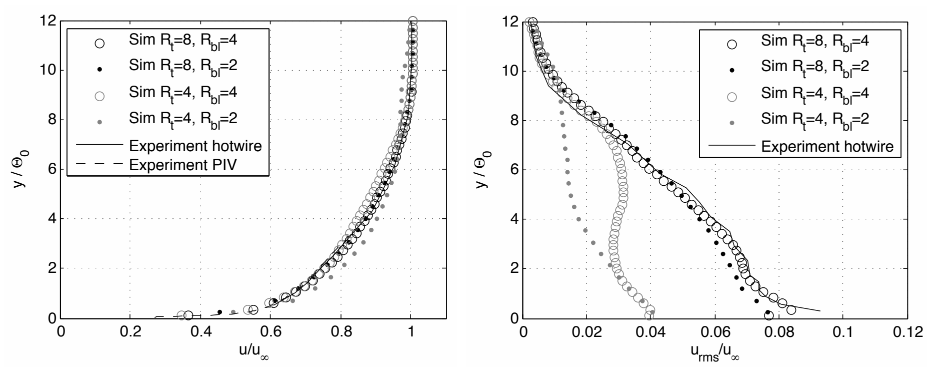

(a) mean

(b) r.m.s.

Figure 7.5: Plate simulation boundary layer mean and r.m.s. velocity profiles, 24 m/s free stream velocity. PIV and hotwire experimental results included.

Final resolution boundary layer properties are given in figure 7.6. Figure 7.6(a) shows the streamwise velocity spectrum at $y/\theta = 2$ for the $R_{\mathrm{t}} = 8$, $R_{\mathrm{bl}} = 4$, $W = 288$ mm simulation. Fluctuations at $y/\theta = 2$ are comparable to hotwire experimental fluctuations until a cutoff around 1.5 kHz, which is above the cavity resonance frequency of interest of around 800 Hz. Figure 7.6(b) shows boundary layer mean properties in logarithmic scale. Both experiment and simulation reveal a fully developed turbulent profile.

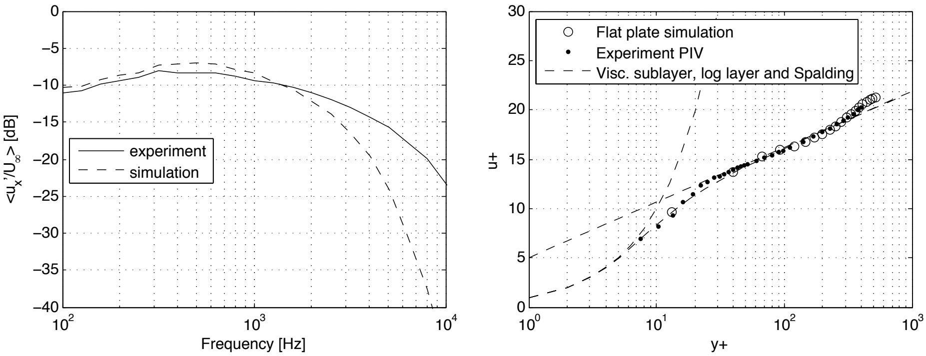

(a) Spectrum at $y/\theta = 2$ (b) Simulation boundary layer in log scale

Figure 7.6: Simulation boundary layer details. 24 m/s, experimental results included. In the right figure the log layer, viscous sublayer and Spaldings law of the wall are depicted [60].

Two integral properties are evaluated from the simulation at 0.2m distance [60], giving a shape factor of $H = 1.36$: the displacement thickness $\delta^* = 1.16$ mm, the momentum thickness $\theta = 0.85$ mm. The shape factor corresponds to a value for a turbulent flat plate boundary layer[60]. The height at 99% of the mean flow is $\delta_{99} = 7.6$ mm.

The turbulent vortices in the boundary layer are visualized by isosurfaces of the λ_2 criterion for vortex detection in figure 7.7, where λ_2 is the second largest Eigenvalue of $S^2 + \Omega^2$, with S the symmetric deformation tensor and Ω the anti-symmetric spin tensor [61]. One can see that the ordered wake structures of the turbulator strip decay into turbulent vortices that are convected downstream. Development of turbulent hairpin vortex structures can be observed in the figure.

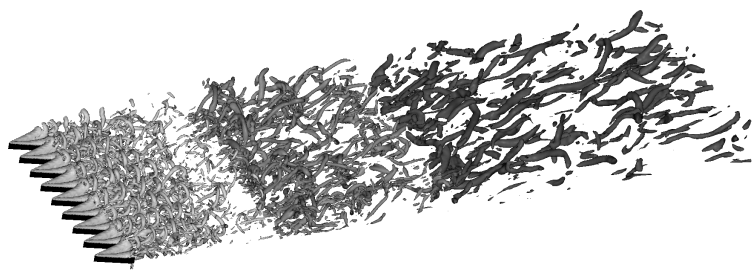

Figure 7.7: Iso-surfaces of λ_2 criterion for part of the strip simulation. Iso-surface adjusted for 3 regions depicted in greyscale, from left to right $\lambda_2 = -0.35, -0.04, -0.012$

7.5 Cavity simulations

Three dimensional cavity simulations have been performed, where the simulated flat plate boundary layer is used as an inlet condition. In order to investigate the effect of turbulent fluctuations, both simulations with and without the direct turbulent boundary layer fluctuations (only the mean flow as an inlet condition) have been performed. In literature [45, 46] it is common practice to simulate only a limited spanwise part of the slender geometry. However it is not clear what is the minimum width needed to correctly simulate the aeroacoustic response. Initial simulations have been performed using a reduced spanwise width and cyclic side boundary conditions. The cavity opening width has been varied between $W = 4L_o$ (32 mm), $W = 8L_o$ (64 mm) and the full cavity width of $W = 250$ mm to investigate the effect of simulation domain width on the cavity response characteristics.

7.5.1 Cavity simulation setup

A view of the cavity simulation setup including resolution regions is given in figure 7.8. The cavity dimensions correspond to the experimental dimensions given in figure 7.1. A resolution study has been performed for $W = 4L_o$ (32 mm) with inlet fluctuations, from which a minimum needed opening resolution of 8 cells/mm or 64 streamwise cells in the opening is found. For the current simulations, the opening resolution is 8 cells/mm and the boundary layer has a resolution of 4 cells/mm. The inlet for the boundary layer is located 30 mm upstream, as seen in figure 7.8. To minimize acoustic reflections, the boundary layer inlet plane is 10 mm high and the upstream, downstream and vertical height of the simulation domain is 2 m. A buffer layer with high viscosity is used in the acoustic far-field. A frictionless wall and free-stream conditions are imposed upstream above the boundary layer inlet.

Both simulations with and without direct inlet turbulent boundary layer fluctuations are performed. Flat plate simulation measurements are taken at a streamwise location such that the boundary layer conditions at 0.2 m streamwise length are matched around the cavity opening region. For simulations with inlet fluctuations, the time-dependent flow properties (all 3 velocity components u, v, w, density ρ and pressure p) of the flat plate simulation boundary layer are recorded at 10 kHz and seeded into the inlet. For simulations without inlet fluctuations, only the mean velocity profile is prescribed at the inlet.

For simulations with a reduced spanwise width, the cavity and flow domain width is varied between $W = 4L_o$ (32 mm) and $W = 8L_o$ (64 mm), which gives an opening aspect ratio $AR = W/L_o$ equal to 4 and 8. Full span simulations include the full cavity width of $W = 250$ mm. The full span simulation domain width is set larger than the cavity width, $W_{sim} = 288mm > W$, in order to capture any fluid dynamic effects of the opening ends. The total number of cells is 45.8 million and the timestep equivalent number of cells is 17.6 million. Due to the fact that in the cavity simulation acoustics are of interest, the simulation is run at the experimentally matched Mach numbers based on the simulation flow velocity and

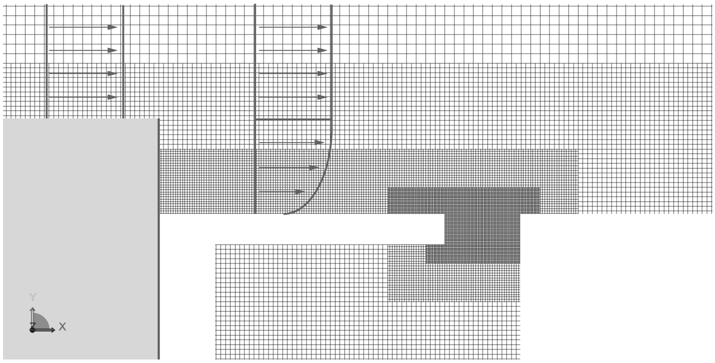

Figure 7.8: Side view of streamwise plane through simulation. Flow is from left to right. The variable resolution regions are shown, with the highest resolution of 8 cells/mm at cavity opening edges. Boundary layer profile is prescribed at dark grey inlet, light grey region is a frictionless wall. Approximate velocity profiles are sketched.

a sound speed of $c = 340$ m/s. The physical run time is 0.3 sec, corresponding to 1.45 million timesteps.

7.5.2 Effect of simulation width and boundary layer turbulent fluctuations

For reduced span setups, several flow velocities in the range of 20 - 30 m/s have been simulated. This corresponds to a Reynolds number range of approximately $10500 < Re < 16000$, based on the streamwise opening length L_o. Figure 7.9 shows the pressure time series of the cavity internal probe of the resonating flow velocity of 23 m/s for both the simulations with and without inlet turbulent fluctuations. Experimental results (center microphone) for 24 m/s are included for comparison. The steady inlet simulation of figure 7.9(a) shows a higher resonance amplitude compared to experiments. The inclusion of boundary layer turbulence reduces resonance amplitude. The $W = 8L_o$ simulation resonance amplitude of figure 7.9(c)is resembling the experimental results of figure 7.9(d). There is more resonance intermittency in the $W = 4L_o$ simulation time signal of figure 7.9(b) compared to the experiment. Pressure spectra are given in figure 7.10. Please note the 2000 Hz experimental cutoff due to the chosen experimental measurement frequency. The intermittency in the $W = 4L_o$ simulation time signal is manifesting itself in an increased broadband component in the spectra compared to experiment.

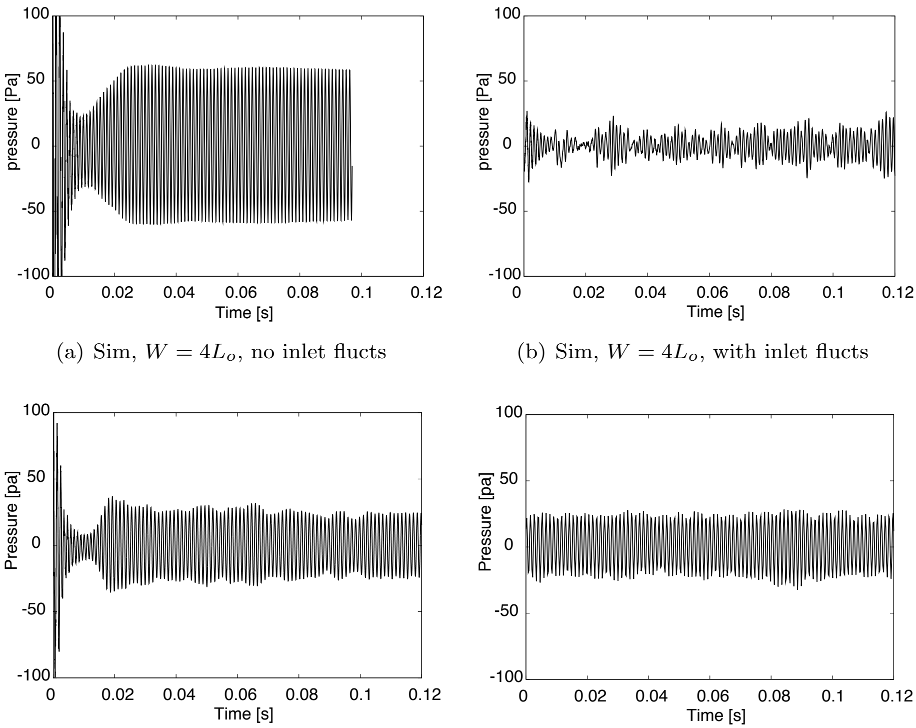

(a) Sim, $W = 4L_o$, no inlet flucts

(b) Sim, $W = 4L_o$, with inlet flucts

(c) Sim, $W = 8L_o$, with inlet flucts

(d) Experiment

Figure 7.9: Pressure time series of cavity internal pressure for experiment and simulations, 24 m/s flow speed.

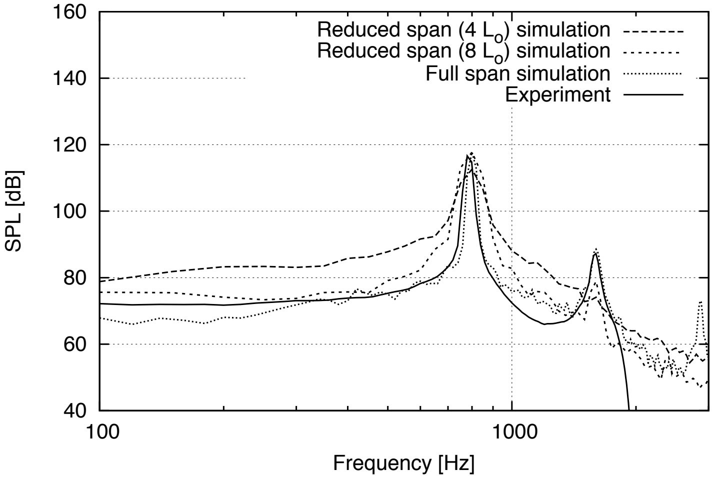

Figure 7.10: Cavity internal pressure spectrum for small span simulations, 23 m/s flow speed (22 m/s for full span simulation). Experimental results (center microphone) at 24 m/s included.

7.5.3 Results of full span simulations

Full span simulations have been performed for 3 free-stream velocities, 22, 25 and 28 m/s and include boundary layer fluctuations prescribed at the inlet. The spectra for the center and side internal cavity microphones are given in figure 7.11. Included are experimental results for the same mode. Please note that due to the limited experimental velocity resolution of 2 m/s, the comparison is limited to only the closest measured mode.

The simulations match all spectral peaks and the broadband well. The onset velocities for the observed modes are slightly shifted compared to experiments. The base mode is excited at 22 m/s (experiment 24 m/s), the second mode is excited at 28 m/s (experiment 30 m/s). The intermittent mode is matched best, at 25 m/s in simulation compared to 26 m/s in experiment. A larger discrepancy between onset velocities of around 40% as observed before in LBM simulations of Helmholtz resonators in literature by Mallick et. al. [44] was attributed to the boundary layer properties. The reduction in discrepancy between current research and Mallick et. al. can be attributed to a better matching of the boundary layer properties in the current research. The remaining discrepancy is currently not fully explained and subject for future investigation.

The overprediction in amplitude for the higher mode can be attributed to differences in cavity structural compliance between experiment and simulation. In the LBM simulations, all walls are infinitely stiff, whereas the experiments included a seal in the lower body of the cavity. The resonance lock-on amplitude is of low energy compared to the mean flow energy and therefore the amplitude of excitation is very sensitive to changes in wall compliance and damping [9, 47].

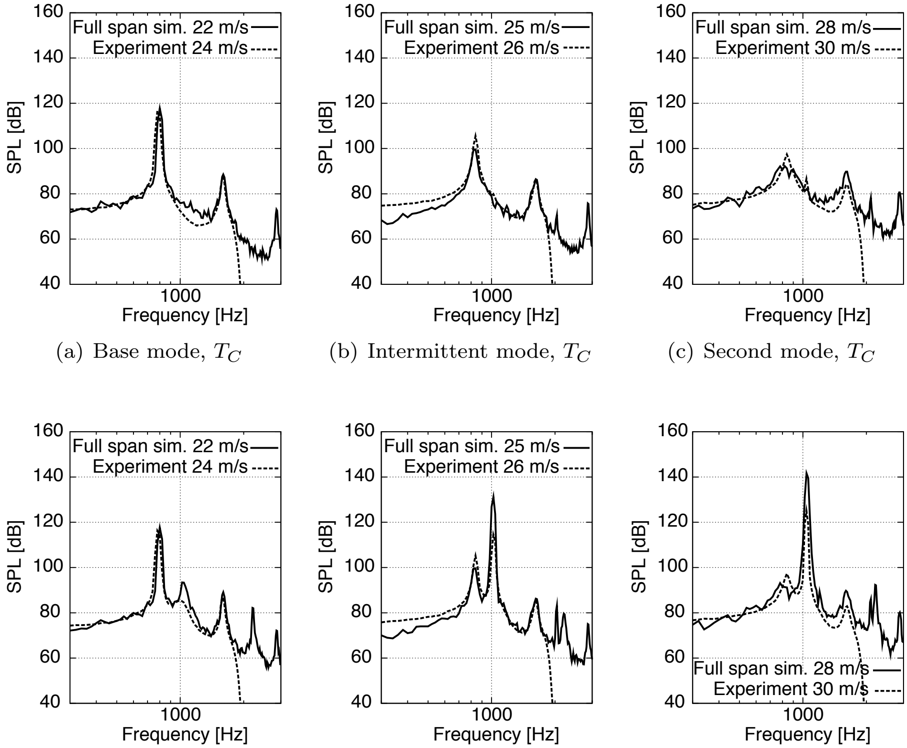

(a) Base mode, T_C (b) Intermittent mode, T_C (c) Second mode, T_C

(d) Base mode, T_E (e) Intermittent mode, T_E (f) Second mode, T_E

Figure 7.11: Full span simulations compared to experiment, cavity internal microphone sound pressure levels. Top figure show center microphone (T_C) response, bottom figures show edge microphone (T_E) results.

7.5.4 Flow visualization

The resulting velocity and vorticity field from LBM simulations is compared to PIV data. Full span simulation results at 22 m/s are used in comparison with 24 m/s experimental results for the base resonance mode. Mean and time-dependent flow properties are compared. Furthermore the effect of spanwise width is investigated for the simulation base mode at 24 m/s and second mode at 30 m/s.

Figure 7.12 shows full span simulation spanwise vorticity ω_z around the opening of the cavity for both simulation and experiment. A time-resolved snapshot and a phase averaged representation of the flow during maximum cavity inflow is presented. Phase averaging is based on the cavity internal pressure. The color range for the snapshots is $\omega_z L_o/U_\infty$ = -1.3 to 6.5 and the phase averaged color range $\omega_z L_o/U_\infty$ = -1.7 to 8.5. Please note that due to reflections the vorticity very close to the upstream wall ($h < \delta^*/4$) is not fully captured in PIV.

The time-resolved visualizations reveal the coherent fluctuations in the incoming boundary layer and their interactions with the separated shear layer on the cavity opening. The turbulent structures interact strongly with the cavity shear layer. The smallest simulation structures are larger than the smallest structures observed by PIV. This was expected based on the boundary layer velocity frequency cutoff of 1.5 kHz.

The position and shape of the shear layer can be identified more clearly in phase-averaged representation than in the snapshot representation. CFD and PIV show similar phase averaged behavior. The shear layer given in figure 7.12 shows both shear flapping motion (first half of the opening) and limited vortex roll up (second half of the opening). The upstream part of the shear layer is stable and shows limited motion. The shed vortices are partly transported into the cavity due to the interaction with the downstream edge. The phase averaged shear layer pattern is corresponding to observations by [16]. The influence of the interaction with turbulent fluctuations in the boundary layer manifests in a more diffuse shear layer compared to the instantaneous velocity fields.

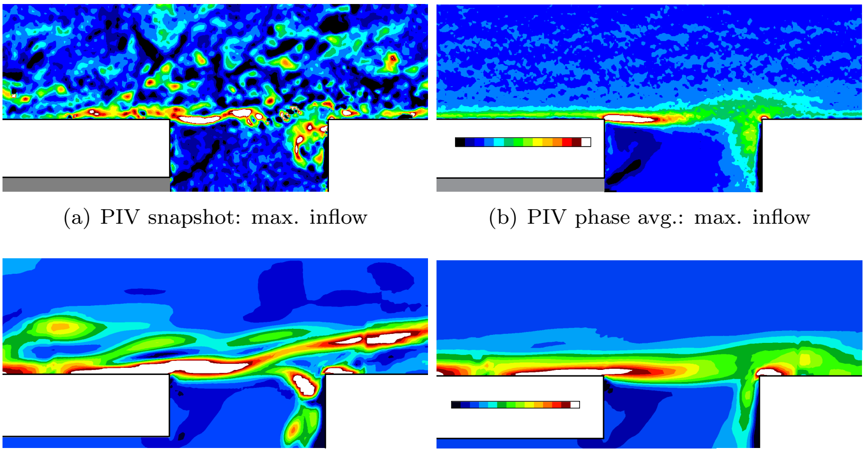

(a) PIV snapshot: max. inflow

(b) PIV phase avg.: max. inflow

(c) Simulation snapshot: max. inflow

(d) Simulation phase avg.: max. inflow

Figure 7.12: Time instances and phase averaged spanwise vorticity for of PIV experiments (top) and CFD simulations (bottom). Time instance color range $\omega_z L_o/U_\infty$ = -1.3 to 6.5. Phase averaged color range $\omega_z L_o/U_\infty$ = -1.7 to 8.5.

The mean flow inside the cavity opening is visualized and compared to PIV data in figure 7.13. This is done for both the standard cavity setup with an upstream cover lip overhang and a reversed cavity with a downsteam cover lip overhang [47]. The simulation with reversed cavity is conducted with a reduced spanwise width of $W = 4L_o$. The modification of the cover lip overhang location drastically alters the flow in the resonator opening. This influences the resonance behavior of the cavity [47]. The current LBM simulations are able to capture this difference in flow patterns between opening geometries.

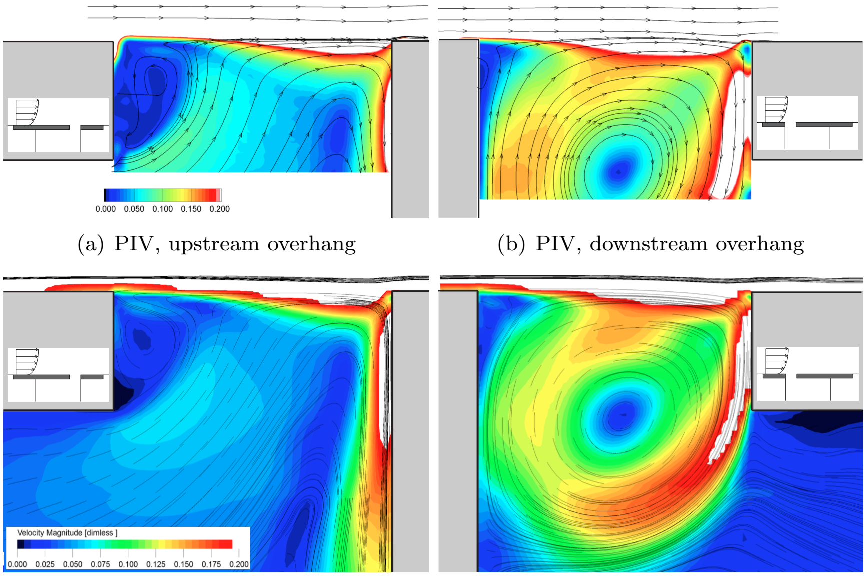

(a) PIV, upstream overhang (b) PIV, downstream overhang

(c) Simulation, upstream overhang (d) Simulation, downstream overhang

Figure 7.13: Velocity magnitude comparison of cavity opening driven flow with experiment, range 0.0 - 0.2 U_∞. The CFD downstream overhang simulation has a reduced spanwise width of $W = 4L_o$.

Figure 7.14 shows a three-dimensional snapshot of the shear layer in the cavity opening for the base mode excitation at 24 m/s. Shown are iso-surfaces of λ_2 vortex tracking parameter colored by spanwise vorticity in the range $-\omega_z L_o/U_\infty =$ 0.0 to 0.3. In this representation, the shear layer roll-up halfway across the streamwise opening length is visible in red. In general the shear layer shows coherent shedding across the entire span, but small variations are present. These variations have a spanwise coherence length that is much shorter than the spanwise width of the opening, but larger than the boundary layer momentum thickness θ. These reduce the amplitude of the base resonance mode compared to an unperturbed shear layer behavior. The influence of small scale spanwise variations in the shear layer was also evident from reduced span simulations depicted in figure 7.9. The fact that the distortion of the shear layer has a length scale larger than the boundary layer coherence length confirms the need for a simulation domain with an extended spanwise width beyond $W = 4L_o$. The turbulent structures influence the resonance behavior in two ways. First of all, the structures directly perturb the cavity, enabling resonance onset. Second, they also break up the shear layer spanwise coherence, thereby reducing the resonance amplitude.

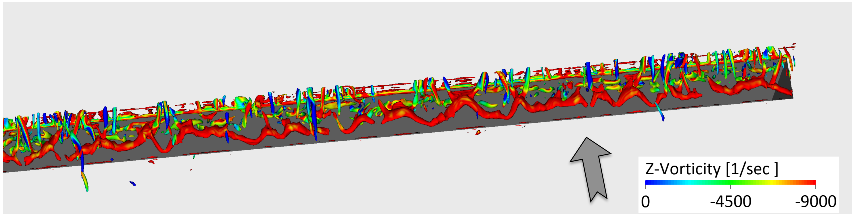

Figure 7.14: λ_2 iso-surfaces colored by spanwise vorticity for base mode simulation. Flow direction is indicated by arrow.

Figure 7.15 shows a snapshot of the shear layer in the cavity opening for the second mode excitation at 30 m/s. Again, shown are iso-surfaces of λ_2 vortex tracking parameter colored by spanwise vorticity in the range $-\omega_z L_o/U_\infty = 0.0$ to 0.3. One can clearly see the half a cycle phase difference between the near and far opening section in the figure. The near section in the figure exhibits a shear layer vortex halfway across the opening length (depicted in red), whereas the far section shows development of a vortex at the upstream opening corner.

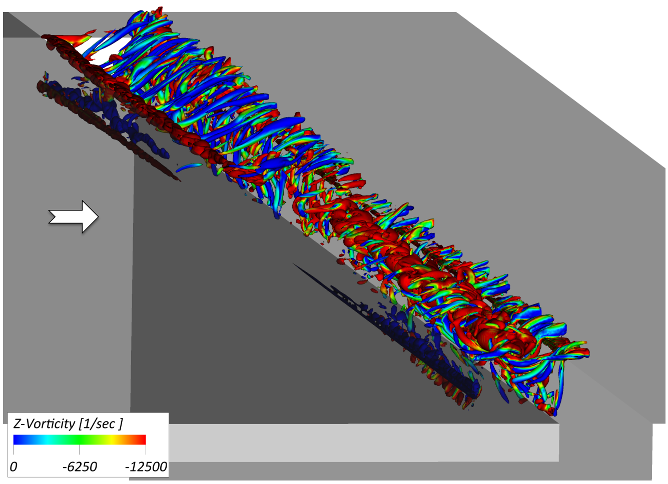

Figure 7.15: External view of λ_2 iso-surfaces colored by spanwise vorticity for second mode (first mode with spanwise variations) simulation. Flow direction is indicated by arrow and the upstream cover lip is depicted transparently.

7.6 Conclusions

A numerical study on simplified door gap geometries has been conducted and compared to experimental results. The numerical investigation is performed using a Lattice Boltzmann Method based code. A flat plate simulation with zigzag type turbulator strip has been implemented to create resolved turbulent boundary layer fluctuations. The mean, r.m.s. profiles and velocity spectra resemble experimental hotwire and PIV results well.

A cavity geometry with an upstream edge overhang and sharp edges is simulated using the Lattice Boltzmann method, where the flat plate boundary layer results are used as inlet conditions. Both reduced and full span setups are simulated. Also simulations including and excluding direct turbulent boundary layer fluctuations are performed to investigate the influence of direct fluctuations on resonance.

Simulations with steady inflow conditions show an over-prediction of resonance amplitude. The boundary layer fluctuations are important to obtain the correct resonance response. Simulations with direct turbulent fluctuations introduced at the inlet show resonance amplitudes that match experiment.

In case of reduced span simulations, lowering the spanwise width to $W = 4L_o$ increases cavity resonance intermittency in the time domain and broadening of the cavity pressure spectrum. This effect is removed by increasing the spanwise width to $W = 8L_o$. Flow visualizations show a shear layer spanwise coherence which is larger than the boundary layer momentum thickness θ, which confirms the need for a sufficient spanwise simulation width.

Full span simulations match the excitation spectrum well for the investigated base mode, first higher mode and a transition mode. The higher mode resonance amplitude is over-predicted, which can be accounted for by the lack of wall compliance of the simulations compared to experiment.

The flow simulations indicate that LBM in the current setup is able to simulate door gap cavity resonance behavior. Large spanwise widths and included boundary layer direct turbulent fluctuations are needed to achieve this.

Acknowledgments

We would like to thank Prof. Hirschberg from Eindhoven University of Technology for the helpful advice on cavity acoustics and advice on design of the experimental setup. From Exa Corp. we would like to thank Dr. David Freed, Dr. Franck Pèrot and Dr. Bernd Crouse for their support and for providing the necessary software. At the aerodynamics department of Delft University we would like to thank Prof. Fulvio Scarano for his experimental advice.

Bibliography

[1] Elder, S. A., Farabee, T. M., and DeMetz, F. C., “Mechanisms of Flow-excited

Cavity Tones at Low Mach Number," *Journal of the Acoustical Society of America*, Vol. 72, No. 2, 1982, pp. 532–549.

[2] Rossiter, J. E., *Wind-tunnel experiments on the flow over rectangular cavities at subsonic and transonic speeds*, London, H.M.S.O., 1st ed., 1967, pp. 1-32.

[3] Crouse, B., Senthooran, S., Balasubramanian, G., Freed, D. M., and Karbon, K., "Computational Aeroacoustics Investigation of Automobile Sunroof Buffeting," *SAE Technical Paper*, 2007-01-2403, 2007, doi:10.4271/2007-01-2403.

[4] Crouse, B., Balasubramanian, G., Senthooran, S., and Freed, D. M., "Investigation of gap deflector efficiency for reduction of sunroof buffeting," *SAE Technical Paper*, 2009-01-2233, 2009, doi:10.4271/2009-01-2233.

[5] Gloerfelt, X., "Cavity noise," `http://sin-web.paris.ensam.fr/squelettes/ref_biblio/Gloerfelt_VKI_2009a.pdf` (date last viewed 04/25/12), 2009.

[6] de Jong, A. T. and Bijl, H., "Investigation of higher spanwise Helmholtz resonance modes in slender covered cavities," *Journal of the Acoustical Society of America*, Vol. 128, No. 4, 2010, pp. 1668–1678.

[7] Howe, M. S., "Low Strouhal number instabilities of flow over apertures and wall cavities," *Journal of the Acoustical Society of America*, Vol. 102, No. 2, 1997, pp. 772–780.

[8] Kooijman, G., Hirschberg, A., and Golliard, J., "Acoustical response of orifices under grazing flow: Effect of boundary layer profile and geometry," *Journal of Sound and Vibration*, Vol. 315, 2008, pp. 849–874.

[9] Nakiboğlu, G., Belfroid, S. P., Willems, J. F., and Hirschberg, A., "Whistling behavior of periodic systems: Corrugated pipes and multiple side branch system," *International Journal of Mechanical Sciences*, Vol. 52, No. 11, 2010, pp. 1458 – 1470.

[10] Dequand, S., Luo, X., Willems, J., and Hirschberg, A., "Helmholtz-Like Resonator Self-Sustained Oscillations, Part 1: Acoustical Measurements and Analytical Models," *AIAA journal*, Vol. 41, No. 3, March 2003, pp. 408–415.

[11] Dequand, S., Hulshoff, S., Kuijk van, H., Willems, J., and Hirschberg, A., "Helmholtz-Like Resonator Self-Sustained Oscillations, Part 2: Detailed Flow Measurements and Numerical Simulations," *AIAA journal*, Vol. 41, No. 3, March 2003, pp. 416–424.

[12] Nelson, P. A., Halliwell, N. A., and Doak, P. E., "Fluid Dynamics of a Flow Excited Resonance, Part I: Experiment," *Journal of Sound and Vibration*, Vol. 78, No. 1, 1981, pp. 15–38.

[13] Nelson, P. A., Halliwell, N. A., and Doak, P. E., "Fluid Dynamics of a Flow Excited Resonance, Part II: Flow Acoustic Interaction," *Journal of Sound and Vibration*, Vol. 91, No. 3, 1983, pp. 375–402.

[14] Henderson, B. S., "Category 6 Automobile Noise Involving Feedback - Sound Generated by Low Speed Cavity Tones," NASA Techical Report, 2000, 95-100.

[15] Henderson, B. S., "Category 5: Sound Generation in Viscous Problems, Problem 2: Sound Generation by Flow over a Cavity," NASA Technical Report, 2004, 71-77.

[16] Ma, R., Slaboch, P., and Morris, S., "Fluid mechanics of the flow-excited Helmholtz resonator," *Journal of Fluid Mechanics*, Vol. 623, Jan 2009, pp. 1–26.

[17] Mongeau, L., Bezemek, J. D., and Danforth, R., "Pressure Fluctuations in a Flow-Excited Door Gap Model," *SAE Technical Paper*, 971923, 1997, doi:10.4271/971923.

[18] Lamp, A. and Chokani, N., "Computation of cavity flows with suppression using jet blowing," *Journal of aircraft*, Vol. 34, No. 4, 1997, pp. 545–551.

[19] Fuglsang, D. F. and Cain, A. B., "Evaluation of shear layer cavity resonance mechanisms by numerical simulation," *30th Aerospace Sciences Meeting and Exhibit*, No. AIAA-1992-555, Reno, Nevada, Jun 1992.

[20] Shieh, C. and Morris, P., "Parallel numerical simulation of subsonic cavity noise," *5th AIAA/CEAS Aeroacoustics Conference and Exhibit*, No. AIAA-1999-1891, Bellevue, Washington, May 1999.

[21] Colonius, T., Basu, A., and Rowley, C., "Numerical investigation of the flow past a cavity," *5th AIAA/CEAS Aeroacoustics Conference and Exhibit*, No. AIAA-1999-1912, Bellevue, Washington, May 1999.

[22] Rowley, C., Colonius, T., and Basu, A., "On self-sustained oscillations in two-dimensional compressible flow over rectangular cavities," *Journal of Fluid Mechanics*, Vol. 455, 2002, pp. 315–346.

[23] Brès, G. and Colonius, T., "Three-dimensional instabilities in compressible flow over open cavities," *Journal of Fluid Mechanics*, Vol. 599, 2008, pp. 309–339.

[24] Bertier, N., Courbet, B., Dutoya, D., Vuillot, F., and Sagaut, P., "Large eddy simulation of a subsonic flow over a cavity on general unstructured grids," *42nd AIAA Aerospace Sciences Meeting and Exhibit*, No. AIAA-2004-0679, Reno, Nevada, Jan 2004.

[25] Dubief, Y. and Delcayre, F., "On coherent-vortex identification in turbulence," *Journal of Turbulence*, Dec 2000, pp. 1–23.

[26] Gloerfelt, X. and Bogey, C., "LES of the noise radiated by a flow over a rectangular cavity," *Proceedings of the LES for Acoustics workshop*, Göttingen, Germany.

[27] Larchevêque, L., Sagaut, P., Le, T., and Comte, P., "Large-eddy simulation of a compressible flow in a three-dimensional open cavity at high Reynolds number," *Journal of Fluid Mechanics*, Vol. 516, Jan 2004, pp. 265–301.

[28] Suponitsky, V., Avital, E., and Gaster, M., "On three-dimensionality and control of incompressible cavity flow," *Physics of Fluids*, Vol. 17, No. 10, Jan 2005, pp. 4103–4121.

[29] Larchevêque, L., Sagaut, P., Mary, I., Labbé, O., and Comte, P., "Large-eddy simulation of a compressible flow past a deep cavity," *Physics of Fluids*, Vol. 15, 2003, pp. 193.

[30] Larchevêque, L., Sagaut, P., and Labbe, O., "Large-eddy simulation of a subsonic cavity flow including asymmetric three-dimensional effects," *Journal of Fluid Mechanics*, Vol. 577, Jan 2007, pp. 105–126.

[31] Shieh, C. and Morris, P., "Comparison of two- and three-dimensional turbulent cavity flows," *39th Aerospace Sciences Meeting and Exhibit*, No. AIAA-2001-511, Reno, Nevada, January 2001.

[32] Kurbatskii, K. and Tam, C., "Direct Numerical Simulation of Automobile Cavity Tones," *NASA contractor report*, , No. NASA/CP-2000-209790, 2000, pp. 371–383.

[33] Shieh, C. and Morris, P., "Parallel Numerical Simulation of Automobile Noise Involving Feedback," *NASA contractor report*, , No. NASA/CP-2000-209790, 2000, pp. 363–370.

[34] Ashcroft, G., Takeda, K., and Zhang, X., "A numerical investigation of the noise radiated by a turbulent flow over a cavity," *Journal of Sound and Vibration*, Vol. 265, No. 1, 2003, pp. 43–60.

[35] Marié, S., Ricot, D., and Sagaut, P., "Accuracy of Lattice Boltzmann method for aeroacoustic simulations," *13th AIAA/CEAS Aeroacoustics Conference*, No. AIAA-2007-3515, Rome, Italy, May 2007.

[36] Marié, S., Ricot, D., and Sagaut, P., "Comparison between Lattice Boltzmann method and Navier-Stokes high order schemes for computational aeroacoustics," *Journal of Computational Physics*, Vol. 228, 2009, pp. 1056–1070.

[37] Chen, S. and Doolen, G., "Lattice Boltzmann method for fluid flows," *Annual Review of Fluid Mechanics*, Vol. 30, Jan 1998, pp. 329–364.

[38] Yu, D., Mei, R., Luo, L., and Shyy, W., "Viscous flow computations with the method of lattice Boltzmann equation," *Progress in Aerospace Sciences*, Vol. 39, No. 5, Jan 2003, pp. 329–367.

[39] Tsutahara, M., Kataoka, T., Shikata, K., and Takada, N., "New model and scheme for compressible fluids of the finite difference lattice Boltzmann method and direct simulations of aerodynamic sound," *Computers & Fluids*, Vol. 37, No. 1, Jan 2008, pp. 79–89.

[40] Li, X. M., So, R. M. C., and Leung, R. C., "Propagation Speed, Internal Energy, and Direct Aeroacoustics Simulation Using Lattice Boltzmann Method," *AIAA journal*, Vol. 44, No. 12, Dec 2006, pp. 2896–2903.

[41] Buick, J., Greated, G., and Campbell, D., "Lattice BGK simulation of sound waves," *Europhysics Letters*, Vol. 43, No. 3, Jan 1998, pp. 235–240.

[42] Buick, J., Buckley, C., Greated, C., and Gilbert, J., "Lattice Boltzmann BGK simulation of nonlinear sound waves: The development of a shock front," *Journal of Physics A: Mathematical and General*, Vol. 33, No. 21, Jan 2000, pp. 3917–3928.

[43] Chen, H., "Extended Boltzmann Kinetic Equation for Turbulent Flows," *Science*, Vol. 301, No. 5633, Aug 2003, pp. 633–636.

[44] Mallick, S., Shock, R., and Yakhot, V., "Numerical simulation of the excitation of a Helmholtz resonator by a grazing flow," *Journal of the Acoustical Society of America*, Vol. 114, 2003, pp. 1833–1840.

[45] Wilde, A., "Calculation of sound generation and radiation from instationary flows," *Computers & Fluids*, Vol. 35, No. 8-9, Jan 2006, pp. 986–993.

[46] Premnath, K., Pattison, M., and Banerjee, S., "Large-Eddy Simulation of Self-Sustained Flow Instabilities in Cavities Using the Lattice-Boltzmann Method," *AIAA journal*, Vol. 47, No. 1, 2009, pp. 229–243.

[47] de Jong, A. T. and Bijl, H., "The aero-acoustic resonance behavior of partially covered slender cavities," *Experiments in Fluids*, Vol. 51, No. 5, 2011, pp. 1353–1367.

[48] Succi, S., *The lattice Boltzmann equation for fluid dynamics and beyond*, Oxford University Press, 2001, pp. 11-13.

[49] Bhatnagar, P. L., Gross, E. P., and Krook, M., "A Model for Collision Processes in Gases. I. Small Amplitude Processes in Charged and Neutral One-Component Systems," *Physical Review*, Vol. 94, No. 3, May 1954, pp. 511–525.

[50] Crouse, B., Freed, D. M., Balasubramanian, G., Senthooran, S., Lew, P., and Mongeau, L., "Fundamental Aeroacoustic Capabilities of the Lattice-Boltzmann Method," *12th AIAA/CEAS Aeroacoustics Conference*, No. AIAA-2006-2571, Cambridge, Massachussets, May 2006, pp. 2571–2588.

[51] Brès, G., Pérot, F., and Freed, D. M., *15th AIAA/CEAS Aeroacoustics Conference*, Miami, Florida, May.

[52] da Silva, A. A. and Scavone, G. P., "Lattice Boltzmann simulations of the acoustic radiation from waveguides," *Journal of Physics A*, Vol. 40, 2007, pp. 397–408.

[53] Li, X. M., Leung, R. C., and So, R. M. C., "One-Step Aeroacoustics Simulation Using Lattice Boltzmann Method," *AIAA Journal*, Vol. 44, No. 1, January 2006, pp. 78–89.

[54] Brès, G., Wessels, M., and Noelting, S., "Tandem Cylinder Noise Predictions Using Lattice Boltzmann and Ffowcs Williams-Hawkings Methods," *16th AIAA/CEAS Aeroacoustics Conference*, No. AIAA-2010-3791, Stockholm, Sweden, June 2010.

[55] Noelting, S., Wessels, M., and Freed, D. M., "Prediction of Aeroacoustic Noise from a Simplified Landing Gear Using a Lattice-Boltzmann-Scheme," *46th AIAA Aerospace Sciences Meeting and Exhibit*, No. AIAA-2008-20, Reno, Nevada, January 2008.

[56] Crouse, B., Freed, D. M., Senthooran, S., Ullrich, F., and Fertl, S., "Analysis of Underbody Windnoise Sources on a Production Vehicle using a Lattice Boltzmann Scheme," *SAE Technical Paper*, 2007-01-2400, 2007, doi:10.4271/2007-01-2400.

[57] Pérot, F., Meskine, M., and Vergne, S., "Investigation of the statistical properties of pressure loadings on real automotive side glasses," *15th AIAA/CEAS Aeroacoustics Conference*, No. AIAA-2009-3402, Miami, Florida, May 2009.

[58] Lee, D. K., Pérot, F., and Freed, D. M., "The prediction of the flow induced noise related to automotive HVAC systems," *SAE Technical Paper*, 2011-01-0493, 2011, doi:10.4271/2011-01-0493.

[59] Pérot, F., Kim, D. K., and Lee, D. K., "Direct aeroacoustics prediction of ducts and vents noise," *16th AIAA/CEAS Aeroacoustics Conference*, No. AIAA-2010-3724, Stockholm, Sweden, June 2010.

[60] White, F. M., *Viscous Fluid Flow*, McGraw-Hill, New York, 2nd ed., 1991, pp. 409, 413.

[61] Jeong, J. and Hussian, F., "On the identification of a vortex," *Journal of Fluid Mechanics*, , No. 285, 1995, pp. 69–94.

Chapter 8

Conclusions and Recommendations

The aeroacoustical response of low Mach number flow over slender cavities has been investigated. Intended applications include, but are not limited to, door and trunk lid gaps. In order to be generally applicable for other applications outside automotive, the research has been performed on simplified open and partially covered cavities. The aims of this thesis regarding the investigated geometries were:

- to understand the physics of tonal flow-induced resonance,
- to evaluate techniques to control resonance behavior,
- to investigate if the flow-induced behavior can be predicted using CFD/CAA simulations.

Both wind tunnel experiments and CFD/CAA simulations have been used, next to analytical models of cavity resonance. An experimental and numerical investigation on the physics of slender cavities including seals has been conducted. Resonance modes with spanwise variations have been found and described by a model. The effect of flexible seals on the cavity resonance was minimal. For the control of the flow induced behavior, both passive and active flow control techniques have been investigated experimentally. The aeroacoustical response is sensitive to the design of the resonator opening. Active flow control using plasma actuators can suppress resonance. For simulations, the Lattice Boltzmann Method (LBM) has been used due to its aeroacoustic capabilities. It is shown that LBM can simulate airfoil sharp trailing edge noise and slender cavity flow induced resonance.

Physics of tonal flow-induced resonance

The aeroacoustic response of slender covered cavities has been investigated in order to understand the physics of flow induced resonance. In the investigated geometries several aeroacoustic resonances occur. The base resonance mechanism is of a simple slender Helmholtz type. The higher resonances show spanwise variations that do not correspond to pure simple standing wave modes. All observed resonances are excited by the first stage hydrodynamic mode. The acoustic response (no flow) of the geometry is simulated using a Lattice Boltzmann method. This simulation is validated by comparing it with an experimental acoustic response test. The acoustic simulations revealed the mechanism for the higher resonance modes of the flow experiments by frequency band-filtering the simulation pressure signal in the entire cavity internal volume. The cavity higher modes with spanwise variation can be interpreted as spanwise sections that act as separate Helmholtz resonators interacting with each other. A lumped mass analytical model for the coupled resonator sections has been derived based on the experimental and numerical results that matches the observed mode frequencies well. The observed modes can be described with an increasing number of coupled Helmholtz resonator sections with increasing velocity. The resonance frequency depends on the cavity total spanwise width. In the limit of one resonator, the original slender Helmholtz equation is retrieved.

An additional experimental campaign has been conducted using a slotted cavity with back cabin in a blown splitter plate with various seal designs in between the two volumes. The influence of the investigated flexible seals on the cavity aeroacoustic response amplitude is minimal. The presence of flexible seals slightly lowers the resonance frequency, which can be expected due to the higher cavity compliance. The sound transmission through the seal is masked by the present ambient sound field. For the aluminum block cavity, differences between transmission properties of the seals have been measured. A square seal showed more attenuation than a rounded seal.

Passive and active control of cavity noise

Experimental investigations have been conducted to investigate the potential for passive and active flow control to suppress cavity resonance.

A parametric study on the influence of the cavity opening geometry and boundary layer properties has been conducted. Several configurations showed resonance lock-on, where the acoustic velocity is about one percent of the free stream velocity. Higher modes with spanwise variations are observed, but only for some investigated geometries. The modes can be described by a simple analytical model of coupled Helmholtz resonance with spanwise room modes. The shear layer showed both flapping shear layer and vortex roll-up behavior. The shear layer growth was dominated by interaction with the turbulent boundary layer. Resonance behavior was highly sensitive to the boundary layer thickness. There was a cutoff boundary layer thickness compared to the opening length above which no resonance occured. Only geometries with an upstream cover lip overhang show resonance lock-on behavior. The difference in lock-on behavior between upstream and downstream edge overhangs can be explained by driven cavity internal flow patterns. Rounding of the downstream edge reduces lock-on amplitude due to a reduction of flow entrapment into the cavity, thereby lowering feedback. Rounding of the upstream edge promotes resonance due to the increased mobility and instability of the shear layer, and an increased streamwise length to grow large deflections.

The effect of novel corner-type active-flow-control plasma actuator configurations on the aeroacoustic lock-on behavior of open cavities has been tested. Only upstream mounted actuators were shown to have an effect on the cavity aeroacoustics. In the case of an inwards velocity inducing actuator lock-on was suppressed for all velocities below 12.5 m/s and the outward velocity inducing actuator had an influence on the mode selection at certain flow speeds. The inwards velocity inducing actuator has been investigated experimentally using high speed planar PIV. The cavity induced flow field in the absence of mean flow closely resembles that of planar actuator configurations in literature. During actuation, a secondary circulating flow region is created in the vicinity of the plasma actuator. This modifies the driven flow inside the cavity and the hydrodynamic feedback causing aeroacoustic lock-on.

Simulation capabilities

Three-dimensional aeroacoustic simulations using a Lattice Boltzmann Method have been performed to evaluate the potential of the method to simulate aerodynamics and acoustics in one single simulation. Airfoil sharp trailing edge noise has been chosen as an initial test case because it does not observe feedback or resonance, but does contain boundary layer turbulence. Afterwards partially covered slender cavity flow induced resonance has been simulated.

For the trailing edge noise simulations two airfoil types (NACA 0012, DU 96-180) and two angles of attack (0 and 7 degrees) have been implemented. Two configurations have been used; a clean airfoil configuration and one with a turbulator strip that was forcing boundary layer transition at a fixed location. A final higher resolution simulation has been performed on the NACA 0012, 0 degrees angle of attack, tripped airfoil. Mean fluid dynamic pressure distributions match reference Xfoil results well for all cases. The simulations show direct generation and convection of time resolved turbulent vortices in the airfoil boundary layer. The free transition location is dependent on the angle of attack. Turbulent structures are smaller in the case of tripping using a turbulence strip. The high resolution simulation shows smaller vortices compared to the normal resolution tripped case. Direct measurements of pressure fluctuations in the simulation are compared to those obtained using the Ffowcs-Williams Hawking (FW-H) method and the effect of cyclic boundary conditions on the far-field noise has been investigated in both the time and frequency domain. When compensated for the cyclic spanwise simulation boundaries, the direct and FW-H results match well. The sound field is directed mostly upstream, in agreement with literature. A high resolution simulation sound emission matches well with experiments in literature for amplitude and spectral shape, indicating that the current method can predict both sound production and far field emission in one single simulation. The corresponding normal resolution simulation shows an over-prediction of SPL, but a correct frequency of maximum amplitude and spectral shape.

For cavity resonance, first a flat plate with zigzag type turbulator strip has been simulated to create resolved turbulent boundary layer fluctuations that can be implemented as inlet conditions. The mean, r.m.s. profiles and velocity spectra resemble experimental hotwire and PIV results well. Afterwards cavity geometry with an upstream edge overhang and sharp edges is simulated, where the flat plate boundary layer results are used as inlet conditions. Both reduced and full span setups are simulated. Also simulations including and excluding direct turbulent boundary layer fluctuations are performed to investigate the influence of direct fluctuations on resonance. Simulations with steady inflow conditions show an over-prediction of resonance amplitude. The boundary layer fluctuations are important to obtain the correct resonance response. Simulations with direct turbulent fluctuations introduced at the inlet show resonance amplitudes that match experiment. In case of reduced span simulations, lowering the spanwise width to $W = 4L_o$ increases cavity resonance intermittency in the time domain and broadening of the cavity pressure spectrum. This effect is removed by increasing the spanwise width to $W = 8L_o$. Flow visualizations show a shear layer spanwise coherence which is larger than the boundary layer momentum thickness θ, which confirms the need for a sufficient spanwise simulation width. Full span simulations match the excitation spectrum well for the investigated base mode, first higher mode and a transition mode. The higher mode resonance amplitude is over-predicted, which can be accounted for by the lack of wall compliance of the simulations compared to experiment. The flow simulations indicate that LBM in the current setup is able to simulate door gap cavity resonance behavior. Large spanwise widths and included boundary layer direct turbulent fluctuations are needed to achieve this.

Recommendations

A more applied investigation on a real-world geometries such as existing door and trunk lid gaps on cars is recommended now that more fundamental questions have been addressed and answered.

Physics of tonal flow-induced resonance

Higher modes with spanwise variations have been observed in the investigated cavities. It is recommended to investigate if the observed modes also exist in more complex applied door gap and trunk lid geometries.

For future investigations on the effect of flexible seals, an experimental campaign in an acoustic chamber with a single sided blown flow is recommended. In this way, the acoustic cabin can also be larger and better insulated to prevent sound from other transmission paths than the seal. A finite element analysis of the various seal designs could improve understanding of the differences in attenuation properties. Transmission of sound into the car cabin should be investigated in more detail.

Passive and active control of cavity noise

The effect of the opening geometry has been investigated. This study can be extended to include a large parameter set and more geometry types, like for example two-sided overhangs and step changes in outer plane height. Also the effect of cross-sectional cavity shape on the resonance amplitude can be investigated in more detail.

The current results with dielectric barrier discharge plasma actuators that continuously actuated show the potential for active flow control using feedback and/or periodic actuation to reduce cavity induced noise. Future investigations could cover the effectiveness of these actuator in a feedback or feed forward control loop for more efficient cavity noise control.

Simulation capabilities

Trailing edge noise simulations have shown promising results. It is recommended to investigate if the used LBM setup can be used to investigate and optimize trailing edge noise from for example wind turbines.

It is recommended to implement the found LBM simulation methodologies for simplified cavities on more complex real world gap geometries that are currently used in the automotive and aerospace industries.

Acknowledgements

Over the past years I have been working together with various people from different backgrounds and organizations. Here I would like to take the time to thank each of them.

First of all I would like to thank my promotor, Hester Bijl. She has been a great help and guidance in my promotion. I would like to deeply thank her for her support and enthusiasm. I also would like to give many thanks to Fulvio Scarano for his enjoyable critical discussions and for being so helpful. My thanks to Stefan Bernardy for his help with the final experimental setups. During my time I have had valuable discussions and help from fellow PhD students. Among them I would like to point out my appreciation for the help of Sina Ghaemi, Marios Kotsonis and Valentina Koschatzky.

Even though I have been funded by TUDelft, I have kept on working together with various previous colleagues of Exa Corporation on simulations using the Lattice Boltzmann method in the past years. I would like to thank Dave Freed, Bernd Crouse, Guillaume Brès, Franck Pèrot and Swen Noelting for their cooperation in investigating new applications for the Powerflow simulation software. I would like to thank Stephane Cyr for representing Exa Corp. as part of my committee.

I have also been collaborating with various research groups across the world. I would like to sincerely thank Randolph Leung from Hong Kong Polytechnical University for being a great host during my time in Hong Kong. I would like to give special thanks to Mico Hirschberg from Eindhoven University. He has been very kind in offering much of his time and providing valuable in-depth advice on the topic. I am grateful to Charlie Lew and Alireza Najafi-Yazdi from McGill university for their pleasant collaboration with the FW-H far-field calculations. I would like to sincerely thank Andreas Hazir and Professor Wiedemann from FKFS for their enjoyable cooperation in research.

Finally, last but not least I would like to thank my family: my father, mother and brothers for all their support in the time during my PhD.

Grazie.

Curriculum Vitae Arjen de Jong

Born in Amersfoort, the Netherlands on 29 april 1982.

Education

- **Delft University of Technology**
  MSc and BSc, Faculty of Aerospace Engineering
  (Started 2000, graduated BSc. Cum Laude 2003, MSc Cum Laude: 2008, Honours track)
  Specialized in: Aerodynamics

- **University of Utrecht**
  MSc and BSc, Faculty of Physics and Astronomy
  (Started 2000, graduated BSc. and MSc. With Honors 2006)
  Specialized in: Astrophysics

- **Delft University of Technology**
  PhD, Faculty of Aerospace Engineering
  (2009-2012)

Work experience

- **Ferrari**
  Maranello, Italy, May - October 2004
  Internship at the Gran Turismo department. Development and wind tunnel validation of the computational fluid dynamics (CFD) program for road-going cars, with results used in the design of Maserati and Ferrari cars.

- **The Boston Consulting Group**
  Amsterdam, The Netherlands, April - August 2005
  Internship in strategy consultancy. Visiting associate in a team of 6 people

that worked for the worldwide market expansion strategy of a multinational in the feed industry.

- **NASA Langley Research Center**
  Hampton, Virginia, US, August - December 2005
  Research position. Research in numerical techniques for fluid dynamics, including the complete development of a new grid generation code creating smooth adaptive grids for high order finite difference schemes.

- **Exa Corp.**
  San Francisco, California, US, November 2006 - March 2008
  Exa Corporation is a producer of Fluid dynamics software for the automotive industry. Prediction of aero-acoustic noise from automobile door gaps using experiments and CFD simulations.

- **Porsche AG. / Exa Corp.**
  Weissach, Germany, July 2008 - March 2009
  Fluid Dynamics Consultant onsite at Porsche AG for Exa GmbH. Onsite engineer for Exa applications of both road and race cars.

- **Delft University of Technology**
  Delft, The Netherlands, April 2009 - June 2012
  PhD candidate.

- **Hong Kong Polytechnical University**
  Hong Kong, CN, August 2009 - February 2010
  Visiting researcher at Hong Kong Polytechnical University.

- **TNO**
  Delft, The Netherlands, May 2011 - present
  Freelance consultant contracted through own company: Arjen de Jong Engineering. Fluid dynamics of building wind loading, oil/gas and marine applications, vibration/structural analysis of construction and rail infra.

Additional education

- **University of California Berkeley**
  Berkeley, California, US, Spring 2006
  Spring 2006 semester graduate level student at the University of California, Berkeley. 5 graduate-level courses completed in physics, astronomy and nuclear engineering.

- **Nyenrode Business University**
  Nyenrode, Netherlands, January 2004 - August 2005
  Fundamentals of Business and Economics program, 1-year program including internships. MBA-level courses in business and management for exact

sciences and engineering students, with invited lecturers from different high-ranking enterprises and universities. 2 internships (BCG, EVD) included in the program.

- **Pilot Honors Track program**
  started 2005
  A six-month addition to the normal study program at Delft University of Technology for top ranking students. Focus on competences such as communication skills, philosophy of science and ethics.

Other practical training

- **Jong-Air Holland** *(started 2001)*
  Design and onsite maintenance/inspection of aircraft maintenance equipment, e.g. laminar down-draft spray booths.

- **Economic Information Institute EVD/ Nyenrode Business University** *(February-April 2005)*
  2-month project for the Fundamentals of Business program. Database analysis of the EVD (The institute of the Dutch government for the promotion of export) to investigate export trends of Dutch companies.

Language skills

Dutch, English, German, Italian.

Publications

Patents

- Patent NL 2 004 886, *Luchtverversingssysteem en werkwijze*, June 2010

Journal Publications

- *Investigation of higher spanwise Helmholtz resonance modes in slender covered cavities*
  A.T. de Jong and H. Bijl
  Journal of the Acoustical Society of America, Volume 128, Issue 4, pp. 1668-1678, 2010

- *The aero-acoustic resonance behavior of partially covered slender cavities*
  A.T. de Jong and H. Bijl
  Experiments in Fluids, Volume 51, Issue 5, pp. 1353-1367, 2011

- *Aeroacoustic simulation of slender partially covered cavities using a Lattice Boltzmann method*
  A.T de Jong, H. Bijl, A. Hazir and J. Wiedemann
  Journal of Sound and Vibration, (paper submitted), 2011

- *Edge type plasma actuators for cavity flow induced noise control*
  A.T. de Jong and H. Bijl
  AIAA Journal, (paper submitted), 2012

Conference publications

- *Aircraft design for Mars surface exploration*
  A.T. de Jong, W. Hageraats and R. Raus
  55th ESA International Astronautical Conference (IAC), Fukuoka, Japan, October 16-21, 2005

- *Experimental and numerical investigation of the flow-induced resonance of slender deep cavities that resemble automotive door gaps*
  A.T. de Jong and H. Bijl
  16th AIAA/CEAS Aeroacoustics Conference, Stockholm, Sweden, June 7-9, 2010, AIAA-2010-3863

- *Airfoil trailing edge noise computations using the Lattice Boltzmann Method*
  A.T. de Jong and H. Bijl
  1st AIAA workshop on Benchmark problems for Airframe Noise Computations (BANC-I), Stockholm, Sweden, June 10-11, 2010

Attended conferences and workshops

- Las Vegas, NV, US, NACE congress, (delegate for Birkholz-De Jong Bodywerks LLC), November 2001
- Bremen, Germany, 53rd ESA IAC Conference, September 2003
- Milan, Italy, Fluent Italia Conference, September 2004
- Fukuoka, Japan, 55th ESA International Astronautical Conference, IAC (presenter), October 2005
- Leuven, Belgium, ISAAC20 acoustics workshop, September 2009
- Stockholm, Sweden, 16th AIAA/CEAS Aeroacoustics conference (presenter), June 2010
- Stockholm, Sweden, 1st workshop on Benchmark problems for Airframe Noise Computations (BANC-I) (presenter), June 2010
- Singapore, associate guest lecturer on CFD methods at NTU, November 2010

- Leiden, Netherlands: Lorentzcenter workshop on LBM methods (presenter), February 2011
- Udine, Italy: Workshop Noise Sources in Turbulent Shear Flows, April 2011
- Vaals, Netherlands, Lanxess Global R&D meeting (Arjen de Jong Engineering), presenter: *Trends and developments in automotive engineering, with focus on TRP*, November 2011.
- Delft, Netherlands, AFDAR international workshop on PIV in aeroacoustics, April 2012